Remote Sensing of Inherent Optical Properties: Fundamentals, Tests of Algorithms and Applications

Reports of the
International Ocean-Colour
Coordinating Group

REPORT NUMBER 5

An Affiliated Program of SCOR
An Associate Member of CEOS

Reports of the International
Ocean-Colour Coordinating Group

An Affiliated Program of the Scientific Committee on Oceanic Research (SCOR)
An Associate Member of the Committee on Earth Observation Satellites (CEOS)

IOCCG Report Number 5, 2006

Remote Sensing of Inherent Optical Properties: Fundamentals, Tests of Algorithms, and Applications

Editor:
ZhongPing Lee (Naval Research Laboratory, Stennis Space Center, USA)

Report of an IOCCG working group on ocean-colour algorithms, chaired by ZhongPing Lee and based on contributions from (in alphabetical order):

Robert Arnone, Marcel Babin, Andrew H. Barnard, Emmanuel Boss,
Jennifer P. Cannizzaro, Kendall L. Carder, F. Robert Chen, Emmanuel Devred,
Roland Doerffer, KePing Du, Frank Hoge, Oleg V. Kopelevich,
ZhongPing Lee, Hubert Loisel, Paul E. Lyon, Stéphane Maritorena,
Trevor Platt, Antoine Poteau, Collin Roesler, Shubha Sathyendranath,
Helmut Schiller, Dave Siegel, Akihiko Tanaka, J. Ronald V. Zaneveld

Series Editor: Venetia Stuart

Correct citation for this publication:

IOCCG (2006). Remote Sensing of Inherent Optical Properties: Fundamentals, Tests of Algorithms, and Applications. Lee, Z.-P. (ed.), Reports of the International Ocean-Colour Coordinating Group, No. 5, IOCCG, Dartmouth, Canada.

The International Ocean-Colour Coordinating Group (IOCCG) is an international group of experts in the field of satellite ocean colour, acting as a liaison and communication channel between users, managers and agencies in the ocean-colour arena.

The IOCCG is sponsored by NASA (National Aeronautics and Space Administration), NOAA (National Oceanic and Atmospheric Administration), ESA (European Space Agency), JAXA (Japan Aerospace Exploration Agency), CNES (Centre National d'Etudes Spatiales), CSA (Canadian Space Agency), JRC (Joint Research Centre, EC), GKSS Research Centre (Geesthacht, Germany), BIO (Bedford Institute of Oceanography, Canada) and SCOR (Scientific Committee on Oceanic Research).

http://www.ioccg.org

Published by the International Ocean-Colour Coordinating Group,
P.O. Box 1006, Dartmouth, Nova Scotia, B2Y 4A2, Canada.

ISSN: 1098-6030 ISBN: 978-1-896246-56-7

Printed by GKSS Research Centre, Max-Planck Str., Geesthacht, Germany.

Contents

Preface

Initially, remote sensing of ocean colour focused primarily on the retrieval of the concentration of chlorophyll-a in the global oceans. Subsequent studies, however, have also emphasized the importance of understanding and retrieving, via remote sensing of ocean colour, inherent optical properties (IOPs), namely, the scattering and absorption characteristics of water and its constituents (the dissolved and suspended material). Variations in IOPs are clear indications of changes in water mass or water constituents.

In the past decade, significant progress has been achieved on remote sensing algorithms for IOPs and applications of IOPs in oceanographic studies. This report summarizes the progress to date, thus serving to emphasize the importance of IOPs in ocean optics and in ocean-colour remote sensing. It outlines the fundamental relationships between water-leaving radiance and IOPs (Chapter 1), establishes a data base for algorithm testing and evaluation (Chapter 2), and provides a discussion of sources of uncertainty (Chapter 3).

The bulk of the report (Chapters 4 to 12) reviews the characteristics of a variety of algorithms commonly used in remote sensing practices and assesses their performance when applied to synthetic and *in situ* data sets. Sufficient details are included to allow for easy comparison between the various algorithms and utilisation of the algorithms by interested researchers. Although the ocean-colour community has accomplished a great deal by developing many algorithms for ocean-colour remote sensing, very few broad-range tests, validations, or intercomparisons have been available hitherto. This report provides initial results in this regard, but it should be pointed out that algorithm development is an ongoing process, and we have by no means attempted to include all the algorithms developed, or under development, by the ocean colour community. The report ends with examples of IOP applications in oceanographic studies (Chapter 13) and a summary and conclusions chapter (Chapter 14).

On a more general level, the material discussed in the report illustrates the rich and quantitative information latent in data on visible spectral radiometry (VSR) of the ocean. The information retrieved from ocean-colour remote sensing can contribute to our understanding of the planetary carbon cycle and climate research, as well as other biological and biogeochemical processes in the oceans, and has many other applications including management of marine resources.

This report may not have become a reality without the support of the IOCCG Committee, and the diligent work of the "Algorithm Working Group". In particular, Z.P.L. wishes to extend his appreciation to Dr. Trevor Platt for his guidance throughout the duration of this project, and to the series editor, Dr. Venetia Stuart, for her encouragement and assistance in completing this monograph. The printing of this report was sponsored and carried out by the GKSS Research Centre (Geesthacht, Germany), which is gratefully acknowledged.

Chapter 1

Why are Inherent Optical Properties Needed in Ocean-Colour Remote Sensing?

Ronald Zaneveld, Andrew Barnard and ZhongPing Lee

1.1 Introduction

In this volume we are interested in the determination of useful oceanographic parameters from the radiance measured by a satellite-based sensor. The measured radiance originates from sunlight that passes through the atmosphere, is reflected, absorbed, and scattered by constituents in the ocean, and is transmitted back through the atmosphere to the satellite-based sensor. Solar photons that reach the sea surface are redistributed from those that reached the top of the atmosphere. Absorption of the aerosols and gases changes the intensity of the radiance, while scattering changes the intensity as well as the directionality, resulting in diffuse light that is a function of wavelength. The directional slope spectrum of the waves at the sea surface, together with the radiance distribution, determine the reflected radiance. White caps, bubbles and surface slicks also affect the redistribution of light entering the ocean, in addition to the waves.

The processes of scattering and absorption by dissolved and suspended materials in the ocean affect the spectrum and radiance distribution (light field) of the light emerging from the ocean – the so called water-leaving radiance. The scattering and absorption characteristics of ocean water and its constituents are described by the inherent optical properties (IOPs) (Preisendorfer, 1976). Note that the IOPs do not depend on the radiance distribution. If we can remove the atmosphere and surface effects successfully, the best we can hope for from inversions of the water-leaving radiance are the scattering and absorption characteristics of the dissolved and suspended materials.

While the spectral quality and quantity of the water-leaving radiance is largely determined by the inherent optical properties, conventionally the modification of the radiance has been used to determine oceanic constituents directly. Typically the desired parameter has been the chlorophyll-a concentration, C. Usually algorithm development searches for a combination of radiance signals at several wavelengths to find some ratio, or other combination, that relates empirically to

the desired parameter. The coefficients contained in these algorithms are generally derived by pooling data collected at various spatial and temporal scales. This globally and seasonally inclusive approach, which removes "noise" associated with the data sets, diminishes important spatial and temporal features of the global oceans. This approach assumes that the ocean is a black box, and that little is to be gained by examining how the black box works, presumably because the black box is too difficult to be understood. With such a perception, most algorithm development (even today) uses the black box approach (see Figure 1.1). However, a great deal is known about the inherent optical properties and their influence on the water-leaving radiance, as is detailed below.

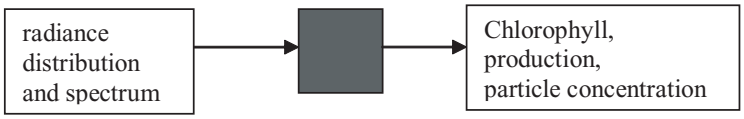

Figure 1.1 Diagram of inverse radiative transfer elements using the "black box" approach.

In the past (CZCS), present (*e.g.*, SeaWiFS, MODIS), and future (VIIRS-NPOESS) missions the emphasis of ocean-colour remote sensing has been on the derivation of the concentration of chlorophyll-a (Hooker *et al.*, 1992; Yoder *et al.*, 2001). This is partly because values of chlorophyll-a play a central role in conventional algorithms for primary production or light attenuation coefficients. Also, it is because in the earlier days of ocean optics studies, chlorophyll-a concentration (as an index to describe a water body) could be routinely measured at sea. Only in the recent decade with the advancement of instrumentation (such as the transmissometer and ac-9), have we been able to look further at the fundamentals and to envisage different inversion schemes. In essence, water colour is determined by inherent optical properties, and chlorophyll is just one of the active components that determine the IOPs. Therefore C can be determined only with a larger uncertainty from ocean-colour remote sensing than the inherent optical properties themselves.

Since no amount of study will modify nature, and the global link between IOPs and C cannot be improved substantially, no real progress has been made in the accuracy of the determination of C from space in the last two decades. On the other hand, it is now assumed, as in VIIRS, that ocean colour can be operational. This should not be interpreted to mean that no further progress can be made in deriving useful information from remotely sensed radiance. By starting at the product end (the need to determine C, production, *etc.*) the real inversion signal, IOP, is ignored. Fundamentally, a better approach would be to ask: "What can water-leaving radiance really give us, and with what accuracy?" Such an approach, based on physics, would examine how water colour is related to the IOPs and then, secondarily, how the IOPs are related to the biogeochemical

parameters of the suspended and dissolved constituents, and finally what these parameters can tell us about processes. Such an approach, as shown below in more detail, would enhance our understanding about the remotely sensed signal, optimize its utilization, and eventually provide improved and reliable products related to the biogeochemistry of the oceans.

1.2 The Forward Problem of Ocean Optics

The process of forward radiative transfer can be summarized by Figure 1.2. In ocean-colour remote sensing, the forward radiative transfer problem is to predict the spectral distribution of water-leaving radiance based on a quantitative description of all the absorption and scattering characteristics of the optical components in the ocean. A recent review of radiative transfer can be found in Zaneveld *et al.* (2005b). The inverse problem is the determination of useful oceanic particulate and dissolved parameters when the spectral characteristics of the water-leaving radiance are known.

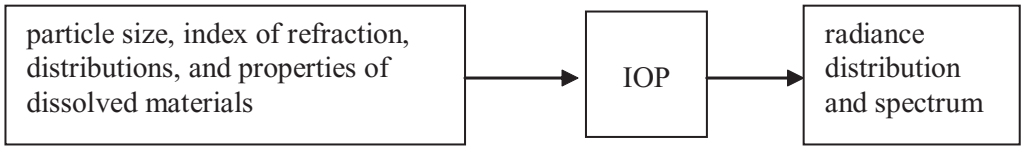

Figure 1.2 Diagram of forward radiative transfer elements.

The forward problem is governed by the Equation of Radiative Transfer (ERT). Without internal sources such as fluorescence or Raman scattering, the ERT is given by:

$$\nabla.L\left(\vec{\mathbf{x}},\lambda,\theta,\phi\right) = -c\left(\vec{\mathbf{x}},\lambda\right)L\left(\vec{\mathbf{x}},\lambda,\theta,\phi\right)+\int_0^{4\pi}\beta\left(\vec{\mathbf{x}},\lambda,\theta,\phi,\theta',\phi'\right)L\left(\vec{\mathbf{x}},\lambda,\theta',\phi'\right)d\omega'. \tag{1.1}$$

The radiance is L, units are W $m^{-2}sr^{-1}$, $\vec{\mathbf{x}}$ is the position vector (x,y,z), θ is the zenith angle, ϕ is the azimuth angle, c is the beam attenuation coefficient (in units of m^{-1}). $\beta(\vec{\mathbf{x}},\theta,\phi,\theta',\phi')$ is the volume scattering function (VSF), with units of $m^{-1}sr^{-1}$. Many books have been written regarding solutions to the ERT (*e.g.*, Chandrasekhar, 1960; Preisendorfer, 1976).

The most common approach in oceanography is to assume that horizontal gradients in radiance and IOPs are much smaller than vertical ones, so that hor-

izontal structure is ignored. This leads to:

$$\cos(\theta)dL(z,\lambda,\theta,\phi)/dz = -c(z)L(z,\lambda,\theta,\phi) + \int_0^{4\pi} \beta(z,\lambda,\theta,\phi,\theta',\phi')L(z,\lambda,\theta',\phi')d\omega'. \quad (1.2)$$

This is the ERT for the so-called plane parallel assumption without internal sources and is widely applied. Numerical solutions to this equation can be found in Mobley (1995) (Hydrolight) and Thomas and Stamnes (1999).

There is a large literature on radiative transfer in the ocean and atmosphere. This body of work is based on deriving radiance distributions when the IOPs are known. Typically, for oceanographic applications, the IOPs used are based on knowledge or speculation of the relationship between particulate and dissolved materials and the IOPs. Again there is a large and developing literature relating particulate properties such as particle concentration, size distributions, index of refraction distributions, and shape to IOP (for a recent review see Twardowski *et al.*, 2005). The forward problem is thus logically broken into two parts: the relationship between biogeochemical parameters and IOPs, and the relationship between the IOPs and the radiance distribution.

1.3 Inherent Optical Properties

Much has been written on inherent optical properties and their wavelength dependencies, examples of which can be found in the books by Shifrin (1988), Kirk (1994), and Mobley (1994). We will briefly summarize here.

The beam attenuation coefficient (c) is a sum of the coefficients of absorption (a) and scattering (b),

$$c = a + b. \quad (1.3)$$

The total scattering coefficient can be divided into forward, b_f, and backward, b_b, components:

$$b = b_b + b_f, \quad (1.4)$$

and

$$b_f = 2\pi \int_0^{\pi/2} \beta(\theta)\sin(\theta)d\theta \text{ and } b_b = 2\pi \int_{\pi/2}^{\pi} \beta(\theta)\sin(\theta)d\theta. \quad (1.5)$$

The theoretical aspects of light scattering are treated extensively in van de Hulst (1981). For the various semi-analytical and analytical remote sensing algorithms, we now have defined the two key IOPs relevant to the remote sensing

reflectance, a and b_b. These IOPs are often separated into operationally defined components such as the dissolved and particulate fractions, and water:

$$a = a_w + a_{ph} + a_d + a_g, \tag{1.6}$$

and

$$b_b = b_{bw} + b_{bp}, \tag{1.7}$$

$$b_f = b_{fw} + b_{fp}, \tag{1.8}$$

which applies to Equation 1.3 as:

$$c = a + b_f + b_b. \tag{1.9}$$

The subscripts "g", "p", and "w" represent dissolved (historically called gelbstoff or gilvin), particulate matter, and water, respectively. Subscripts "ph" and "d" represent the algal and non-algal components of the particles, respectively. Operationally, the dissolved fraction typically comprises all substances that pass through a 0.2 μm filter. The non-algal component is comprised of non-living particulate organic material, living particles such as bacteria, inorganic minerals, and bubbles. The relative contributions of these different particle groups to particulate backscattering are poorly known, but recent progress has been made (Stramski *et al.*, 2001).

Substituting all of the above into the ERT (Equation 1.2) gives:

$$\begin{aligned}\cos(\theta)dL(z,\lambda,\theta,\phi)/dz = &-[a_w + a_g + a_{ph} + a_d + b_w + b_p](z,\lambda)L(z,\lambda,\theta,\phi) \\ &+ \int_0^{4\pi} [\beta_w(z,\lambda,\theta,\phi,\theta',\phi') + \beta_p(z,\lambda,\theta,\phi,\theta',\phi')]L(z,\lambda,\theta',\phi')d\omega'.\end{aligned} \tag{1.10}$$

Of the IOP parameters in the ERT, only a_{ph} relates more or less directly to the concentration of chlorophyll-a, C (depending on the presence of ancillary pigments and their proportionality to chlorophyll-a). The other parameters only relate very indirectly and weakly to C. In so-called Case 1 waters (Morel, 1988), it is assumed that all non-water components vary closely with C. This has been shown to be questionable (Mobley *et al.*, 2004; Lee and Hu, 2006), especially in coastal waters. It is thus clear, that in nature, deriving the radiance based on knowledge of C only, will often lead to incorrect results.

When solving a forward radiative transfer problem, one determines the inherent optical properties in some manner. This can be done by measurement or modelling. Modelling often involves electromagnetic theory, as this allows one

to derive IOPs based on the particle size distribution, index of refraction distribution and shape distribution. Clearly, requiring all of the particulate properties above to be closely related to C, is unreasonable, though in practice has quite frequently been done (*e.g.*, Morel, 1988; Haltrin, 1999). For the purposes of the direct inversion of remote sensing to obtain the concentration of chlorophyll-a, these relations were, of course, a necessity. This encourages inattentive people to believe that all IOPs are in fact a function of chlorophyll only, when this is far from the truth.

1.4 The Inverse Problem of Ocean Optics

The inversion problem is to determine the biogeochemical parameters from the upwelling radiance spectrum, *i.e.* the normalized water-leaving radiance. Zaneveld (1973) has shown that the radiance distribution and its derivative can, in theory, be inverted to obtain the volume scattering function and beam attenuation coefficient, *i.e.* the inherent optical properties. This has not been done in practice. An important point is, however, that the entire radiance distribution and its depth derivative must be known to obtain the IOPs. In remote sensing we only know the radiance at the surface in a few directions. We therefore cannot expect to be able to accurately invert for all of the IOPs. A corollary is that we are unable to invert accurately for the complete suite of biogeochemical parameters which determine the IOPs.

Inversion for either IOPs or biogeochemical parameters is thus inexact and must, perforce, depend on approximations. Based on the discussion above, it is clear that inversion is also a two-step process, explicitly or implicitly: the derivation of IOPs from the radiance, and then biogeochemical parameters from the IOPs. Both of these are inexact procedures, especially for the separation of particulate and dissolved materials. Due to the extremely complex nature of these materials, their full details cannot be expected to be inverted from the IOPs. Nonetheless, one would logically expect inversion of the water leaving radiance spectrum to follow an inverse approach to that of Figure 1.2.

Historically, starting with the CZCS, remote sensing inversions have been focused on the direct derivation of the chlorophyll concentration from water-leaving radiance (*e.g.* Figure 1.1). This was based on the early recognition that chlorophyll-laden waters are “greener” than chlorophyll poor waters. While this was a reasonable starting point, it is also unfortunate in that this is still the oceanographic parameter chosen for performance criteria of future satellite sensors such as NPOESS–VIIRS. This is unfortunate not because chlorophyll is of no interest to scientists and managers, but because chlorophyll is only indirectly, or not at all, related to many of the IOPs that determine radiance, as shown in the IOP section and Figure 1.3. Using chlorophyll as the primary product therefore

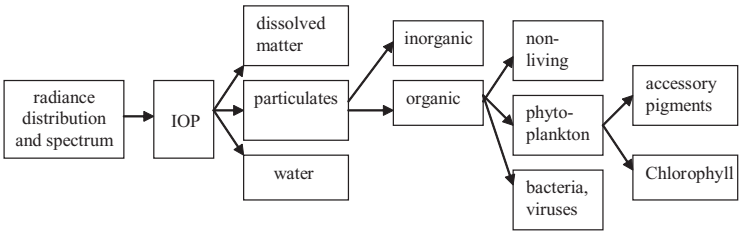

Figure 1.3 Diagram of inverse radiative transfer elements. Many further parameters are derived from these constituents, such as DOC, POC and productivity.

minimizes the information that can be gained from optical remote sensing. Even the chlorophyll concentration itself could be determined with greater accuracy if there was a full understanding of all the optical processes that connect the remotely sensed radiance to the IOPs, and the IOPs to chlorophyll.

It is of course possible to find empirical relationships between radiance ratios and C, for example, but the uncertainties in such relationships cannot be predicted and analyzed. Furthermore such relationships cannot be justified or derived *a priori* using radiative transfer. Because of this, most of the information contained in remotely sensed radiance is ignored or overlooked. This approach thus limits the use and applicability of optical remote sensing.

How can one obtain the maximum information from remote sensing? This requires going back to the approach in Figure 1.3. We must recognize that the radiance spectrum depends physically on the IOPs and solar input. Thus, if we focus on the derivation of the IOPs to the maximum allowed by the geometric restrictions of radiative transfer, we have not diminished the information given to us. Once the IOPs are in hand we can ask the second question: "What particulate and dissolved properties can be derived from the remotely determined IOPs?" Such an IOP-based inversion maximizes the information gained from remote sensing, whereas the black box approach minimizes it. Recently, good progress has been made in the inversion of IOPs from the upwelled radiance spectrum (Roesler and Perry, 1995; Hoge and Lyon, 1996; Lee *et al.,* 1996b; Garver and Siegel, 1997; Carder *et al.,* 1999; Maritorena *et al.*, 2002; Lee *et al.*, 2002; Roesler and Boss 2003).

Semi-analytical approaches to remote sensing inversion (Gordon *et al.*, 1988; Morel, 1988) use an IOP approach in that they use the relationship between the oceanic constituents and the IOPs upon which to base the inversion. Such semi-analytical approaches are based on simple approximations of the remote sensing reflectance such as Equation 1.11. To complete this discussion we present below the fundamental relationship that links remote-sensing reflectance (or water-leaving radiance) and the IOPs.

1.5 The Dependence of the Remote Sensing Reflectance on the IOPs

Most remote sensing inversions are based on this simple relationship:

$$r_{\mathrm{rs}} = L_{\mathrm{u}}(0^-)/E_{\mathrm{d}}(0^-) = g\frac{b_{\mathrm{b}}}{a}, \tag{1.11}$$

where $L_{\mathrm{u}}(0^-)$ and $E_{\mathrm{d}}(0^-)$ are the upwelling radiance and downwelling irradiance just below the sea surface, respectively. A similar relationship developed for subsurface irradiance reflectance was first derived by Gordon *et al.* (1975) and Morel and Prieur (1977) based on modeling the results from radiative transfer calculations. They found that the water reflectance is proportional to the backscattering coefficient and inversely proportional to the absorption coefficient. The proportionality factor g (also called f/Q in the literature, in units of sr^{-1}), which generally varies over the range $0.084 - 0.15\ \mathrm{sr}^{-1}$ for nadir-viewed radiance (Morel and Gentili, 1993; Lee *et al.*, 2004), depends on how the backscattered light relates to the backscattering coefficient, and therefore to the details of the volume scattering function in the backward direction and the radiance distribution. Most of the directional effects of radiative transfer are thus contained in the factor g, and this factor has been studied in detail (for example Gordon *et al.*, 1988; Morel and Gentili, 1993; Lee *et al.*, 2004). Equation 1.11 is the starting point for many inversion algorithms, which remains inaccurate if the dependence of g on the shape of the volume scattering function and the radiance distribution is ignored.

Based on the derivations of Zaneveld (1982; 1995), a theoretical relationship of the dependence of the remote sensing reflectance on the IOPs can be obtained from the ERT (in the form of Equation 1.11) for the nadir radiance, L_{u}, for which $\cos(\theta) = -1$, and for which we can define a vertical attenuation coefficient k_{u}:

$$r_{\mathrm{rs}}(z) = L_{\mathrm{u}}(z)/E_{\mathrm{d}}(z) = \frac{1}{\bar{\mu}_{\mathrm{d}}(z)}\frac{\frac{f_{\mathrm{b}}(z)}{2\pi}b_{\mathrm{b}}(z)}{k_{\mathrm{u}}(z) + c(z) - f_{\mathrm{L}}b_{\mathrm{f}}(z)}, \tag{1.12}$$

where

$$\bar{\mu}_{\mathrm{d}}(z) = \frac{E_{\mathrm{d}}(z)}{E_{\mathrm{od}}(z)}, \tag{1.13}$$

$$f_{\mathrm{b}}(z) = \left(\int_0^{2\pi}\int_0^{\pi/2}\beta(z,\pi,0,\theta',\varphi')L(z,\theta',\varphi')\sin(\theta')d\theta'd\varphi'\right) \Big/ \left(\tfrac{b_{\mathrm{b}}(z)}{2\pi}E_{\mathrm{od}}(z)\right), \tag{1.14a}$$

$$f_{\mathrm{L}}(z) = \left(\int_0^{2\pi}\int_{\pi/2}^{\pi}\beta(z,\pi,0,\theta',\varphi')L(z,\theta',\varphi')\sin(\theta')d\theta'd\varphi'\right) \Big/ \left(b_{\mathrm{f}}(z)L_{\mathrm{u}}(z)\right). \tag{1.14b}$$

Equation 1.12 is an exact expression, as it is only a rewrite of the ERT. All of the details of the radiative transfer process are compressed into the parameters $\bar{\mu}_{\mathrm{d}}(z)$, $f_{\mathrm{b}}(z)$, $f_{\mathrm{L}}(z)$, and $k_{\mathrm{u}}(z)$.

The simple relationship in Equation 1.11 is thus clearly an approximation. Based on Equation 1.12, Zaneveld (1995) has derived the following (also approximate) dependence of g:

$$g \approx \frac{f_{\mathrm{b}}}{2\pi\bar{\mu}_{\mathrm{d}}(0^-)(1+1/\bar{\mu}_{\infty})}, \tag{1.15}$$

where $\bar{\mu}_{\infty}$ is the asymptotic average cosine, which in turn can be described as a function of b/c (Zaneveld, 1989; Berwald *et al.*, 1995).

We thus find that the remote sensing reflectance can be expressed directly in terms of IOPs. This is logical, in that reflectance is a measure of water-leaving radiance, while radiance is determined by the ERT. The difficulty is that all of the directional effects of radiative transfer are involved. The entire shape of the volume scattering function thus matters. Therefore any time we use inversion formulas such as equations 1.11 and 1.15 approximations, uncertainties are introduced.

A further problem in the interpretation of remotely-derived properties is the vertical structure of the IOPs. Recently Zaneveld *et al.* (2005a) derived the dependence of the reflectance at the surface on the vertical structure of optical parameters from first principles. It was shown that the depth dependence is a function of the derivative of the round trip attenuation of the downwelling and backscattered light. With some approximation it can be shown that the backscattering to absorption ratio follows the same vertical integration rule. For backscattering and absorption separately, and for chlorophyll, it can be shown that there is no general formula that allows one to integrate the vertical structure and arrive at the remotely sensed parameter. Only in the special case of "optical homogeneity" where the ratio of the backscattering and absorption coefficients does not vary with depth, can the vertical structure be ignored.

What we learn from the above discussion is that in remote sensing inversion, the directional and vertical details are initially buried in various model parameters. Later, when higher accuracies of inversion are required, this necessitates the reinsertion of information such as the directional effects, as evidenced by Morel and Gentili (1993; 1996) on the bi-directional reflectance. What has not been done, is to start with an expression such as Equation 1.12, which contains the full ERT, and use this as a basis for the derivation of IOPs, and hence particulate and dissolved properties. This is an approach to the question: "What information about the oceanic environment can optical remote sensing provide us?" The multiple connections in Figure 1.3 can then be explored, and such an approach would allow the maximum information content of the remotely-sensed data to be obtained.

Chapter 2

Synthetic and *In Situ* Data Sets for Algorithm Testing

Stephane Maritorena, ZhongPing Lee, KePing Du, Hubert Loisel, Roland Doerffer, Collin Roesler, Paul Lyon, Akihiko Tanaka, Marcel Babin and Oleg V. Kopelevich

---

In algorithm testing and evaluation, we are frequently limited by the availability of adequate data sets. In many studies, individual groups have measured data from limited areas. Those data sets, which are important for the initial development of algorithms, usually lack the dynamic range, and therefore make it difficult to evaluate an algorithm's performance in broader scales. To fill this gap and to have a common ground for algorithm testing, two independent data sets were compiled and adopted by the "Algorithm Working Group". One of the data sets was compiled from global field measurements, where uncertainties among measured properties are common (see Chapter 3). The other data set was simulated using the widely accepted numerical code, Hydrolight (Mobley, 1995), with input IOPs generated based on extensive measurements made in the field. This synthetic data set can perhaps be viewed as results from controlled experiments, where errors from measurement procedures are minimal. This chapter summarizes the characteristics of both the synthetic and *in situ* data sets.

2.1 *In situ* Data Set

The *in situ* data set is an extraction from NASA's SeaWiFS Bio-optical Archive and Storage System (SeaBASS) (Hooker *et al.*, 1994; http://seabass.gsfc.nasa.gov/) and contains chlorophyll-a concentration, above-surface remote sensing reflectance (R_{rs}, which is the ratio of water-leaving radiance, L_w, to downwelling irradiance just above the surface, $E_d(0^+)$) at the first five SeaWiFS bands (412, 443, 490, 510 and 555 nm), along with the detrital (a_d), gelbstoff (a_g), and phytoplankton (a_{ph}) absorption coefficients. Detrital (a_d) and gelbstoff (a_g) absorption coefficients were summed to form a single term (Carder *et al.*, 1991) as a_{dg} (a_{cdm} in Maritorena *et al.*, 2002) and total absorption (a) was calculated by

adding pure water values (a_w) (Pope and Fry, 1997) to a_{ph} and a_{dg} at each wavelength. The chlorophyll-a, remote sensing reflectance, and absorption data were considered a match (*i.e.* coming from a unique station) when all measurements were made within a 12-hour window and within 0.05 degrees in both latitude and longitude. Absorption data come from hyperspectral spectrophotometric measurements but only the SeaWiFS bands were used, for consistency, with the remote sensing reflectance data.

Methods to measure R_{rs}, a_d, a_g and a_{ph} are summarized in NASA's technical memorandum (Mueller and Austin, 1992). Generally, phytoplankton absorption coefficients were obtained by spectrophotometric measurements after filtration of a water sample through a GF/F filter. Detrital absorption coefficients were obtained after a methanol extraction of the pigments on the GF/F filter. For all measurements related to filter pad, there is a need to correct for pathlength amplification ("beta-factor" correction) (Mitchell and Kiefer, 1988; Bricaud and Stramski, 1990). Errors will be introduced when an incorrect "beta-factor" is used (Cleveland and Weidemann, 1993; Allali *et al.*, 1995).

Gelbstoff absorption coefficients were obtained by measuring the absorbance of the filtrate with a spectrophotometric cell (usually $\sim$ 10 cm in length). Remote sensing reflectance data were obtained by either in-water or above-surface radiometric measurements (Mueller *et al.*, 2002). Backscattering measurements were too rare to be included here. As always, errors (sometimes quite large) are associated with each of the measured components.

Data were filtered by applying quality control procedures to the remote-sensing reflectance and absorption data. For R_{rs}, these procedures consisted of comparisons with the SeaBAM data set (O'Reilly *et al.*, 1998) and the synthetic data set described in Section 2.2. For a given chlorophyll range, data with $R_{rs}(\lambda)$ values either 10% higher than the maximum or 10% lower than the minimum value found in the SeaBAM or synthetic data sets were eliminated. While this procedure removed extra noise in the data set, it may have also removed some extreme cases such as CDOM or sediment dominated waters. Of the 1,235 original data points, 177 points were eliminated during this step.

For the absorption components, the following controlling factors were applied:

$$
\begin{aligned}
1.0 &< a_{dg}(412)/a_{dg}(443) < 2.0, \\
1.0 &< a_{dg}(443)/a_{dg}(490) < 3.0, \\
0.5 &< a_{ph}(412)/a_{ph}(443) < 1.1, \\
0.1 &< a_{ph}(490)/a_{ph}(443) < 1.0,
\end{aligned}
$$

and another 402 points were removed during this step. The final *in situ* data set contains only 656 stations with a complete set of chlorophyll concentration, R_{rs}, and component absorption data. Most of the data come from locations that

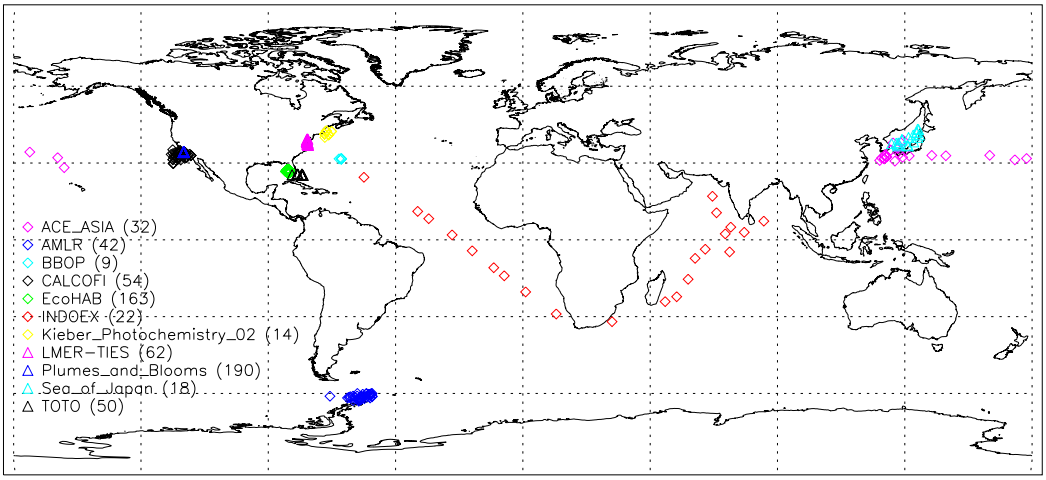

Figure 2.1 Data location of the *in situ* data set. The origin of the data and the number of stations (in parentheses) by experiment are also indicated.

are relatively close to the coast and some of the data are from high latitudes. Figure 2.1 presents a summary of the origin and location of the *in situ* data set.

2.2 Synthetic Data Set

This data set (a total of 500 points) contains both inherent (IOP) and apparent (AOP) optical properties. IOPs, required as inputs for Hydrolight (Mobley, 1995), are simulated with optical and bio-optical parameters and models. Detailed descriptions regarding the simulation of IOPs and AOPs can be found at:
http://www.ioccg.org/groups/OCAG_data.html.

The absorption coefficient of the bulk water was simulated using a four-term model (Prieur and Sathyendranath, 1981; Roesler *et al.*, 1989; Carder *et al.*, 1991; Bukata *et al.*, 1995; Fischer and Fell, 1999; Doerffer *et al.*, 2002), with contributions from water molecules, phytoplankton, detritus, and gelbstoff. Values of $a_w(\lambda)$ were taken from Pope and Fry (1997). Values of $a_{ph}(\lambda)$ were modelled as $a_{ph}(440)$ multiplying the spectral shape of phytoplankton absorption coefficient ($a^+_{ph}(\lambda) \equiv a_{ph}(\lambda)/a_{ph}(440)$), with $a_{ph}(440)$ expressed as a function of the chlorophyll concentration (the specific absorption coefficients at 440 nm were taken from Bricaud *et al.*, 1995; 1998). Oligotrophic and eutrophic waters exhibit different spectral shapes of phytoplankton absorption spectra (Hoepffner and Sathyendranath, 1992; Stuart *et al.*, 1998). To represent this natural variation, at least to the first order, an $a^+_{ph}(\lambda)$ data bank (600 spectra) was composed from the extensive measurements of Bricaud *et al.* (1995; 1998) and Carder *et al.* (1999). This $a^+_{ph}(\lambda)$ data bank is divided into nine groups separated by the measured $a_{ph}(440)$ values. Figure 2.2 presents examples of $a^+_{ph}(\lambda)$ from the nine

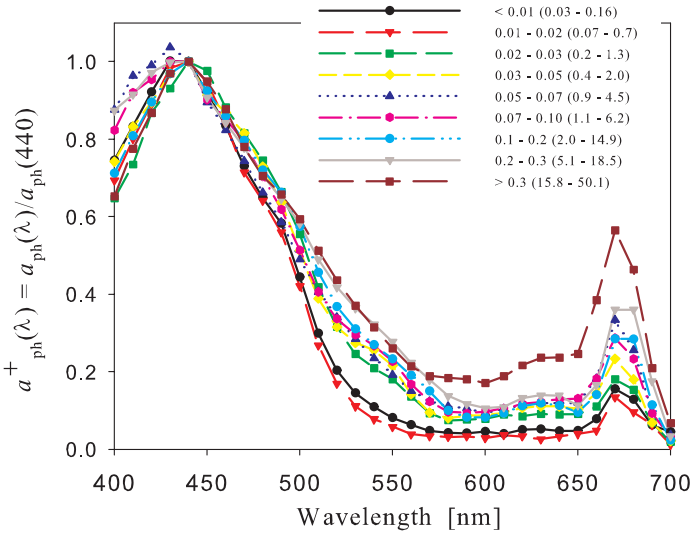

Figure 2.2 Examples of a_{ph} spectral shape for the nine a_{ph} groups (separated by values of $a_{\mathrm{ph}}(440)$ [m^{-1}]). Numbers in parenthesis are the range of C [mg m^{-3}] for those groups.

groups. In the simulation of $a_{\mathrm{ph}}(\lambda)$ spectra, $a^+_{\mathrm{ph}}(\lambda)$ is selected randomly within the group in which the $a_{\mathrm{ph}}(440)$ value falls. Using this process, the variability of a_{ph} spectral shapes is retained in the modelled $a_{\mathrm{ph}}(\lambda)$ spectra, and at the same time the $a^+_{\mathrm{ph}}(\lambda)$ of eutrophic waters will not be used to generate $a_{\mathrm{ph}}(\lambda)$ of blue oceanic waters, or vice versa.

Absorption spectra of both detritus and gelbstoff were described as exponentially decreasing functions with wavelength (Bricaud *et al.*, 1981; Roesler *et al.*, 1989). The spectral slopes were treated as random variables but constrained by ranges commonly observed in the field. The absorption coefficients at 440 nm also varied randomly, but this randomness was constrained such that the ranges were wider for higher C values and narrower for lower C values.

The total scattering coefficient was simulated by a three-term model (Bukata *et al.*, 1995), with contributions from water molecules, phytoplankton, and inorganic particles. Two different particle phase functions were used to represent the scattering distribution of phytoplankton and inorganic particles. For both particulates, the scattering coefficients at 550 nm and the spectral exponents were varied randomly (but within commonly observed ranges).

With the above modelled absorption and scattering (backscattering) coefficients, Hydrolight was used for the calculation of radiance distribution and then the AOPs, which include the nadir-viewed above-surface remote-sensing reflectance (R_{rs}), nadir-viewed subsurface remote-sensing reflectance (r_{rs}), and

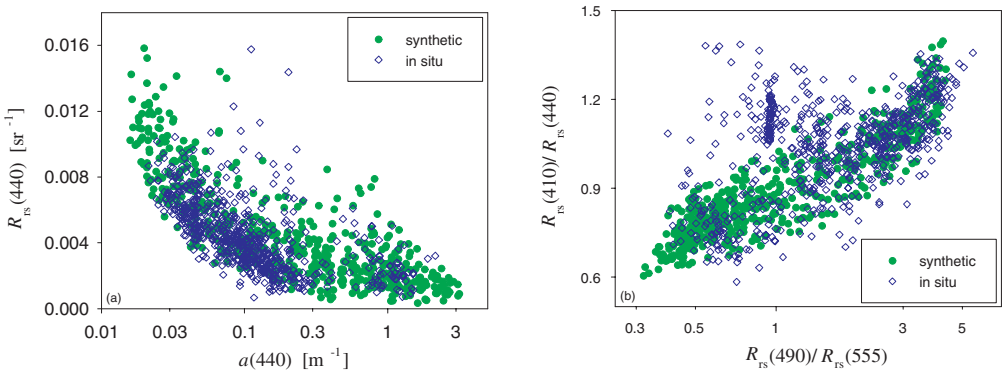

Figure 2.3 Comparison between *in situ* and synthetic data sets. (a) Ranges and variations of $R_{rs}(440)$ and $a(440)$. (b) Ranges and variations of $R_{rs}(410)/R_{rs}(440)$ and $R_{rs}(490)/R_{rs}(555)$.

subsurface irradiance reflectance (R). In the Hydrolight runs, solar input was simulated with the Gregg and Carder (1990) model with marine aerosols, and the sky was assumed to be cloud free. A wind speed of 5 m s^{-1} was applied, and the water body was assumed to be homogeneous. Spectral bands were set from 400 to 800 nm, with a spacing of 10 nm. Inelastic scattering (*i.e.* Raman scattering, chlorophyll-a fluorescence) was excluded.

For consistency, the synthetic data set was compared with the *in situ* data set. For the two data sets Figure 2.3a shows the range and variation of $R_{rs}(440)$ versus $a(440)$, and Figure 2.3b shows the range and variation of $R_{rs}(410)/R_{rs}(440)$ versus $R_{rs}(490)/R_{rs}(555)$. We used $R_{rs}(412)/R_{rs}(443)$ instead of $R_{rs}(410)/R_{rs}(440)$ for the *in situ* data set, although the effects of these small wavelength differences are considered negligible. For both data sets, $a(440)$ is in the range of $\sim 0.02 - 3.1$ m^{-1}, while $R_{rs}(490)/R_{rs}(555)$ is in the range of $\sim 0.3 - 5.2$ m^{-1}. Clearly, the two data sets agree with one another in variation and coverage, although for $R_{rs}(490)/R_{rs}(555)$ ratios around ~ 1.0, some *in situ* data points have higher $R_{rs}(410)/R_{rs}(440)$ ratios.

Although this synthetic IOP-AOP data set may not cover all possible variations that occur in natural waters, it nevertheless covers a wide range of variations encountered in the field, since the models and parameters used in the simulation process are based on extensive field measurements. In the following chapters (Chapter 4 – Chapter 12), a series of algorithms currently used for the retrieval of IOPs from $R_{rs}(\lambda)$ are applied to both the synthetic and the *in situ* data sets, and the retrieved absorption and/or backscattering coefficients are compared with known (synthetic) or measured (*in situ*) values, respectively. To evaluate the performance of each algorithm, regression results (Type II, Laws, 1997) and Root-Mean-Square-Error (RMSE) are calculated and tabulated for each property, in log space. RMSE is defined as:

$$\mathrm{RMSE} = \left(\frac{\sum_{i=1}^{N} \left[\log\left(IOP_i^{\mathrm{model}}\right) - \log\left(IOP_i^{\mathrm{true}}\right) \right]^2}{N-2} \right)^{1/2}, \tag{2.1}$$

where $\mathrm{IOP}_i^{\mathrm{model}}$ stands for the i$^{\mathrm{th}}$ property derived from $R_{\mathrm{rs}}(\lambda)$, $\mathrm{IOP}_i^{\mathrm{true}}$ for the i$^{\mathrm{th}}$ property known either from simulation or from *in situ* measurements, and N is the number of valid retrievals. It is necessary to point out that a slightly different set of IOPs may be derived from the same $R_{\mathrm{rs}}(\lambda)$ due to architecture differences. Also, for the same IOP product, not all algorithms may derive valid retrievals for a given $R_{\mathrm{rs}}(\lambda)$ spectrum, due to the different settings of the algorithms. Such non-valid retrievals are then excluded in the performance analysis, and result in a smaller data set, and likely better statistical results.

Chapter 3

Uncertainties in the Products of Ocean-Colour Remote Sensing

Emmanuel Boss and Stephane Maritorena

Data products retrieved from the inversion of *in situ* or remotely sensed ocean-colour data are generally distributed or reported without estimates of their uncertainties. The accuracy of inversion products such as chlorophyll-a or IOPs is frequently evaluated by comparison with *in situ* measurements, but these analyses are not always sufficient to determine the level of uncertainty of an ocean-colour product. This is particularly true for remote sensing data where match-up analyses (McClain *et al.*, 2000; http://seabass.gsfc.nasa.gov/matchup_results.html) can only be performed for an infinitesimal fraction of a sensor's records. Although very useful, these analyses cannot provide reliable estimates of how ocean-colour uncertainties vary with time and/or space. Moreover, because the uncertainties of the input data (for example the normalized water-leaving radiance, L_{wN}) vary in space and time, the uncertainties of the output products cannot be reported simply as a single global value unless it is intended to provide general bounds. Some ocean-colour products are also used as input to other models (for example, to calculate primary production or to assimilate phytoplankton carbon into ecosystem models) for which uncertainty budgets cannot be properly established without knowledge of the uncertainties associated with the input data. It is thus important that the variations of the uncertainty in L_{wN} and in the products derived from them are documented in time and space. This section discusses the various types of uncertainties present in ocean-colour data or products and emphasizes recent approaches that allow uncertainties of satellite ocean-colour products to be estimated on a pixel-by-pixel basis.

3.1 Sources of Uncertainty

3.1.1 Uncertainties in *in situ* measurements (L_{wN}, R_{rs}, C, IOP)

In situ data are used for algorithm development and for validation of algorithms and data products. While *in situ* measurements are frequently considered as "the reference" to which other data (*e.g.* satellite data) are compared, they contain significant levels of uncertainties caused by various experimental and environmental factors. Calibration, dark signal, data processing, deployment strategy, sea and sky states all introduce uncertainties in the radiometric measurements (Siegel *et al.*, 1995; Hooker and Maritorena, 2000; Hooker *et al.*, 2001). Close compliancy to establish measurement protocols (*e.g.* Mueller and Austin, 1995 and follow up) along with regular and rigorous calibrations and good characterization of instruments are key to the minimization of uncertainties in the *in situ* measurements. Measurements of biogeochemical variables have their own set of difficulties and resulting uncertainties (Mitchell *et al.*, 2000; Van Heukelem *et al.*, 2002; Claustre *et al.*, 2004). Most of the data sets that are publicly available (*e.g.*, SeaBASS) do not contain information regarding the estimated uncertainties of the various variables they contain (*e.g.*, the differences between the triplicate chlorophyll measurements and the uncertainties in the radiometer reading, based on its variability through the sampling period and its calibration history). It is frequently assumed that the uncertainties of *in situ* data are small and in any case much smaller than the uncertainties arising from the natural spatial/temporal variability of a given variable.

Another uncertainty arises from the fact that the match-up field data usually characterize an area of around 1–10 m while the satellite spatial scale is often 100–1,000 m. This environmental mismatch in scales introduces an uncertainty that is often hard to quantify. Also, satellite measurements represent a water-column weighted average (Gordon and Clark, 1980; Sathyendranath and Platt, 1989; Zaneveld *et al.*, 2005a), while *in situ* measurements usually come from discrete depths. Therefore, for vertically inhomogeneous waters, uncertainties arise when the two are compared with each other. Some sampling platforms such as on-line sampling from steaming vessels, undulating vehicles, gliders, and autonomous underwater vehicles (AUVs) are likely to be fruitful approaches in quantifying these uncertainties.

3.1.2 Uncertainties in satellite measurements (L_{wN})

Various sources of random and systematic error contribute to disagreements between measured normalized water-leaving radiances and their actual values. Uncertainties in L_{wN} are introduced through a variety of factors such as pre-launch characterization of the sensor, atmospheric and bi-directional corrections, and

uncertainties in the monitoring of the changes in the sensor's performance. Errors in geo-location, contamination with light emanating from adjacent pixels or other factors like white caps can also add to this uncertainty. The calibration/validation activities of each ocean-colour mission are designed to assess and minimize the magnitude of this uncertainty (and remove any bias). Prelaunch and on-orbit characterization of the sensors (*e.g.*, measurements of reflected Sun and/or Moon light) along with vicarious calibrations (*e.g.*, the MOBY buoy) and match-up analyses are the major procedures used to quantify uncertainties of normalized water-leaving radiances.

The calibration/validation activities and the reduction of the uncertainties in the derived L_{wN} should be one of the primary tasks of space agencies providing the ocean-colour data and much effort must be invested in minimizing it for various missions. In the remainder of this chapter we will therefore assume the uncertainty in the L_{wN} is known and documented, although at present uncertainties in atmosphere correction still dominates errors in L_{wN} of coastal waters.

3.1.3 Uncertainties and assumptions in the functional relationship that links L_{wN} and IOP and in the inversion procedure used to derive the products

Uncertainties in the products derived from the inversion of L_{wN}, however, do not benefit from the same level of effort. In what follows we will address these uncertainties with reference to the type of algorithm designed to produce them, distinguishing between empirical and semi-analytical inversion algorithms. The approaches used in some recent works to provide ocean-colour product uncertainties are also described.

3.1.3.1 Obtaining uncertainties in products based on empirical algorithms

Empirical algorithms are developed from data sets where *in situ* radiometry and a to-be-derived product (*e.g.*, chlorophyll-a, POC) have been collected at the same spot of the ocean and within a narrow period of time. A regression is most often performed to obtain the 'best-fit' function between the two variables and to define the formulation that relates the two quantities. The type of regression used to relate two variables is relevant to the uncertainty discussion because regression methods work under different assumptions about uncertainties in the data involved. Type-I regressions (Laws, 1997) are the most frequently used and are based on the assumption that only the dependent variable (*i.e.* y, the product) has an uncertainty, while the independent variable (*i.e.* x, the input data) is error free. In Type-I regressions, the individual uncertainties in the input data are not taken into account and it is generally assumed that the relative error

in the variable is constant. Conversely, Type-II regressions (Press *et al.*, 1992; Laws, 1997) assume that both variables have uncertainties and are thus better adapted for ocean colour where substantial uncertainties frequently exist in the variables involved (*e.g.*, reflectance ratio, chlorophyll).

An empirical algorithm is as good as the data it is based on, and on how representative the data are of the environment or bio-optical provinces where the algorithm is to be applied. *In situ* data sets are often geographically and seasonally biased due to constraints in the timing and location of oceanic cruises (Claustre and Maritorena, 2003).

In general, it is crucial that data sets used in the development (or validation) of an ocean-colour algorithm have complete information about the location and time at which the data were collected and about their quality (*i.e.* associated uncertainties). The geographical and temporal extent of a data set determines the water types where the algorithm can be applied, whereas uncertainties in products require information on uncertainties in the input data.

For empirical algorithms, the dispersion of the y-axis data (*i.e.* the product) around the "mean" relationship of the resulting algorithm provides, to some degree, information about the uncertainties that can be expected at any given x-axis value (*i.e.* the input data). However, this only represents the uncertainties associated with the data set used in the regression and cannot be generalized unless the data set fully encompasses all the natural variability that exists for the water types included. Ideally, to evaluate the uncertainties of an empirical algorithm one needs a different data set than that with which the algorithm was developed; the statistics of the differences between the inverted products and the measured products in this independent data set can then be used to evaluate the uncertainties in the product. Additionally, an uncertainty propagation analysis to evaluate the effect of the uncertainties in the L_{wN} on the output has to be carried out to establish whether or not this uncertainty is a significant source for uncertainty in the product (*e.g.*, to what extent a 5% relative uncertainty in L_{wN} at 440 and 555 nm affects the IOPs retrieved).

In the case of neural network (NN) based algorithms, uncertainties should be determined from a rigorous statistical approach. Aires *et al.* (2004) provided an example of such an approach to products derived from remote sensing (other than ocean colour). They use a Bayesian technique to evaluate the uncertainties in the NN parameters which are then used to compute the uncertainties in the outputs.

Another way to determine whether the measured reflectance spectrum is within the domain of the bio-optical models used to simulate reflectance spectra, which in turn were used to train a neural network, has been developed for the Medium Resolution Imaging Spectrometer (MERIS) (Doerffer and Schiller, 2000; Krasnopolsky and Schiller, 2003). For this purpose one network is trained to determine concentrations from the eight MERIS bands together with the solar and

viewing zenith angles and the azimuth difference between viewing and sun direction (see Chapter 6). A second, forward, network is trained with the same data set, which takes the derived concentrations as input and produces reflectances. The deviation, calculated as the Chi^2 (Sokal and Rohlf, 1981), over all eight bands between the measured and the computed spectrum, is then used as an indicator to see if the measured spectrum is within the training range, and thus within the scope of the algorithm. In the case of the MERIS ground segment, a flag is raised whenever the Chi^2 deviation exceeds a certain threshold. However, the Chi^2 value can also be used as an uncertainty measure. Furthermore, a technique has been developed (Schiller and Doerffer, 2005), which combines the neural networks with an optimization procedure, to estimate the uncertainty of a product on a pixel-by-pixel basis.

3.1.3.2 Obtaining uncertainties in products based on semi-analytical models

Semi-analytical models or algorithms are based on the premise of a known relationship (derived from the radiative-transfer theory) between L_{wN} (or a function of it) and IOPs (generally the absorption, a, and the backscattering, b_b, coefficients). These models contain some level of empiricism in the way IOPs are parameterized (*i.e.* how their variations and spectral shapes are formulated) and they also use simplified assumptions for some of their components (see Chapter 1). The inversion of semi-analytical models generally allows the simultaneous retrieval of several variables contained in the IOP terms. Like empirical algorithms, semi-analytical models are affected by uncertainties in L_{wN} but they are also influenced by uncertainties associated with the chosen relationship between L_{wN} and IOPs, and uncertainties resulting from the assumptions used in their formulation.

Sensitivity analyses are frequently used to assess how assumptions used to describe the component terms of a model affect retrievals (Roesler and Perry, 1995; Hoge and Lyon, 1996; Garver and Siegel, 1997). Although very useful, this approach does not allow the determination of a product's uncertainty on a case-by-case (or pixel-by-pixel) basis, but rather provides a general uncertainty estimate. To our knowledge, only two methods have recently been used with ocean-colour data that can estimate the uncertainties of products retrieved by the inversion of a semi-analytical model on a case-by-case basis. The first one (Maritorena and Siegel, 2005) is a non-linear adaptation of the calculation of confidence intervals in linear regressions. Essentially, this method is based on the projection of the residuals between the observed and reconstructed (from the inverted variables) L_{wN} in the solution (*i.e.* retrieved variables) (Bates and Watts, 1988).

A recent study (Wang *et al.*, 2005) suggests another approach to compute uncertainties of the retrieved variables. In this approach, each of the variables

to be retrieved has a predefined set of spectral shapes and the model is inverted for each of the possible combinations of these spectral shapes resulting in an extensive set of possible solutions. These results are then filtered to keep only the "realistic" (e.g., positive) solutions that can closely reproduce the input L_{wN} spectrum (within a pre-described difference from the L_{wN} based on the uncertainties in L_{wN} and the uncertainties in the theoretical relationship between L_{wN} and IOP). The final value for each inversion product and its associated uncertainty is then obtained from the statistics (median and percentiles) on the acceptable solution subset. The key steps in this approach are the choice of the acceptance criteria for the solutions (*e.g.*, what is the acceptable difference between observed L_{wN} and that reconstructed from retrieved IOP) and the choice of range in possible shapes for the spectrum of each individual IOP. The two methods described above do not produce the same kind of uncertainties, and thus they are not directly comparable. Both approaches have benefits and limitations. For example, the Maritorena and Siegel (2005) approach always returns a value for the confidence interval of the retrieved product because the calculations do not depend on spectral criteria but on the sum of the residuals (weighted by the spectral uncertainties of the input data, if they are known). On the other end, this approach does not take into account the uncertainties caused by the model assumptions. In the Wang *et al.* (2005) approach, uncertainties in the model and data are included in the spectral agreement criteria but the inversion may fail to find any solution that satisfies this criteria. Although it uses an efficient linear matrix inversion technique (Hoge and Lyon, 1996), the Wang *et al.* (2005) method is also more computationally demanding (computational demands increase with numbers of possible combinations of different shapes of IOPs).

3.2 Summary

While some preliminary uncertainty estimates for ocean-colour products are available through match-up analyses, uncertainties are generally not provided on a per data point basis. This has caused many users to use ocean-colour products as a qualitative descriptor of patterns rather than a quantitative variable. Others use these products in biogeochemical models (*e.g.*, computing primary productivity) without being able to propagate uncertainties.

For some ocean-colour missions, such as for MERIS, a sophisticated flagging system has been developed. It computes, on a pixel-by-pixel basis, indicators for the reliability of a product by regarding different possible error sources including sun glint, failure in the atmospheric correction, high turbidity in the water, *etc.* A flag for each possible problem is raised if the uncertainty value exceeds a certain threshold. By this method, the user gets a warning and has to decide if he can accept this pixel for further computations.

We have reviewed briefly some of the uncertainties present in ocean-colour data, and have presented different approaches to establish uncertainties in products of ocean-colour remote sensing for either empirical or semi-analytical algorithms. The procedures described above are not complicated and their full application benefits from the knowledge of uncertainties in the input data. Use of such approaches will help the ocean-colour community establish quantitative confidence in the remote-sensing products.

Chapter 4

Simple Algorithms for Absorption Coefficients

ZhongPing Lee, Stephane Maritorena, Andrew Barnard

4.1 One-Step Spectral Ratio Algorithm

4.1.1 General description

In a similar fashion to the empirical approach of deriving chlorophyll-a concentration from ocean-colour data, the simplest way to derive absorption coefficients from $R_{rs}(\lambda)$ is by empirical relationships. This kind of approach does not require knowledge of the fundamental relationships between R_{rs} and IOPs, but requires an adequate data set to develop the empirical coefficients. For the derivation of the total absorption coefficient at 440 nm, based on limited measurements (63 data points), Lee *et al.* (1998b) developed an empirical spectral-ratio algorithm from the spectral ratios of $R_{rs}(\lambda)$. To obtain a better fit between measured and algorithm-derived values, the algorithm uses quadratic polynomials with two spectral ratios:

$$\log\left(a(440)\right) = A_0 + A_1\rho_{25} + A_2\rho_{25}^2 + B_1\rho_{35} + B_2\rho_{35}^2, \tag{4.1}$$

where ρ_{25} and ρ_{35} are

$$\rho_{25} = \log\left(\frac{R_{rs}(440)}{R_{rs}(555)}\right), \rho_{35} = \log\left(\frac{R_{rs}(490)}{R_{rs}(555)}\right). \tag{4.2}$$

Values of $A_{0,1,2}$ and $B_{1,2}$ in Equation 4.1, derived by least-square fitting, are -0.674, -0.531, -0.745, -1.469, and 2.375, respectively (Lee *et al.*, 1998b).

4.1.2 Results and discussion when applied to the IOCCG data sets

With R_{rs} values at 440, 490 and 555 nm (or nearby wavelengths) as inputs, values of $a(440)$ were calculated from Equations 4.1 and 4.2. Figure 4.1 compares the derived and known $a(440)$ values for the synthetic and the *in situ* data sets, respectively. For the synthetic data set, this empirical algorithm systematically overestimated $a(440)$ for most of the data, though good correlation of determination ($R^2 = 0.976$) was achieved between the algorithm derived, and known

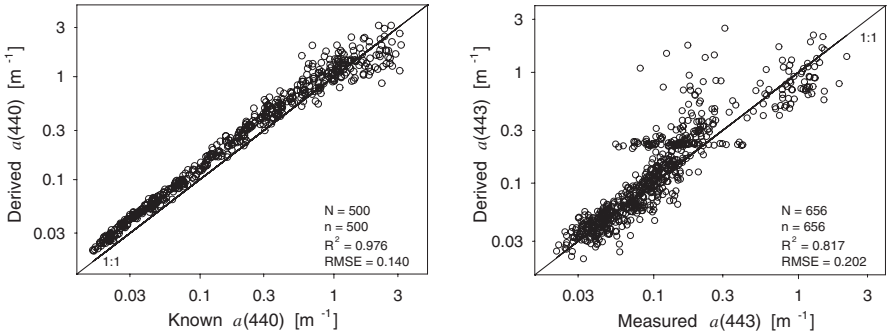

Figure 4.1 Comparison between algorithm-derived and known IOP, using algorithm results from the empirical approach of Lee *et al.* (1998b). Results of $a(440)$ from the synthetic data set (left) and $a(443)$ from the *in situ* data set (right).

$a(440)$ values (see Table 4.1). These results suggest that the empirical coefficients, derived by forcing Equation 4.1 derived $a(440)$ to match a limited number of $a(440)$ from field measurements, were biased by data from those measurements. It is likely that when more high-quality data are available, the coefficients in Equation 4.1 could be fine tuned and the estimation of $a(440)$ from $R_{rs}(\lambda)$ by simple ratios could be improved.

Table 4.1 RMSE and regression (Type II) results for the synthetic data set ($\theta_0 = 30°$). N is the number of data tested, while n is the number of valid retrievals by the relevant algorithm.

	N	n	intercept	slope	R^2	RMSE	bias
$a(440)$, L98[a]	500	500	0.050	0.939	0.976	0.140	0.091
$a(440)$, B99[b]	500	500	-0.466	0.538	0.932	0.356	-0.151
$a(490)$, B99	500	500	-0.488	0.574	0.948	0.281	-0.119
$a(410)$, MM01[c]	500	500	-0.368	0.747	0.976	0.295	-0.221
$a(440)$, MM01	500	500	-0.299	0.792	0.976	0.224	-0.156
$a(490)$, MM01	500	500	-0.256	0.815	0.965	0.169	-0.096

[a]Lee *et al.* (1998b) [b]Barnard *et al.* (1999) [c]Morel and Maritorena (2001)

For the *in situ* data set, the R^2 value is 0.817 and the RMSE is 0.202 (see Table 4.2), indicating that algorithm-derived $a(443)$ are quite consistent with $a(443)$ values from water samples. The larger differences are likely due to uncertainties associated with both $R_{rs}(\lambda)$ and $a(443)$ in the *in situ* measurements (see also Chapter 3 for discussions regarding uncertainties).

Table 4.2 RMSE and regression (Type II) results for the *in situ* data set. N is the number of data tested, while n is the number of valid retrievals by the relevant algorithm.

	N	n	intercept	slope	R^2	RMSE	bias
a(443), L98	656	656	0.140	1.081	0.817	0.202	0.061
a(443), B99	656	642	0.085	1.039	0.643	0.272	0.047
a(490), B99	656	642	0.152	1.080	0.626	0.255	0.062
a(412), MM01	656	656	-0.228	0.911	0.817	0.237	-0.147
a(443), MM01	656	656	-0.158	0.954	0.821	0.210	-0.113
a(490), MM01	656	656	-0.117	0.949	0.808	0.171	-0.059

4.2 Spectral Curvature Algorithm

4.2.1 General description

A simplistic 3-wavelength ratio method to test *in situ* measurements of remote sensing reflectance and the absorption coefficient for closure was developed by Barnard *et al.* (1999). The purpose of the method was to minimize the influence of parameters of the radiative transfer equation that are difficult to determine *in situ*, *e.g.*, backscattering. This method uses two ratios with three different wavelengths ($\lambda_1 = 440$, $\lambda_2 = 490$, and $\lambda_3 = 555$ nm) of R_{rs} to minimize the spectral dependence of the backscattering coefficient, as well as the angular dependence of the underwater light field. Based on the semi-analytical relationship between R_{rs} and b_b/a (Morel and Gentili, 1993) one can derive the following relationship using ratios of three different wavelengths:

$$R_{rs3}(\lambda_1,\lambda_2,\lambda_3) = \frac{R_{rs}(\lambda_1)}{R_{rs}(\lambda_2)} \Big/ \frac{R_{rs}(\lambda_2)}{R_{rs}(\lambda_3)} \simeq \frac{g(\lambda_1)g(\lambda_3)}{[g(\lambda_2)]^2} \frac{b_b(\lambda_1)b_b(\lambda_3)}{[b_b(\lambda_2)]^2} \frac{[a(\lambda_2)]^2}{a(\lambda_1)a(\lambda_3)}. \tag{4.3}$$

As the spectral behaviour of the g parameter is nearly linear over these wavelengths, only a small error is induced by assuming that the triple ratio of g is equal to 1.0. The triple wavelength ratio of the backscattering coefficient in Equation 4.3, evaluated over typical oceanic conditions where the backscattering ranges from particle dominated to water dominated, and where the spectral dependency of particle backscattering ranges from 0 to 2, varies from 0.93 to 1.02. Thus by choosing a constant value equal to 0.975 for the b_b ratio term in Equation 4.3, a maximum error of 4.5% is made for most oceanic conditions.

Substitution of the assumed constant values of g triple ratio (= 1.0) and the backscattering triple ratio (= 0.975) into Equation 4.3 results in a model that can be used to compare directly *in situ* (and modelled) measurements of $R_{rs}(\lambda)$ and $a(\lambda)$.

$$R_{rs3}(\lambda_1, \lambda_2, \lambda_3) \simeq 0.975 \frac{[a(\lambda_2)]^2}{a(\lambda_1)a(\lambda_3)}. \tag{4.4}$$

If functional relationships exist between the absorption coefficients at the selected three wavelengths, such that the absorption at λ_1 and λ_3 can be defined solely in terms of the absorption at λ_2, the above formulation can be used to invert the remotely-sensed reflectance to determine the spectral absorption at the selected three wavelengths.

While any functional form for the spectral absorption coefficient can be utilized, Barnard *et al.* (1999) has shown that the absorption at 440 (originally it was 443 nm) and 555 nm is significantly, linearly correlated to the absorption at 490 nm, such that;

$$\begin{aligned} a(440) &= f_1[a(490)] = \gamma_1[a(490)] + \gamma_2, \\ a(555) &= f_2[a(490)] = \gamma_3[a(490)] + \gamma_4, \end{aligned} \tag{4.5}$$

where values of γ_{1-4} are 1.561, -0.012, 0.319, and 0.067, respectively.

Substitution of these functional forms into Equation 4.4 thus allows for the absorption coefficient at 490 nm (and then at 440 and 555 nm) to be derived solely from $R_{rs}(\lambda)$,

$$a(490) = \frac{-(\gamma_1\gamma_4 + \gamma_2\gamma_3) - \left[(\gamma_1\gamma_4 + \gamma_2\gamma_3)^2 - 4\left(\gamma_1\gamma_3 - \frac{0.975}{R_{rs3}}\right)(\gamma_2\gamma_4)\right]^{0.5}}{2\left(\gamma_1\gamma_3 - \frac{0.975}{R_{rs3}}\right)} \tag{4.6}$$

4.2.2 Results and discussion when applied to the IOCCG data sets

With $R_{rs}(\lambda)$ values at 440, 490 and 555 nm, $a(490)$ and $a(440)$ are calculated from R_{rs3} based on Equations 4.5 and 4.6. Figure 4.2 (also see Tables 4.1 and 4.2) compares model-derived $a(440)$ versus known $a(440)$ values. For the synthetic data, the model-derived values are systematically higher in the lower end ($a(440) < 0.05$ m^{-1}) and systematically lower in the higher end ($a(440) > 0.3$ m^{-1}), indicating a mismatch between data used for algorithm development and data used for test. However, when the algorithm was applied to the *in situ* data set, no such systematic bias was found, although there were 14 points for which no valid results were obtained.

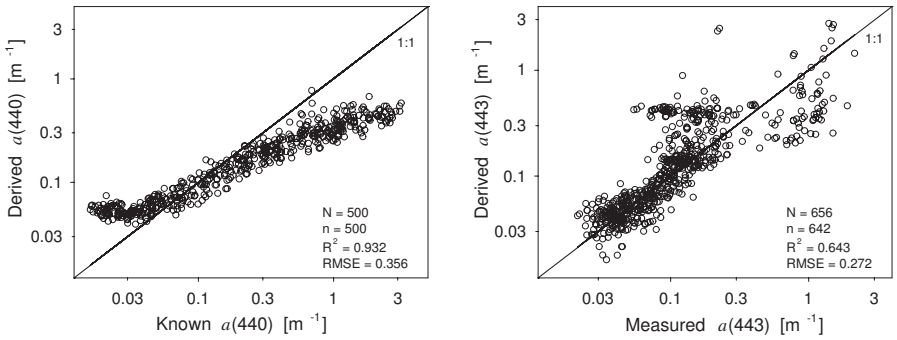

Figure 4.2 Model-derived versus known $a(440)$ (or $a(443)$) values using results from the spectral-curvature algorithm (Barnard *et al.*, 1999). Results for the synthetic data set (left) and the *in situ* data set (right).

4.3 Spectral-Ratio Algorithm with Chlorophyll Concentration as an Intermediate Link

4.3.1 General description

Using chlorophyll-a concentration (C) derived from the spectral-ratio of $R_{\mathrm{rs}}(\lambda)$, and a relationship between K_{d} and C, along with an analytical function that expresses a as a function of K_{d} and R, the value of a can be derived from the spectral ratios of R_{rs} (Morel and Maritorena, 2001). Specifically, values of C are first derived from the current operational chlorophyll algorithm for SeaWiFS (OC4v4) (SeaWiFS, 2000),

$$C = 10^{(a_0+a_1\rho+a_2\rho^2+a_3\rho^3+a_4\rho^4)}, \tag{4.7}$$

where $\rho = \log[\max(R_{\mathrm{rs}}(440, 490, 510))/R_{\mathrm{rs}}(555)]$, and values of a_{0-4} are 0.366, -3.067, 1.93, 0.649, and -1.532, respectively.

$K_d(\lambda)$ can be calculated from Equation 4.7 derived C, (Morel, 1988; Morel and Maritorena, 2001):

$$K_{\mathrm{d}}(\lambda) = K_{\mathrm{w}}(\lambda) + \chi(\lambda)C^{e(\lambda)}, \tag{4.8}$$

with the values of $K_{\mathrm{w}}(\lambda)$, $\chi(\lambda)$ and $e(\lambda)$ known from statistical analysis of field measurements (see Table 2 of Morel and Maritorena, 2001).

Semi-analytically, there is (Morel, 1988; Morel and Maritorena, 2001)

$$a(\lambda) = \frac{0.9K_{\mathrm{d}}(\lambda)[1 - R(\lambda)]}{1 + 2.25R(\lambda)}, \tag{4.9}$$

and

$$R(\lambda) \approx \frac{n_{\mathrm{w}}^2}{t^2} Q R_{\mathrm{rs}}(\lambda). \tag{4.10}$$

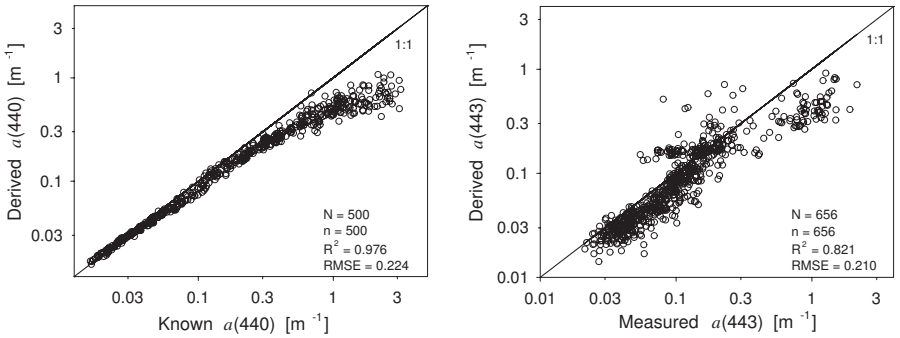

Figure 4.3 Comparison between algorithm-derived and known IOP, using results from the spectral-ratio algorithm with C as an intermediate link (Morel and Maritorena, 2001). Results of $a(440)$ from the synthetic data set (left) and $a(443)$ from the *in situ* data set (right).

Here t is the sea-air transmittance, n_{w} is the index of refraction of the water, and Q (sr) accounts the conversion of irradiance to radiance. The quantity Qn_{w}^2/t^2 represents the conversion between radiance reflectance to irradiance reflectance and the air-sea interface effect, and approximates 6.8 for the remote sensing domain (Morel and Gentili, 1993). Since the value of R is generally less than 0.1 and only plays a secondary role in Equation 4.9, the variation in Qn_w^2/t^2 does not greatly affect the value of $a(\lambda)$ derived by Equation 4.9. Therefore, for a given $R_{\mathrm{rs}}(\lambda)$, absorption coefficients can be calculated following Equations 4.7 to 4.10.

4.3.2 Results and discussion when applied to the IOCCG data sets

With $R_{\mathrm{rs}}(\lambda)$ values at 440, 490, 510 and 555 nm, values of $a(410)$, $a(440)$ and $a(490)$ were calculated from Equations 4.7 to 4.10. The comparison of these derived values versus known (or measured) values is presented in Tables 4.1 and 4.2. Figure 4.3 shows model-derived $a(440)$ with known $a(440)$. Apparently, this empirical procedure performed very well, especially for the synthetic data set with $a(440)$ less than 0.2 m^{-1}. However, this empirical procedure (with the present coefficients) underestimates absorption when the value of $a(440)$ is greater than 0.2 m^{-1}, which may be attributed to the data range used to derive the parameters in Equation 4.7 and Equation 4.8. The difference between model-derived $a(443)$ and known $a(443)$ is larger when applied to the *in situ* data set, as was found for the other two algorithms. In addition, $a(443)$ appears to be underestimated. Even so, an R^2 value of 0.821 and an RMSE of 0.210 were achieved.

4.4 Conclusions

Empirical and semi-empirical algorithms are easy to use and straightforward for data processing. However, since the coefficients used in empirical algorithms are derived from data sets that do not necessarily represent all natural variations, the performance of such algorithms is always subject to compatibility between the waters under study and the waters from which data were obtained for algorithm development. It is critical to examine this compatibility if robust results are desired, and if this kind of algorithm is to be applied to an extensive area.

Chapter 5

Inversion of IOP based on R_{rs} and Remotely Retrieved K_d

Hubert Loisel and Antoine Poteau

5.1 Background

Based on Monte Carlo and Hydrolight simulations we developed an inverse algorithm to retrieve the total absorption, scattering, and backscattering coefficients from the irradiance reflectance just beneath the surface ($R(0^-)$), and the mean vertical diffuse attenuation coefficient over the first optical depth, $<K_d>_1$ (Loisel and Stramski, 2000). Note that while the particulate backscattering coefficient, b_{bp}, is directly obtained from b_b by removing the effect of pure water, our algorithm does not intend to decompose a into its different components such as the absorption by phytoplankton or by coloured dissolved organic matter. This task can be done in a second step (*e.g.*, Chapter 10), by assuming some spectral models for pigments and gelbstoff absorption coefficients, such as those already available in the literature (Kopelevich and Burenkov, 1977; Kirk, 1994; Bricaud *et al.*, 1995), and using least-square fitting methods or equivalent. The major motivation for the development of our algorithm was the assessment of total IOP from basic radiometric measurements by means of a simple and fast approach that does not require any assumption about the spectral shapes of a, b, and b_b. A detailed review of the methods used for solving the hydrologic-optics inverse problem was recently performed by Gordon (2002). One of the differences among these methods concerns the input parameters they use. The choice of $R(0^-)$ and $<K_d>_1$ for our algorithm was motivated by the fact that they can both be estimated from satellite measurements of ocean colour. Whereas $R(0^-)$ is linked to the above surface remote sensing reflectance (R_{rs}) in a fairly straight forward manner (Mobley, 1994), the retrieval of $<K_d>_1$ from space is based on empirical relationships (Mueller, 2000; Loisel *et al.*, 2001b). Therefore, our algorithm does not require any spectral assumptions about IOPs, but does require spectral relationships between $<K_d>_1$ and R_{rs}, in the frame of remote sensing application. However, while $<K_d>_1$ is still empirically determined from R_{rs}, one can imagine a more sophisticated method to retrieve $<K_d>_1$ from space

(such as an iterative scheme based on analytical relationships between $<K_d>_1$ and space retrieved IOP).

Here we test an improved version of our algorithm (Loisel *et al.*, in prep) with the IOCCG data sets (synthetic and *in situ*). After a brief overview of the model, we examine closure between data from both synthetic and *in situ* IOPs, and the retrieval of these IOPs using our model. Finally, these results are discussed, and compared to previous validation studies performed with the Loisel and Stramski (2000) algorithm in various oceanic waters.

5.2 Output and Input Parameters

Output parameters of the model are a, b and b_b averaged over the first attenuation layer. Because the retrieval of b is highly sensitive to the variations in the particle phase function, only a and b_b can be retrieved reasonably well from R_{rs}. For this reason, we will specifically focus on the retrieval of a and b_b at 410, 440, 490, and 550 nm. These wavelengths are common to almost all ocean-colour sensors (with some slight spectral shifts depending on the sensor).

Input parameters of the model are $R(0^-,\lambda)$, $<K_d(\lambda)>_1$, and the sun zenith angle (θ_0). Within the context of ocean colour remote-sensing applications, only $R_{rs}(\lambda)$ is available; both $R(0^-,\lambda)$ and $<K_d(\lambda)>_1$ have to be determined. The exact procedure to assess $R(0^-,\lambda)$ from $R_{rs}(\lambda)$ is given in Loisel and Morel (2001). This step accounts for the process of reflection and refraction of light at the air-water interface, and of the bi-directional effect as described in Morel and Gentili (1993). To estimate $<K_d(\lambda)>_1$ from $R_{rs}(\lambda)$, we originally used an empirical relationship between $<K_d(490)>_1$ and $R_{rs}(490)/R_{rs}(555)$, such as the one developed by Mueller (2000). $<K_d(\lambda)>_1$ was then estimated empirically from $<K_d(490)>_1$. To estimate $a(410)$, $a(440)$, $a(490)$, $b_b(440)$, $b_b(490)$, and $b_b(550)$, we therefore need $R_{rs}(410)$, $R_{rs}(440)$, $R_{rs}(490)$, and $R_{rs}(550)$. Moreover, because of the strong influence of the incident light field at the air-sea interface on the R_{rs}-IOP relationships, our model also accounts for the change of θ_0.

5.3 Assumptions and Description

The radiative transfer simulations used for the development of our model were run for an infinitely deep ocean (no bottom reflected light) with an optically homogenous water column, a nearly flat sea surface with no wind, and the absence of inelastic scattering processes. The phase function was derived from a weighted sum of the molecular scattering and the particle scattering phase functions proposed by Mobley *et al.* (1993). An iterative scheme was also developed for removing the Raman contribution, which is always present in the

natural environment, from $R(0^-)$. This correction will not be applied here for consistency with the other models presented in this report.

Our model is based on the following set of equations between $a(\lambda)$, $b_b(\lambda)$ and $<K_d(\lambda)>_1$, $R(0^-,\lambda)$ which can be applied to any wavelength:

$$a = \frac{\mu_w < K_d >_1}{\left[1 + (2.54 - 6.5\mu_w + 19.89\mu_w^2)\frac{R(0^-)}{1-R(0^-)}\right]^{0.5}}, \tag{5.1}$$

$$b_b = < K_d >_1 10^{\alpha}[R(0^-)]^{\delta}. \tag{5.2}$$

The α and δ functions were given by:

$$\alpha = (-0.83 + 5.34\eta - 12.26\eta^2) + \mu_w(1.013 - 4.124\eta + 8.088\eta^2), \tag{5.3}$$

$$\delta = (0.871 + 0.4\eta - 1.83\eta^2). \tag{5.4}$$

Where η is the ratio of the molecular scattering to the total scattering ($= b_w/b$), and μ_w is the cosine of the refracted solar beam angle just beneath the surface.

Some modifications of the original version of the model are performed for a better retrieval of a and b_b in the context of ocean-colour remote sensing applications (Loisel *et al.*, in prep). These modifications are listed briefly below:

i) The model accounts directly for R_{rs} instead of $R(0^-)$.

ii) We developed a new way to account for the effect of η on the derivation of a and b_b from remote sensing (new parameterisations coupled with an iterative procedure). Note that the dependence of η on the assessment of a was not taken into account in the previous version of our model.

iii) We performed some slight modifications within the a parameterisation to account for some more realistic $\eta - b/a$ combinations at any given wavelength used by ocean-colour sensors.

iv) We used new formulations and parameterisations to determine $<K_d(\lambda)>_1$ from ratios of remote sensing reflectance:

$$q = R_{rs}(440)/R_{rs}(550). \tag{5.5}$$

$$< K_d(\lambda) >_1 = 10^{(\nu_1(\lambda)\log(q)+\nu_2(\lambda))/(\nu_3(\lambda)+\log(q))}. \tag{5.6}$$

ν_{1-3} are empirical parameters and are provided in Table 5.1 for the SeaWiFS bands.

5.4 Results

Using $R_{rs}(\lambda)$ values at 410, 440, 490 and 550 nm, IOPs retrieved from the above steps were compared with known (synthetic) or measured (*in situ*) values.

Table 5.1 Parameters for deriving $<K_d(\lambda)>_1$ from spectral ratio of remote sensing reflectance (Equation 5.6).

	v_1	v_2	v_3
410	-4.7636	-2.1269	3.1752
440	-4.6216	-2.3587	3.1235
490	-3.6636	-2.3116	2.5648
550	-2.0152	-1.5296	1.7751

5.4.1 Comparison with synthetic data

Figure 5.1 as well as Table 5.2 present the performance of our model using $R_{rs}(\lambda)$ and the sun angle as inputs to the calculation of the IOPs. In this case, the sun angle is at 30°. For the absorption coefficient at 410, 440, and 490 nm, the slope of the linear regression is very close to 1.0, and the coefficient of determination is very high ($R^2 \geq 0.94$). The RMSE values are 0.12, 0.119, 0.136, and 0.138 for $a(410)$, $a(440)$, $a(490)$, and $a(550)$, respectively. Note that the performance of the model is slightly degraded at 550 nm compared to other wavelengths.

Table 5.2 RMSE and regression (Type II) results between the derived and the known values of IOP for synthetic data (for $\theta_0 = 30°$). $R_{rs}(\lambda)$ at 410, 440, 490 and 550 nm are used as inputs for the derivation of IOP. N is the number of data tested, while n is the number of valid retrievals.

	N	n	intercept	slope	R^2	RMSE	bias
$a(410)$	500	500	0.029	0.977	0.973	0.120	0.043
$a(440)$	500	500	-0.007	0.990	0.966	0.119	-0.001
$a(490)$	500	500	-0.017	0.980	0.939	0.136	0.000
$a(550)$	500	500	-0.067	0.927	0.818	0.138	-0.002
$b_b(440)$	500	500	-0.173	0.902	0.924	0.123	0.003
$b_b(490)$	500	500	-0.114	0.935	0.917	0.140	0.007
$b_b(550)$	500	500	-0.028	0.973	0.934	0.138	0.023

The retrieval of the absorption coefficient at 550 nm is challenging, as it is strongly dominated by absorption by pure sea water, and because variations of R_{rs} are mostly due to the backscattering coefficient in this spectral domain. The RMSE values for $b_b(\lambda)$ at 440, 490, and 550 nm are very similar to those of $a(\lambda)$, but the slopes differ slightly from 1.0 (0.902, 0.935 and 0.973 at 440, 490, and 550 nm, respectively). Note that the RMSE values for b_b are almost similar for every wavelength. Also, the total absorption and backscattering coefficients are retrieved with the same precision when the sun angle is fixed at 60° (not shown here). Most of the $a(\lambda)$ and $b_b(\lambda)$ errors appear at the high end of the data range, where the retrieval of $<K_d(\lambda)>_1$ from $R_{rs}(\lambda)$ is generally much more doubtful. For instance, by restricting the data set to the $a(440)$ values

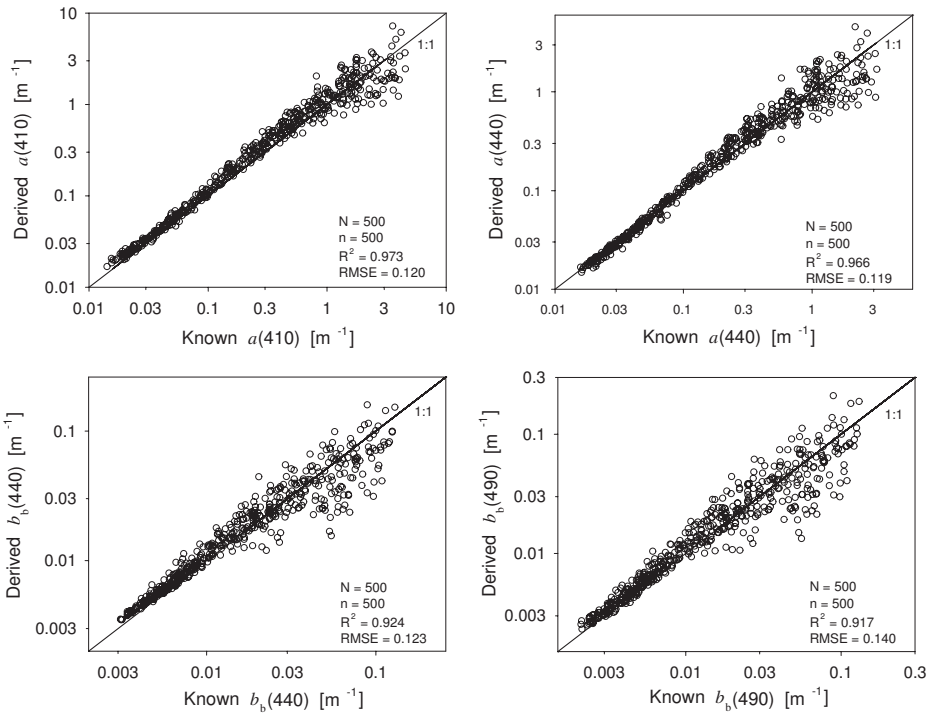

Figure 5.1 Comparison of the derived absorption and backscattering coefficients using the synthetic data set, for a sun zenith angle at 30°, and at different wavelengths. $R_{rs}(\lambda)$ at 410, 440, 490 and 550 nm are used as inputs for the derivation of a and b_b.

lower than 0.3 m^{-1}, which includes most oceanic waters, the RMSE drops by a factor of 2 (from 0.119 to 0.058). The same remark holds at other wavelengths. When measured $<K_d(\lambda)>_1$ is explicitly taken into account as an input parameter, the performance of the model is greatly enhanced. For example, the RMSE for a(410), a(440), a(490), a(550), and b_b(490) are 0.0445, 0.0102, 0.0131, 0.0101, and 0.0324, respectively (not shown here).

5.4.2 Comparison with *in situ* data

Figure 5.2 and Table 5.3 show that there is a reasonably good agreement between the modelled and the measured values of the absorption coefficients, with the RMSE always being lower than 0.2. In the blue-green spectral domain, the mean RMSE value is 0.166. Compared to the synthetic data set, the RMSE increases by a factor of 1.6, 1.6, and 1.24 at 412, 443, and 490 nm, respectively. Note that RMSE drops from 0.169 to 0.142 by restricting the data set to the a(490) values lower than 0.3 m^{-1}. Interestingly, the RMSE at 550 nm is slightly better with the

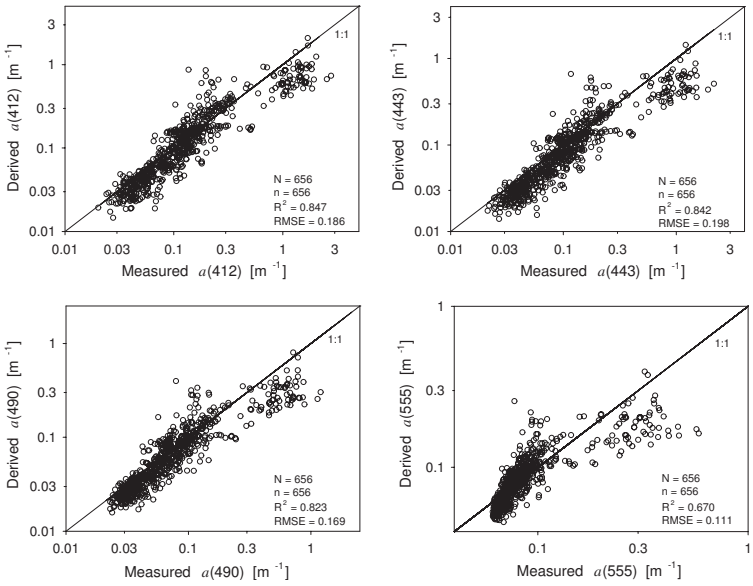

Figure 5.2 Comparison of the derived and the measured total absorption coefficients at different wavelengths, using the *in situ* data set. $R_{rs}(\lambda)$ at 412, 443, 490 and 555 nm are used as inputs for the derivation.

in situ data set than with the synthetic data set.

Table 5.3 RMSE and regression (Type II) results between the derived and the known values of IOP for *in situ* data. $R_{rs}(\lambda)$ at 412, 443, 490 and 555 nm are used as inputs for the derivation of IOP. N is the number of data tested, while n is the number of valid retrievals.

	N	n	intercept	slope	R^2	RMSE	bias
$a(412)$	656	656	-0.052	1.013	0.847	0.186	-0.064
$a(443)$	656	656	-0.108	0.997	0.842	0.198	-0.105
$a(490)$	656	656	-0.122	0.953	0.823	0.169	-0.069
$a(555)$	656	656	-0.126	0.897	0.670	0.111	-0.017

5.5 Conclusions

The retrieval of both $a(\lambda)$ and $b_b(\lambda)$ is achieved with excellent accuracy in the blue green spectral region when both $R(0^-)$ and $<K_d>_1$ are measured (the mean RMSE value in this spectral domain is 0.0195 for the absorption coefficient). When only R_{rs} is available as an input parameter, the results are obviously degraded, but are still very satisfactory: for the synthetic data set, the mean RMSE value over the blue-green part of the spectrum for a and b_b is 0.128 and 0.134,

respectively. When comparing with *in situ* data, we should emphasise that our model is able to predict a with a mean RMSE value of 0.166 over the spectral domain of interest for ocean-colour related studies. The performance of our model is governed, to a certain extent, by the accuracy of the $<K_d>_1$ assessment from space. Different approaches have been tested to improve the retrieval of $<K_d(\lambda)>_1$ from $R_{rs}(\lambda)$ (Loisel *et al.*, in prep). Preliminary results for the retrieval of both a and b_b are very promising.

The results presented here are consistent with previous comparisons performed in oceanic and coastal waters (Loisel *et al.*, 2001b; Melin et al., 2002; Dupouy *et al.*, 2003). For example, based on field data collected in waters off southern California, and in waters surrounding Europe, Loisel *et al.* (2001b) showed that the average value and the standard deviation of the relative difference between the measured and the retrieved absorption coefficients from 412 to 555 nm are 26% and 16%, respectively. The new version of the model significantly improves the retrieval of a and b_b, especially in the green part of the spectrum and at the extreme values (Loisel *et al.*, in prep).

Chapter 6

The MERIS Neural Network Algorithm

Roland Doerffer and Helmut Schiller

6.1 Introduction

In this chapter we present the results of the MERIS Case 2 water algorithm for the IOCCG algorithm inter-comparison. This algorithm is an artificial neural network (aNN) inversion procedure (Doerffer *et al.*, 2002; Doerffer and Schiller, 2000; Schiller and Doerffer, 2005; Doerffer and Schiller, 2006), which is used in the ground segment processor of MERIS. This instrument is operated on board the Earth observation satellite ENVISAT of the European Space Agency (ESA), which was launched on 1 March 2002. The aNN algorithm was selected because of its capability to invert directional water-leaving radiance reflectance directly into absorption and scattering coefficients or concentrations of different constituents present in coastal waters, with high efficiency for mass production. Due to the fixed architecture of the aNN, only the simulated IOCCG data set could be processed for inter-comparison.

6.2 Description of the MERIS Case 2 Water Algorithm

The MERIS Case 2 water algorithm is a neural network, which takes the log of the above-surface remote-sensing reflectance (R_{rs}, which is the directional water leaving radiance divided by the downwelling irradiance) of eight of the fifteen MERIS bands (*i.e.* after atmospheric correction, Bands 1-7 and Band 9) as well as three angles (solar zenith, viewing zenith, azimuth difference) as input and provides the log of the following three optical coefficients as output: pigment absorption ($a_{ph}(442)$), absorption of gelbstoff and bleached suspended matter ($a_{dg}(442)$), and scattering coefficient of all particles ($b_{p}(442)$), all at 442 nm (MERIS Band 2). The optical coefficients are then used to compute the concentrations of chlorophyll-a and total suspended matter dry weight. Together with the gelbstoff absorption, these are the three Case 2 water products of MERIS. However, by using the inverse of the conversion factors it is also easy to go back one step and compute the three IOPs from the concentrations again, as well as

the total absorption and scattering.

The neural network is trained with simulated R_{rs} spectra. About 30,000 spectra are used to cover a large range from Case 1 and Case 2 waters as well as different observation and solar angles (see Table 6.1). The simulation of $R_{rs}(\lambda)$ is performed using Hydrolight radiative transfer model. The model is set up in the following way:

- No bottom reflection
- Homogenous vertical distribution of water constituents
- No inelastic scattering
- Waves according to a wind speed of 3 m s^{-1}

Standard clear atmosphere with oceanic aerosol and different solar zenith angles (0 - 80° from zenith) was used to simulate incoming solar light. The detector captures the directional, water-leaving radiance and downwelling irradiance just above the surface, for computing the directional R_{rs}. For the comparison here, only the nadir R_{rs} was used. The part controlling the success of the simulation and training of the aNN is the bio-optical model. For the MERIS aNN algorithm, it is based on measurements of the IOPs, *i.e.* absorption and scattering. These data are mainly from European waters, dominated by measurements in the North Sea.

Table 6.1 Variability and range of the optical properties used for the simulation of water-leaving radiance reflectance spectra that were used to train the aNN.

Component/Property	**Value Range**
Gelbstoff absorption wavelength exponent [nm^{-1}]	0.014 ± 0.002
Bleached particle absorption wavelength exponent [nm^{-1}]	0.008 ± 0.005
Particle scattering wavelength exponent	0.4 ± 0.2
White particle scattering wavelength exponent	0.0
Phytoplankton pigment absorption spectra	random selection from > 200 absorption spectra, normalized at 442 nm (MERIS Band 2)
Gelbstoff absorption (a_g) at 442 nm [m^{-1}]	0.005 - 5.0
Particle scattering (b_p) at 442 nm [m^{-1}]	0.005 - 30.0
White particle scattering (b_{pw}) at 442 nm [m^{-1}]	0.005 - 30.0
Phytoplankton pigment absorption (a_{ph}) at 442 nm [m^{-1}]	0.001 - 2.0
Minimum particle scattering at 442 nm [m^{-1}]	0.25 $a_{ph}(442)$
Bleached particle absorption	0.1 $b_p(442)$ + $\delta^{\dagger}$ 0.03 $b_p(442)$
Sun zenith angle [degree]	0 - 80
Viewing zenith angle [degree]	0 - 50
Difference between sun and viewing azimuth angle [degree]	0 - 180

†– δ is a random value in the range of 0-1

The bio-optical models used here represent mean conditions and variabilities (see Table 6.1). For each case of the simulations, the optical properties are varied

randomly according to the standard deviations of the measured absorption and scattering spectra. For the absorption of gelbstoff (a_g) and bleached particles (a_d) as well as for the total particle scattering (b_p), the wavelength exponent is varied according to the measured standard deviations. For the absorption spectra of phytoplankton pigments ($a_{ph}(\lambda)$), one out of 223 different measured spectra is selected randomly for each simulation. The absorption and scattering coefficients at 442 nm are randomly selected from the range using the log scale (see Table 6.1), while the viewing and sun angles are selected randomly using the linear scale. The simulated spectra are furthermore randomly degraded using an estimated error of the instrument and the atmospheric correction. Any R_{rs} spectrum that is out of the training range is detected using a forward neural network. This network takes the optical coefficients from the first backward network as input to compute a R_{rs} spectrum. This spectrum is then compared with the measured one. If the Chi^2 deviations of all eight bands are above a certain level (Doerffer and Schiller, 2000), the spectrum is classified as out of the training range. However, this test was not used for the IOCCG data sets.

Uncertainties in atmospheric correction over water with low water-leaving radiance sometimes result in negative reflectance. These incorrect values can easily be excluded from the neural network by introducing a cut-off. In the MERIS aNN algorithm, this cut-off was set to a R_{rs} value of 0.000955 sr^{-1}. All reflectance values below this threshold are clipped to this value. The neural network is trained in the same way.

6.3 aNN Results with the IOCCG Data Sets

The aNN algorithm we have tested here has five hidden layers with 45, 16, 12, 8 and 5 neurons respectively. It is the algorithm which is presently used for reprocessing all the MERIS data (Doerffer and Schiller, 2006). $a_{ph}(442)$, $a_{dg}(442)$ and $b_{bp}(442)$ (which is assumed to be 1.5% of $b_p(442)$) were retrieved by applying this algorithm to the IOCCG data sets. Note that, due to wavelength mismatch, the aNN algorithm (designed specifically for MERIS) was not applied to the *in situ* part of the IOCCG data sets. Before applying the aNN algorithm, the reflectance spectra for the MERIS bands were linearly interpolated from the data set, which has a 10 nm spacing. Also the optical properties of the test data set were interpolated for 442 nm. It should be pointed out that although the IOCCG synthetic data set was also simulated with Hydrolight radiative transfer code, it was nevertheless computed totally independently from the data used for training the aNN. The two data sets are completely independent and are based on independent bio-optical models, which explains at least part of the deviations.

Figure 6.1 compares the derived properties (for data of 30° solar zenith angle) with their corresponding known values, while Table 6.2 summarizes results from

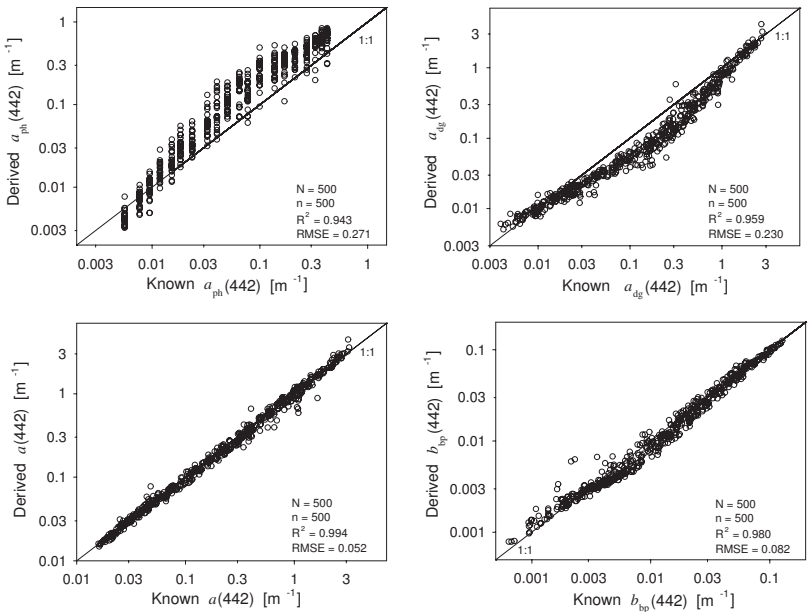

Figure 6.1 Comparison between aNN derived IOPs and the known IOPs, for the IOCCG synthetic data set (the Sun at 30° from zenith). aNN used R_{rs} values at 412, 442, 490, 510, 560, 617, 665 and 708 nm to retrieve the IOPs.

statistical analyses. For the entire range of total absorption and backscattering coefficients the RMSE values are 0.052 and 0.082 (see Table 6.2), respectively, with slope values nearly 1.0. Similar results were also obtained for the synthetic data set with the Sun at 60° from zenith (not shown here).

Table 6.2 RMSE and regression (Type II) results for the synthetic data set (30° solar zenith angle). IOPs were retrieved with R_{rs} values at 412, 442, 490, 510, 560, 617, 665 and 708 nm. N is the number of data tested, while n is the number of valid retrievals.

	N	n	Intercept	slope	R^2	RMSE	bias
$a_{dg}(442)$	500	500	-0.210	0.959	0.959	0.230	-0.174
$a_{ph}(442)$	500	500	0.407	1.163	0.943	0.271	0.202
$a(442)$	500	500	-0.009	1.006	0.994	0.052	-0.013
$b_{bp}(442)$	500	500	-0.038	0.993	0.980	0.082	-0.024

These results indicate that the aNN algorithm accurately retrieved those optical properties that determine the remote sensing reflectance. When the total absorption is decomposed into the components of water, gelbstoff and phytoplankton pigments, the scatter is much larger (RMSE values are 0.230 and 0.271 for $a_{dg}(442)$ and $a_{ph}(442)$, respectively) and the relationships deviate from lin-

earity in the middle concentration range. The scatter is obviously due to the fact that the bio-optical models used for the IOCCG synthetic data set are different from those used for training the aNN. This is presumably also true for the maximum difference in the middle of the data range. Since this is also normally the case in nature, it indicates that total absorption and total backscattering are more robust variables, which should be derived from reflectance spectra in addition to other IOPs or concentrations of different water constituents.

Chapter 7

The Linear Matrix Inversion Algorithm

Paul Lyon and Frank Hoge

7.1 Background

The Linear Matrix Inversion (LMI) algorithm was developed by Hoge and Lyon (1996). This algorithm uses remote-sensing reflectance at three wavelengths to simultaneously derive three major unknowns algebraically. Due to its linear matrix nature, it is efficient in processing satellite images. In the past decade, this algorithm has been applied to data taken from many regions around the world (Hoge and Lyon, 1996; Hoge and Lyon, 1999; Hoge *et al.*, 2001). Nevertheless, since some of the parameters used in the algorithm were developed based on measurements made mainly from the Mid Atlantic Bight and off the East Coast of the United States, further refinement and improvement is expected in the coming years.

7.2 Inputs of LMI

The algorithm uses remotely sensed reflectance, R_{rs}, propagated through the air/ water interface, into semi-analytic reflectance model developed by Gordon *et al.* (1988). The present version of the algorithm that is optimized for use with satellite data uses only three inputs, $R_{rs}(412)$, $R_{rs}(490)$ and $R_{rs}(555)$. The algorithm also has four empirical parameters, described below, that determine the spectral shapes of the individual IOP spectrum.

7.3 Basic Assumptions of LMI

There are three assumptions that are fundamental to this inversion technique. First, it is assumed that the semi-analytic equation, shown in Equation 7.1, is a good description of the relationship between the IOPs and the reflectance over a wide range of environments. Second, it is assumed that globally, the optically significant varying IOPs are absorption coefficients of phytoplankton and

CDOM (including detritus), and backscattering coefficient of all particles (scattering constituents other than water). Thus, an algorithm based on properly formulated spectral models of these three principal IOPs may be applied to many different water masses. And, third, it is assumed that, using a proper combination of wavelengths, the three major IOPs can be resolved if the following conditions are met. The wavelengths used should maximize the mathematical differences between the spectral shapes of the three IOPs. And, within each IOP, a stable spectral dependence must be maintained or the modulations of the IOP spectral shapes need to be empirically adjusted to reflect their natural variability.

7.4 Approach

7.4.1 Algorithm mathematical description

As stated above, the algorithm is based on the reflectance model developed by Gordon *et al.* (1988),

$$r_{rs} = g_1 \left(\frac{b_b}{b_b + a} \right) + g_2 \left(\frac{b_b}{b_b + a} \right)^2. \tag{7.1}$$

Here r_{rs} is the subsurface remote-sensing reflectance, which can be easily calculated from the remote-sensing reflectance (R_{rs}) provided by any sensor. $g_1 = 0.0949$ and $g_2 = 0.0794$ are model parameters for r_{rs} (Gordon *et al.*, 1988). b_b and a are the total backscattering coefficients and total absorption coefficient, respectively. Defining u as

$$u \equiv \frac{b_b}{b_b + a}, \tag{7.2}$$

we get a quadratic equation with u as the variable,

$$g_2 u^2 + g_1 u - r_{rs} = 0, \tag{7.3}$$

which can easily be solved for u using the quadratic formula. Since b_b is a sum of b_{bw} and b_{bp}, a is a sum of a_w, a_{ph}, and a_{dg}, and a_w and b_{bw} are known constants, a linear system with a_{ph}, a_{dg} and b_{bp} as variables can then be constructed by re-arranging u (Hoge and Lyon, 1996):

$$a_{ph}(\lambda) + a_{dg}(\lambda) + b_{bp}(\lambda)\nu(\lambda) = -a_w(\lambda) - b_{bw}(\lambda)\nu(\lambda), \tag{7.4}$$

with

$$\nu \equiv 1 - \frac{1}{u}. \tag{7.5}$$

For an exact solution, three different wavelengths are used to form a system of three equations with three unknowns. After spectrally modeling the three

IOP variables with values at a reference wavelength (λ_r = 410 nm) the equation becomes,

$$a^{\diamond}_{\mathrm{ph}}(\lambda)a_{\mathrm{ph}}(\lambda_r) + a^{\diamond}_{\mathrm{dg}}(\lambda)a_{\mathrm{dg}}(\lambda_r) + b^{\diamond}_{\mathrm{bp}}(\lambda)b_{\mathrm{bp}}(\lambda_r)\nu(\lambda) = -a_{\mathrm{w}}(\lambda) - b_{\mathrm{bw}}(\lambda)\nu(\lambda). \tag{7.6}$$

Here $a^{\diamond}_{\mathrm{ph}}(\lambda)$, $a^{\diamond}_{\mathrm{dg}}(\lambda)$ and $b^{\diamond}_{\mathrm{bp}}(\lambda)$ represent the normalized optical properties at λ_r (see section 7.4.2). Equation 7.6 can now be used to construct the linear matrix that could be inverted to derive the IOPs consistent with the input R_{rs} and the spectral models,

$$\begin{bmatrix} 1 & 1 & \nu(\lambda_r) \\ a^{\diamond}_{\mathrm{ph}}(\lambda_2) & a^{\diamond}_{\mathrm{dg}}(\lambda_2) & b^{\diamond}_{\mathrm{bp}}(\lambda_2)\nu(\lambda_2) \\ a^{\diamond}_{\mathrm{ph}}(\lambda_3) & a^{\diamond}_{\mathrm{dg}}(\lambda_3) & b^{\diamond}_{\mathrm{bp}}(\lambda_3)\nu(\lambda_3) \end{bmatrix} \begin{bmatrix} a_{\mathrm{ph}}(\lambda_r) \\ a_{\mathrm{dg}}(\lambda_r) \\ b_{\mathrm{bp}}(\lambda_r) \end{bmatrix} = - \begin{bmatrix} a_{\mathrm{w}}(\lambda_r) + b_{\mathrm{bw}}(\lambda_r)\nu(\lambda_r) \\ a_{\mathrm{w}}(\lambda_2) + b_{\mathrm{bw}}(\lambda_2)\nu(\lambda_2) \\ a_{\mathrm{w}}(\lambda_3) + b_{\mathrm{bw}}(\lambda_3)\nu(\lambda_3) \end{bmatrix}. \tag{7.7}$$

Note that the inverse matrix must be computed for each data point since input data, $R_{\mathrm{rs}}(\lambda)$, is on both sides of the equation (contained in $\nu(\lambda)$). Any standard method of solving this system of equations can be used. The Hoge/Lyon inversion algorithm uses lower/upper deconvolution (Hoge and Lyon, 1999).

7.4.2 IOP spectral models

To mathematically solve Equation 7.7, spectral models are required for the three IOP variables. It is important to select wavelengths where each IOP tends to co-vary among wavelengths (Hoge and Lyon, 1996). Based on many different published phytoplankton absorption spectra, phytoplankton absorption coefficients at 412, 490 and 555 nm are found to co-vary well. A Gaussian function centered at 443 nm, with a full-width at half max (FWHM) of 70 nm (σ in Equation 7.8 below) is used to model $a_{\mathrm{ph}}(\lambda)$. No improvement in the retrieved IOPs was found when the FWHM parameter σ was empirically varied.

$$a_{\mathrm{ph}}(\lambda) = a_{\mathrm{ph}}(\lambda_r)e^{\left[\frac{\lambda_r^2 + 886(\lambda-\lambda_r) - \lambda^2}{2\sigma^2}\right]}. \tag{7.8}$$

The combined absorption coefficient of detritus and gelbstoff, $a_{\mathrm{dg}}(\lambda)$, is modelled with an exponential decay function (Bricaud *et al.*, 1981; Roesler *et al.*, 1989; Carder *et al.*, 1991):

$$a_{\mathrm{dg}}(\lambda) = a_{\mathrm{dg}}(\lambda_r)e^{-S(\lambda-\lambda_r)}. \tag{7.9}$$

S is the spectral slope and is set to 0.018 (nm^{-1}) for all inversions discussed within this chapter.

The total particulate backscattering coefficient, $b_{\mathrm{bp}}(\lambda)$ is modelled as a power-law function of wavelength,

$$b_{\mathrm{bp}}(\lambda) = b_{\mathrm{bp}}(\lambda_r)\left(\frac{\lambda_r}{\lambda}\right)^{Y}, \tag{7.10}$$

with exponent Y empirically estimated as follows,

$$Y = m_1 \frac{R_{rs}(490)}{R_{rs}(555)} + m_2. \tag{7.11}$$

Sensitivity studies have found that the magnitude of parameter Y affects the b_{bp} and the a_{dg} retrievals more than the a_{ph} retrievals (Hoge and Lyon, 1996). The empirical parameters, $m_1(0.8)$ and $m_2(0.2)$ have been optimized for use with global satellite data, such that errors in the derived IOPs caused by this equation are minimized in a global sense. These parameters can also have regional values to achieve better regional results.

7.5 Results

7.5.1 Synthetic data set

Figure 7.1 shows the agreement between known and derived IOPs. There is a logarithmic offset in the $a_{ph}(410)$ retrievals and several outliers, yet the agreement is evident as shown in Table 7.1 by the correlation of determination (R^2) of 0.877 (n = 484) and the slope close to 1.0, and an RMSE of 0.222. Note that the statistics presented in Table 7.1 are affected by the outliers that lie below the one-to-one line, so that the larger population above the line could still be corrected by using an offset in log space. This infers, of course, that regional or specific tuning of this and any algorithm may improve its performance for similar settings.

Table 7.1 RMSE and regression (Type II) results of the synthetic data set ($\theta_0 = 30°$). IOPs were retrieved with R_{rs} values at 410, 490 and 550 nm as inputs. N is the number of data tested, while n is the number of valid retrievals.

	N	n	intercept	slope	R^2	RMSE	bias
$a_{ph}(410)$	500	484	0.053	0.989	0.877	0.222	0.068
$a_{ph}(490)$	500	484	0.114	0.997	0.891	0.23	0.118
$a_{dg}(410)$	500	484	0.069	1.052	0.958	0.161	0.03
$a_{dg}(490)$	500	484	-0.032	1.051	0.921	0.236	-0.095
$a(410)$	500	484	0.067	1.036	0.964	0.14	0.045
$a(490)$	500	484	0.012	1.007	0.942	0.133	0.005
$b_{bp}(410)$	500	484	0.043	1.019	0.922	0.15	0.007
$b_{bp}(490)$	500	484	0.008	1.018	0.936	0.149	-0.027

The agreement between input and output $a_{dg}(410)$ is better than that of $a_{ph}(410)$, with an R^2 of 0.958 and slope about 1.1, and RMSE of 0.16 (Table 7.1). Much better results are achieved for the total absorption and particle backscattering coefficients, with both R^2 and slope values close to 1.0 and RMSE of 0.14 and 0.15, respectively.

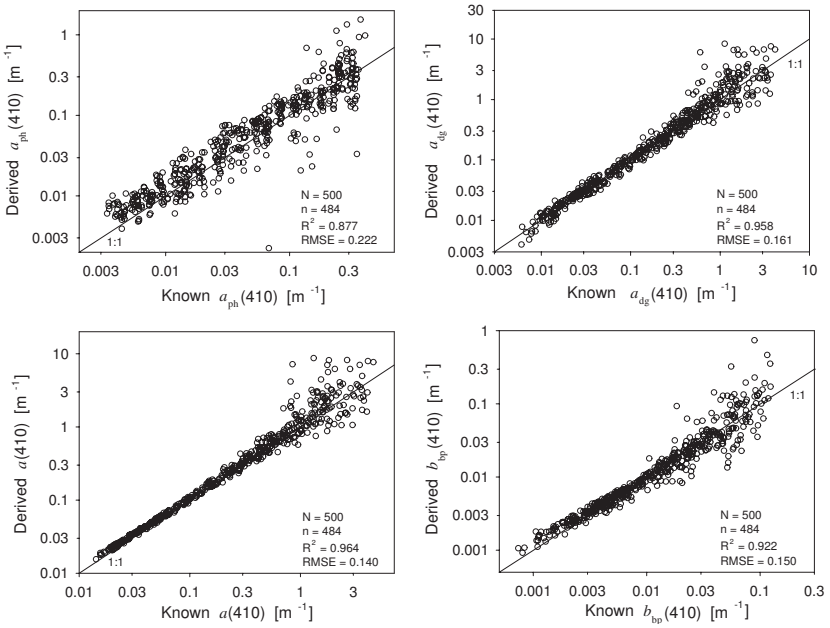

Figure 7.1 Comparison between retrieved and simulated IOPs for a sun zenith angle of 30°. IOPs were retrieved using R_{rs} values at 410, 490 and 550 nm.

The smaller number (n) in the statistics analysis (Table 7.1 and Table 7.2) represents all the data points that the inversion successfully processed (all IOPs with values greater than zero, or where the output $a(410) < 10.0$ m^{-1}). Data points with negative IOP retrievals were excluded from the statistics and the figures, as they are physically unrealistic values that are filtered out automatically. In normal operation of the linear matrix inversion, retrievals where $a_{dg}(410) >$ 1.0 m $^{-1}$ or $a_{ph}(410) > 1.0$ m $^{-1}$ are considered suspect. To allow readers to compare the results of this algorithm with those of other techniques discussed in this report, however, inversions with $a(410)$ with values up to 10.0 m^{-1} are included in the figures and tables.

7.5.2 *In situ* data set

For the *in situ* data set, the regression statistics are provided in Table 7.2. Retrieved $a_{ph}(412)$, $a_{dg}(412)$, $a(412)$ and $a(490)$ are compared with their measured values respectively in Figure 7.2. There were no *in situ* b_{bp} data for comparison.

Apparently the retrievals of a_{ph} and a_{dg} scattered much more than that of the simulated data set. This might be due to the measurement uncertainties that are common in field-measured data. Also, large portions of the data were taken in coastal waters, and real *in situ* properties may not follow the limited

Table 7.2 RMSE and regression (Type II) results of the *in situ* data set. IOPs were retrieved with R_{rs} values at 412, 490 and 555 nm as inputs. N is the number of data tested, while n is the number of valid retrievals.

	N	n	intercept	slope	R^2	RMSE	bias
$a_{ph}(412)$	656	642	0.336	1.208	0.654	0.332	0.02
$a_{ph}(490)$	656	642	0.454	1.231	0.686	0.325	0.078
$a_{dg}(412)$	656	642	-0.142	1.007	0.653	0.325	-0.149
$a_{dg}(490)$	656	642	-0.315	0.98	0.599	0.427	-0.284
$a(412)$	656	642	-0.082	0.96	0.872	0.163	-0.045
$a(490)$	656	642	-0.035	0.994	0.804	0.168	-0.028

combinations of spectral shapes used in the simulated data set.

Again, better results are obtained for the total absorption coefficients. This suggests that it is easier to retrieve the total absorption using this technique than it is to resolve the separate components of the total absorption.

7.6 Discussion

7.6.1 Overall results of the linear matrix inversion algorithm

As described above, the retrievals of the total absorption are quite good for both *in situ* and simulated data sets. The separation of the absorption into contributions from phytoplankton and dissolved organic matter are less accurate, but still retrieved well. The spectral model parameters used in the linear inversion of both simulated and *in situ* data sets preformed well in spite of the fact that the true spectral shapes at the wavelengths used in the inversions varied over dramatic ranges, as shown in Figure 7.1. These results demonstrate that an exact solution derived from a 3-by-3 inversion, can be optimized to retrieve IOPs at a reference wavelength. The linear inversion method has both weaknesses and strengths associated with its use, which are briefly described below.

7.6.2 Algorithm weaknesses

One set of weakness in this algorithm is related to the parameterisation of the IOP spectral shapes. For example, the empirically adjusted b_{bp} spectral model and the fixed spectral models for a_{ph} and a_{dg} will not properly represent all combinations of water constituents, especially when contributions from optically significant constituents not well described by the three IOP basis vectors are present. The fixed spectral shape of a_{ph} limits the accuracy of IOP retrievals since true phytoplankton absorption spectra vary dramatically (*e.g.*, Hoepffner and Sathyendranath, 1991), however, the selection of covarying wavelengths reduces the impact of the high variability of other wavelengths. Also, the a_{dg}

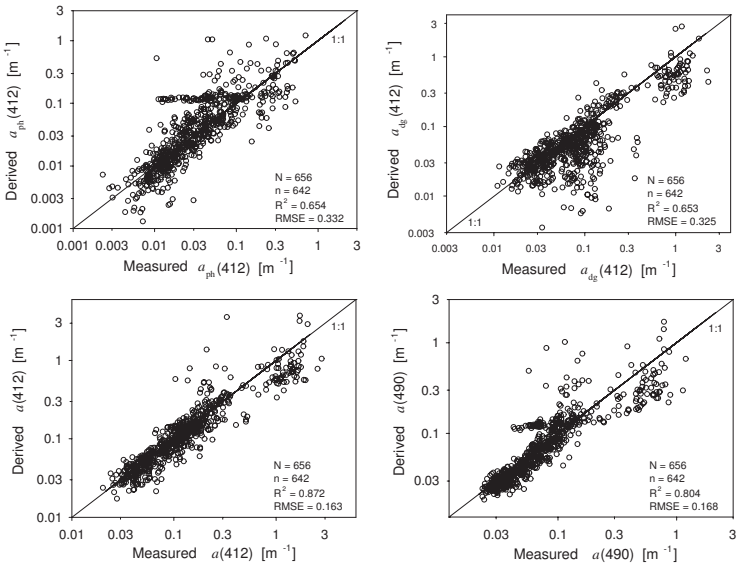

Figure 7.2 Comparison between retrieved and *in situ* IOPs. IOPs were retrieved using R_{rs} values at 410, 490 and 555 nm.

spectral slope coefficient, S, should be varied with type of water mass, but at this point, no parameterization of S with an *a priori* data value has improved the retrievals of a_{dg}.

As shown in Figures 7.1 and 7.2, the algorithm has been optimized to retrieve values at 412nm. The IOPs derived at 412 nm can be translated to any other wavelength through the IOP spectral models but the accuracy of the values derived at the other wavelengths will be driven by how well the spectral models reflect the true characteristics of the in-water constituents, which is true of any spectral model-based algorithm. Methods developed by Wang *et al.* (2005) could be implemented to help describe the range of equally valid retrievals of IOPs.

The need for the 412 nm band to separate the CDOM absorption from the phytoplankton absorption exposes the algorithm to potentially large errors in input $R_{rs}(412)$, caused by the fact that in coastal regions accurate atmospheric correction at the shorter wavelengths is very difficult to achieve. This is a fundamental problem for all semi-analytical algorithms that attempt to use $R_{rs}(412)$ to separate phytoplankton and CDOM absorption coefficients.

7.6.3 Algorithm strengths

There are also several advantages gained by using the exact linear inversion approach. The most important feature is that the algorithm limits errors in IOP spectral models by using wavelengths where each IOP tends to co-vary. This

approach is selected to optimize the algorithm for application to global data sets. Hyper-spectral data was tested and it was found that the best agreement between the retrieved IOPs and truth data was achieved by using the fewest number of co-varying wavelengths possible. Therefore, the SeaWiFS bands, 412, 490 and 555 nm, or the closest to those bands on other sensors, are used in this algorithm. By using this simplified approach, we sacrifice deriving information about more constituents in the water but minimize the errors caused by poor spectral models to describe highly variable portions of the IOP spectra, and great variability of water mass types on a global scale.

The inversion is computationally fast and no iteration is needed. Large data set processing is limited more by the rate of data to be read and written to a disk, than by the computation of the IOP outputs.

Inputs from several different satellites that are contemporaneous and geographically coincident can be used in the inversion to produce a multi-satellite blended product. In this case, the same three wavelengths (or similar wavebands) are used from each satellite to realize the benefit of averaging out the asymmetrical errors in R_{rs} in an over determined linear inversion, while still maintaining the inter-wavelength co-variance for each IOP.

With fewer spectral model parameters to adjust, the algorithm is easy to tune given known or expected values. This allows for tuning of the algorithm to specific regions where characteristics of constituents in the water are constrained temporally and spatially, so regionally optimized versions of the algorithm can be developed, without changing the core mathematical implementation.

Chapter 8

Over Constrained Linear Matrix Inversion with Statistical Selection

Emmanuel Boss and Collin Roesler

8.1 General Description

Semi-analytic inversions of remotely-sensed reflectance have been available since 1995 (Roesler and Perry, 1995). However, a procedure that provides an uncertainty of the inverted parameter for each individual spectrum based on uncertainties in the remote-sensing data and the model has only recently been devised (Wang *et al.*, 2005).

We use the same model philosophy as in Wang *et al.* (2005) with a slight modification (we use a single phytoplankton absorption spectrum). We assume a known relationship between r_{rs} and the absorption and backscattering coefficients (Gordon *et al.*, 1988):

$$r_{rs}(\lambda) = \frac{L_u(\lambda, 0^-)}{E_d(\lambda, 0^-)} = 0.0949\frac{b_b(\lambda)}{a(\lambda) + b_b(\lambda)} + 0.0794\left(\frac{b_b(\lambda)}{a(\lambda) + b_b(\lambda)}\right)^2. \quad (8.1)$$

The quadratic form is important for high $r_{rs}(\lambda)$ values (Garver and Siegel, 1997). Gordon *et al.* (1988) estimated that the model errors in Equation 8.1 are less than 10%.

The total absorption coefficient is partitioned as follows:

$$a(\lambda) = a_w(\lambda) + a_{ph}(\lambda) + a_{dg}(\lambda), \quad (8.2)$$

where the subscripts "w", "ph", and "dg" designate sea water, phytoplankton, and the combined contribution of CDOM and detrital material. The spectral absorption coefficient for sea water, $a_w(\lambda)$, is computed for given salinity and temperature based on Pope and Fry (1997) and Pegau *et al.* (1997).

The spectral absorption coefficient of phytoplankton is assumed to be:

$$a_{ph}(\lambda) = a_{ph}(\lambda_0)a^+_{ph}(\lambda), \quad (8.3)$$

where $a^+_{ph}(\lambda)$ is an average of normalized phytoplankton absorption spectra (Roesler and Perry, 1995) and λ_0 is commonly set as 440 nm.

The spectral absorption coefficient of the combined absorption by CDOM and detritus is:

$$a_{dg}(\lambda) = a_{dg}(\lambda_0)\exp(-S(\lambda - \lambda_0)), \tag{8.4}$$

where S is the spectral slope of the combined absorption coefficient. This function has been found to be an adequate representation of measured CDOM and detritus absorption coefficient with S ranging between 0.008 to 0.023 nm^{-1} (e.g., Roesler *et al.*, 1989).

The total backscattering coefficient, $b_b(\lambda)$, is approximated by

$$b_b(\lambda) = b_{bw}(\lambda) + b_{bp}(\lambda). \tag{8.5}$$

The spectral backscattering coefficients of sea water ($b_{bw}(\lambda)$) are computed for a given salinity based on the interpolation of the data of Morel (1974) as in Boss and Pegau (2001).

The spectral particle backscattering coefficient is assumed to obey:

$$b_{bp}(\lambda) = b_{bp}(\lambda_0)(\lambda/\lambda_0)^{-Y}. \tag{8.6}$$

This formulation is consistent with many previous studies, though without in-water validation.

To account for variability in space and time of the spectral shapes of the IOPs we perform the r_{rs} inversion allowing the shape parameters (spectral slope S and spectral slope Y) to vary within most of their observed range of variability ($0.01 \le S \le 0.02$, $0 \le Y \le 2$). For each parameter we use 11 different values with equal intervals between their maximum and minimum, resulting in $11^2 = 121$ different inversion computations for each r_{rs}.

It can be shown that with known spectral shapes, Equation 8.1 can be solved to obtain $b_{bp}(\lambda_0)$, $a_{dg}(\lambda_0)$, and $a_{ph}(\lambda_0)$ using a linear matrix inversion technique (Hoge and Lyon, 1996). When the number of wavelengths exceeds the number of unknowns (3 in our case), this solution is the best solution in a least-square sense (Press, 1992).

From all the solutions to Equation 8.1 we select the solution for which $a_{dg}(440)$ and $a_{ph}(440) > -0.005$ m^{-1} and $b_{bp}(440) > -0.0001$ m^{-1} (slightly negative values are accepted to compensate for finite uncertainties in measurements and calibrations). We further restrict ourselves to the solutions whose reconstructed r_{rs} (calculated by substituting the solutions into Equation 8.1) obeys:

$$|r_{rs,reconstucted}(\lambda) - r_{rs,known}(\lambda)|/r_{rs,known}(\lambda) < 0.1 \text{ or } 0.2 \text{ for every } \lambda.$$

These criteria can result in cases where no solution could be found for a given r_{rs}. The choice of the criteria should be driven by knowledge of uncertainties in observed r_{rs} as well as the assumed spectral shapes (in particular that of phytoplankton).

We thus present the results from the two different solution selection criteria in the tables, but only the criteria of 0.1 in the plots. We provide uncertainties for the solutions on the plots based on the distance between the 84th and 16th percentile of the obtained solutions (~ ± one standard deviation for a normal distribution).

Given the application to remote sensing we used only the R_{rs} values at 410, 440, 490, 510 and 550 nm (or nearby for the *in situ* data set).

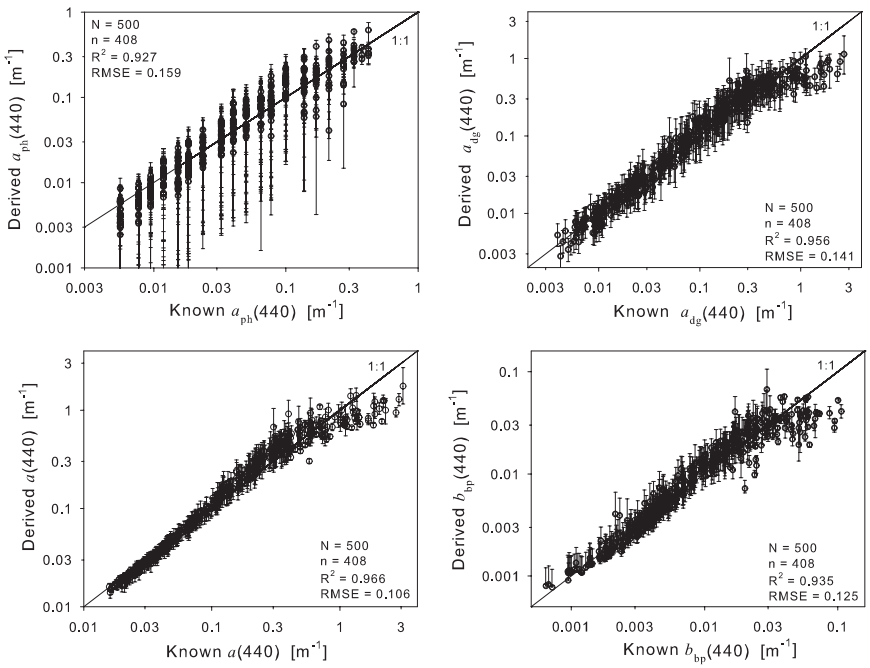

Figure 8.1 Comparison of inverted and the simulated data set (Sun at 30^{o} from zenith) for $a_{ph}(440)$, $a_{dg}(440)$, $a(440)$, and $b_{bp}(440)$ for the 10% criteria (statistics in Table 8.1). Vertical lines denote the 90% confidence intervals in the solutions. R_{rs} values at 410, 440, 490, 510 and 550 nm were used as inputs for IOP retrieval.

8.2 Results and Discussion with IOCCG Data Sets

8.2.1 Simulated data set

Over the large dynamic range of the data set the inversion fares rather well for both 10 and 20% criteria (Figure 8.1, Tables 8.1 and 8.2). Not surprisingly the stringent criteria provide less but better solutions (in terms of RMSE error and bias). The agreement between derived and known IOPs can be further improved

Table 8.1 RMSE and regression (Type II) results for the synthesized data set. Statistics of comparison of the median of all possible inversion solutions with a 10% agreement criterion. R_{rs} values at 410, 440, 490, 510 and 550 nm were used as inputs for IOP retrieval. N is the number of data tested, while n is the number of valid retrieval.

	N	n	intercept	slope	R^2	RMSE	bias
$a(440)$	500	408	-0.001	0.995	0.966	0.106	0.003
$b_{bp}(440)$	500	408	-0.055	0.972	0.935	0.125	0.003
$a_{dg}(440)$	500	408	-0.021	0.982	0.956	0.141	-0.001
$a_{ph}(440)$	500	408	0.160	1.113	0.927	0.159	-0.002

Table 8.2 RMSE and regression (Type II) results for the synthesized data set. Statistics of comparison of the median of all possible inversion solutions with a 20% agreement criterion. R_{rs} values at 410, 440, 490, 510 and 550 nm were used as inputs for IOP retrieval. N is the number of data tested, while n is the number of valid retrieval.

	N	n	intercept	slope	R^2	RMSE	bias
$a(440)$	500	438	-0.074	0.938	0.946	0.145	-0.025
$a_{ph}(440)$	500	438	-0.025	1.014	0.878	0.201	-0.044
$a_{dg}(440)$	500	438	-0.082	0.942	0.944	0.169	-0.023
$b_{bp}(440)$	500	438	-0.186	0.925	0.898	0.168	-0.034

by choosing other wavelengths (*e.g.* 410 nm for a_{dg} and 550 nm for b_{bp}) and by adding more wavelengths (*e.g.* Wang *et al.* (2005) added a 670 nm channel and the successful retrieval increased from 408 to 472 with the 10% criteria). It is encouraging that the uncertainty estimates for both $a_{dg}(440)$ and $b_{bp}(440)$ intersect the 1:1 line suggesting the constraint criteria is working well.

8.2.2 *In situ* data set

Large uncertainties in inverted parameters (in particular a_{ph}) suggest that some of these data have many possible solutions and thus large uncertainties for a given $R_{rs}(\lambda)$. Some data points are way off the line, possibly due to large sun angles and/or poor measurements (Figure 8.2 and Tables 8.3 and 8.4).

In Wang *et al.* (2005) we used a more complicated phytoplankton absorption formulation which increased the computation by a factor larger than 10. We found that this complexity did not improve the match ups significantly and thus decided here to use a single phytoplankton absorption function. It can easily be demonstrated that a different choice of wavelengths for inversions or a different choice of wavelength for the parameter can significantly improve/degrade the retrieval. Thus, if we are after a_{dg}, inverting a near UV wavelength provides the best inversion; while for b_b, it is in the NIR that the inversion does best; as long

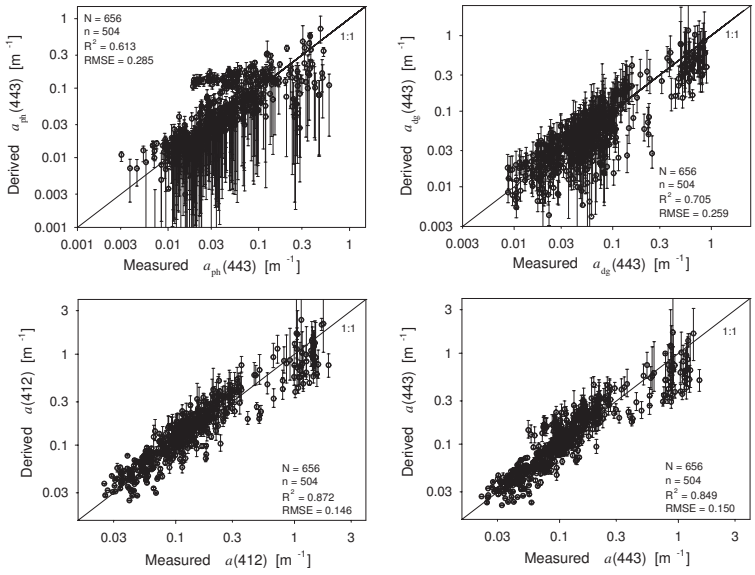

Figure 8.2 Comparison of inverted and the *in situ* data set (Sun at 30° from zenith) for $a_{\mathrm{ph}}(440)$, $a_{\mathrm{dg}}(440)$, $a(440)$, and $b_{\mathrm{bp}}(440)$ for the 10% criteria (statistics in Table 8.3). Vertical lines denote the 90% confidence intervals in the solutions. R_{rs} values at 410, 440, 490, 510 and 555 nm were used as inputs for IOP retrieval.

as adequate R_{rs} at those wavelengths could be available.

8.3 Summary

The inversion method presented here was designed to provide uncertainty estimates of inversion products and is dependent on the reality of the assumptions of the model. For example, it is well known that Equation 8.6 is likely not a good representation of particulate spectral backscattering, yet it is the only simple model currently available. Much work is still needed to understand spectral IOPs, and such work will, without a doubt, improve our ability to retrieve in-water parameters from remote sensing.

Table 8.3 RMSE and regression (Type II) results for the *in situ* data set. Statistics of comparison of the median of all possible inversion solutions with a 10% agreement criterion. R_{rs} values at 412, 443, 490, 510 and 555 nm were used as inputs for IOP retrieval. N is the number of data tested, while n is the number of valid retrievals.

	N	n	intercept	slope	R^2	RMSE	bias
$a(412)$	656	504	-0.022	0.942	0.872	0.146	0.029
$a(443)$	656	504	-0.029	0.969	0.849	0.150	0.001
$a_{dg}(443)$	656	504	-0.018	1.043	0.705	0.259	-0.072
$a_{ph}(443)$	656	504	0.068	1.031	0.613	0.285	0.024

Table 8.4 RMSE and regression (Type II) results for the *in situ* data set. Statistics of comparison of the median of all possible inversion solutions with a 20% agreement criterion. R_{rs} values at 412, 443, 490, 510 and 555 nm were used as inputs for IOP retrieval. N is the number of data tested, while n is the number of valid retrievals.

	N	n	intercept	slope	R^2	RMSE	bias
$a(412)$	656	629	-0.036	0.939	0.867	0.157	0.019
$a(443)$	656	629	-0.039	0.977	0.842	0.165	-0.017
$a_{dg}(443)$	656	629	0.086	1.069	0.63	0.298	-0.013
$a_{ph}(443)$	656	629	-0.057	1.014	0.714	0.266	-0.075

Chapter 9

MODIS Semi-Analytic Algorithm for IOP

Kendall Carder, Jennifer Cannizzaro, Robert Chen and ZhongPing Lee

9.1 Introduction

The Moderate-Resolution Imaging Spectrometer (MODIS) semi-analytic algorithm (Carder_MODIS here after) (Carder *et al.*, 1999; Carder *et al.*, 2004) derives chlorophyll-a concentrations and inherent optical properties ($a_{\mathrm{ph}}(\lambda)$, $a_{\mathrm{dg}}(\lambda)$ and $b_{\mathrm{bp}}(\lambda)$) from remote-sensing reflectance spectrum ($R_{\mathrm{rs}}(\lambda)$). This algorithm is composed with an algebraic portion and an empirical portion. The algebraic portion is for waters with low absorption (mostly oceanic waters) while the empirical portion is for waters with high absorption (mostly coastal waters). One of the main characteristics of this algorithm is that it responds to the large global variability observed in both chlorophyll-specific absorption coefficients ($a^*_{\mathrm{ph}}(\lambda)$), as well as gelbstoff-to-phytoplankton absorption ratios. This algorithm utilizes differences between measured sea-surface temperatures and known nitrate-depletion temperatures (NDT) (Kamykowski and Zentara, 1986; Kamykowski, 1987) to select the most appropriate $a^*_{\mathrm{ph}}(\lambda)$ for a given bio-optical domain. The algorithm was first developed and evaluated using high-light, tropical/subtropical and summer temperate field data (Carder *et al.*, 1999) and later expanded to include parameters appropriate for low-light, polar data (Carder *et al.*, 2004).

9.2 Algorithm Description

9.2.1 Remote-sensing reflectance model

By making several approximations, the $R_{\mathrm{rs}}(\lambda)$ used in Carder_MODIS algorithm is simplified to (Carder *et al.*, 1999)

$$R_{\mathrm{rs}}(\lambda) \approx \mathrm{constant}\frac{b_{\mathrm{b}}(\lambda)}{a(\lambda)}, \tag{9.1}$$

where the “constant" is unchanging with respect to wavelength and solar zenith angle. The value of the constant is not relevant to the algorithm since, as will

be shown later, the algorithm (for absorption and chlorophyll-a concentration) uses spectral ratios of $R_{rs}(\lambda)$ and the constant term factors out.

Further, both $b_b(\lambda)$ and $a(\lambda)$ are partitioned into several separate terms. Each term is described empirically and is written in a general fashion as a function of variables and empirically derived parameters. Since sea-surface temperatures were not provided in the IOCCG data sets, the unpackaged parameters regarding $a^*_{ph}(\lambda)$ derived from high-light, tropical/subtropical and summer temperate waters were employed (Carder *et al.*, 1999) (see Table 9.1). While $a^*_{ph}(\lambda)$ is extremely important for deriving chlorophyll-a concentrations accurately, retrievals of $a_{ph}(\lambda)$ and $a_{dg}(\lambda)$ are less sensitive to differences in $a^*_{ph}(\lambda)$.

Table 9.1 Parameters for the MODIS semi-analytical algorithm for regions without packaged pigments

λ	a_0	a_1	a_2	a_3	X_0	X_1	Y_0	Y_1	S (nm^{-1})
412	2.20	0.75							
443	3.59	0.80	0.5	0.0112	-0.00182	2.058	-1.13	2.57	0.0225
488	2.27	0.59							
551	0.42	-0.22							

9.2.2 Backscattering coefficients

The total backscattering coefficient, $b_b(\lambda)$, can be expanded as

$$b_b(\lambda) = b_{bw}(\lambda) + b_{bp}(\lambda), \tag{9.2}$$

with $b_{bp}(\lambda)$ modelled as (Carder *et al.*, 1999)

$$b_{bp}(\lambda) = X\left(\frac{551}{\lambda}\right)^Y. \tag{9.3}$$

$b_{bw}(\lambda)$ is constant (Morel, 1974). X is the particulate backscattering at 551 nm, and Y describes the spectral shape of the particle backscattering spectrum. Values for X and Y were determined empirically by model inversion (Carder *et al.*, 1999) and are described as

$$X = X_0 + X_1 R_{rs}(551), \tag{9.4}$$

$$Y = Y_0 + Y_1 \frac{R_{rs}(443)}{R_{rs}(488)}, \tag{9.5}$$

where $X_{0,1}$ and $Y_{0,1}$ are empirically derived constants (Carder *et al.*, 1999) and are provided in Table 9.1.

When absorption due to water molecules does not dominate the total absorption coefficient at 551 nm, algorithms that utilize wavelengths longer than

551 nm, that take advantage of the larger inflection in the pure water absorption spectra between 570-610 nm (Pope and Fry, 1997), are required. Using measurements of $R_{rs}(\lambda)$ and $b_{bp}(\lambda)$ collected from the West Florida Shelf, the equation

$$b_{bp}(551) = 10^{(0.933-0.134\log(R_{rs}(551))+1.029\log(R_{rs}(667)))} - 0.000966, \quad (9.6)$$

(n=154, $r^2 = 0.96$, RMSE = 0.160) was derived for MODIS-like wavelengths. This function was used when the Carder_MODIS algorithm was applied to the IOCCG synthetic data set. Since remote-sensing data with wavelengths longer than 555 nm were not available for the IOCCG *in situ* data set, however, $b_{bp}(551)$ values were then estimated using Equation 9.4.

9.2.3 Absorption coefficients

The total absorption coefficient, $a(\lambda)$, can be expanded as

$$a(\lambda) = a_w(\lambda) + a_{ph}(\lambda) + a_{dg}(\lambda), \quad (9.7)$$

with values of $a_w(\lambda)$ taken from Pope and Fry (1997).

The shape of the $a_{ph}(\lambda)$ spectrum for a given water mass changes due to the pigment-package effect and changes in pigment composition. For the MODIS wavebands centered at 412, 443, 488, and 551 nm, a hyperbolic tangent function was chosen to empirically model the ratio of $a_{ph}(\lambda)/a_{ph}(675)$ in order to ensure that this ratio approaches an asymptote at very high or very low values of $a_{ph}(675)$ (Carder *et al.*, 1999),

$$a_{ph}(\lambda) = a_0(\lambda)\exp\left(a_1(\lambda)\tanh\left(a_2(\lambda)\ln\left(a_{ph}(675)/a_3(\lambda)\right)\right)\right)a_{ph}(675), \quad (9.8)$$

with values of $a_{0-3}(\lambda)$ provided in Table 9.1.

The cumulative effects of detritus and gelbstoff absorption, $a_{dg}(\lambda)$, are expressed as

$$a_{dg}(\lambda) = a_{dg}(400)\exp(-S(\lambda - 400)), \quad (9.9)$$

where S is the spectral slope, and a value of 0.0225 nm^{-1} provided optimal retrieval results for the Carder_MODIS algorithm to calculate chlorophyll-a concentrations (Carder *et al.*, 1999). It is larger than the mean ocean value of about 0.015 nm^{-1}, likely compensating in part for uncertainties in other parts of the model.

9.2.4 Model inversion

Via Equations 9.1 – 9.9, $R_{rs}(\lambda)$ is reduced to a function of three unknowns ("constant" term, $a_{ph}(675)$, and $a_{dg}(400)$) along with model constants for $X_{0,1}$, $Y_{0,1}$, $a_{0-3}(\lambda)$, and S (Table 9.1). To algebraically solve for the values of the two desired

unknowns ($a_{\mathrm{ph}}(675)$ and $a_{\mathrm{dg}}(400)$), spectral ratios of 412/443 and 443/551 for $R_{\mathrm{rs}}(\lambda)$ as shown

$$\begin{aligned} \frac{R_{\mathrm{rs}}(412)}{R_{\mathrm{rs}}(443)} &= \frac{b_{\mathrm{b}}(412)}{b_{\mathrm{b}}(443)} \frac{a(443)}{a(412)}, \\ \frac{R_{\mathrm{rs}}(443)}{R_{\mathrm{rs}}(551)} &= \frac{b_{\mathrm{b}}(443)}{b_{\mathrm{b}}(551)} \frac{a(551)}{a(443)}, \end{aligned} \tag{9.10}$$

provided the best separation of the two absorption contributions. Details on the computational method of solving these equations are discussed in Carder *et al.* (1999).

9.2.5 Empirical portion of Carder_MODIS

For waters with high concentrations of gelbstoff and chlorophyll, $R_{\mathrm{rs}}(412)$ and $R_{\mathrm{rs}}(443)$ values are small, and therefore the above semi-analytical approach cannot perform properly due to low signal-to-noise ratios. Thus the semi-analytic approach is designed to return values only when modelled $a_{\mathrm{ph}}(675)$ values are less than 0.025 m^{-1}, which is equivalent to a chlorophyll-a concentration of about 1.5 mg m^{-3}. Otherwise, the following empirical algorithms derived from the West Florida Shelf (1999-2001) and Bayboro Harbor (St. Petersburg, Florida) field data (n = 319) are used.

For $a_{\mathrm{ph}}(443)$, there is

$$a_{\mathrm{ph}}(443)_{\mathrm{emp}} = 10^{(-1.164-1.2095\rho_{35}-1.566\rho_{35}^2-1.708\rho_{45}+19.502\rho_{45}^2)}, \tag{9.11}$$

where ρ_{ij} is the log-transformed ratio of $R_{\mathrm{rs}}(\lambda_i)$ to $R_{\mathrm{rs}}(\lambda_j)$ and the subscripts i and j are wavebands #1-6 that represent MODIS wavebands 412, 443, 488, 531, 551, and 667 nm, respectively. Since this equation requires the MODIS $R_{\mathrm{rs}}(531)$ waveband and the SeaWiFS waveband $R_{\mathrm{rs}}(510)$ was provided instead with the IOCCG *in situ* data, a modified SeaWiFS algorithm was also developed

$$a_{\mathrm{ph}}(443)_{\mathrm{emp}} = 10^{(-1.189-1.33\rho_{35}-2.151\rho_{35}^2-0.775\rho_{45S}+7.592\rho_{45S}^2)}, \tag{9.12}$$

and applied to the IOCCG *in situ* data set. Here ρ_{45S} is equal to $\log(R_{\mathrm{rs}}(510)/R_{\mathrm{rs}}(555))$.

The empirical algorithm for $a_{\mathrm{dg}}(443)$ is

$$a_{\mathrm{dg}}(443)_{\mathrm{emp}} = 10^{(-1.144-0.738\rho_{15}-1.386\rho_{15}^2-0.644\rho_{25}+2.451\rho_{25}^2)}, \tag{9.13}$$

and was applied to the IOCCG *in situ* data set. Since adding a ρ_{65} term reduced the RMSE error by 40% for calculating $a_{\mathrm{dg}}(443)$ for the West Florida Shelf and Bayboro Harbor data, the derived equation

$$a_{\mathrm{dg}}(443)_{\mathrm{emp}} = 10^{(0.043-0.185\rho_{25}-1.081\rho_{35}+1.234\rho_{65})}, \tag{9.14}$$

was applied to the synthetic data set where $R_{rs}(670)$ data (considered equal to $R_{rs}(667)$) were available.

Empirical retrievals of $a(\lambda)$ at 412, 443, and 488 nm also improved for the West Florida Shelf and Bayboro Harbor data set when a red reflectance waveband was included. Thus, the empirical expression derived from field data and applied to the synthetic data set takes the form

$$a(\lambda)_{emp} = 10^{(c_0(\lambda)+c_1(\lambda)\log(R_{rs}(443))+c_2(\lambda)\log(R_{rs}(488))+c_3(\lambda)\log(R_{rs}(667)))}, \quad (9.15)$$

where $c_{0-3}(\lambda)$ are empirically derived parameters (Table 9.2a). Note that while reflectance ratios are used to calculate $a_{ph}(443)_{emp}$ and $a_{dg}(443)_{emp}$, reflectance values are used to calculate $a(\lambda)_{emp}$ in Equation 9.15. For the IOCCG *in situ* data set that does not have a red reflectance waveband, an empirical expression similar to that of Lee *et al.* (1998b)

$$a(\lambda)_{emp} = 10^{(t_0(\lambda)+t_1(\lambda)\rho_{25}+t_2(\lambda)\rho_{25}^2+t_3(\lambda)\rho_{35}+t_4(\lambda)\rho_{35}^2)}, \quad (9.16)$$

was developed with $t_{0-4}(\lambda)$ (Table 9.2b) also derived from the West Florida Shelf and Bayboro Harbor data.

Table 9.2a Wavelength-dependent parameters for the high-absorption empirical $a(\lambda)$ algorithm (Equation 9.15) that requires $R_{rs}(670)$.

	$c_0(\lambda)$	$c_1(\lambda)$	$c_2(\lambda)$	$c_3(\lambda)$
$a(412)$	-0.349	-1.041	0.171	0.754
$a(443)$	-0.166	0.068	-1.284	1.077
$a(488)$	-0.167	0.478	-1.639	1.075

Table 9.2b Wavelength-dependent parameters for the high-absorption empirical $a(\lambda)$ algorithm (Equation 9.16) that does not require $R_{rs}(670)$.

	$t_0(\lambda)$	$t_1(\lambda)$	$t_2(\lambda)$	$t_3(\lambda)$	$t_4(\lambda)$
$a(412)$	-0.640	-0.718	-0.650	-1.365	2.369
$a(443)$	-0.837	-0.860	-0.791	-1.162	2.855
$a(488)$	-0.947	-0.343	-0.721	-1.633	2.741

9.2.6 Blending semi-analytic and empirical IOP values

In order to provide a smooth transition in modelled IOP values when the algorithm switches from the semi-analytical to the empirical method, a weighted average of the modelled values returned by both algorithms is used near the transition border (Carder *et al.*, 1999). When the semi-analytical portion returns an $a_{ph}(675)$ value between 0.015 and 0.025 m^{-1}, IOP values are calculated as

$$IOP = w(IOP)_{sa} + (1 - w)(IOP)_{emp}, \quad (9.17)$$

where $(\text{IOP})_{\text{sa}}$ is the semi-analytically-derived value, $(\text{IOP})_{\text{emp}}$ is the empirically derived value, and w is the weighting factor equal to $(0.025 - a_{\text{ph}}(675))/0.010$. Semi-analytical and empirical IOP values are used when modelled $a_{\text{ph}}(675)$ values are less than 0.015 m^{-1} and greater than 0.025 m^{-1}, respectively. Note that this transition range can vary with pigment packaging (*e.g.*, see Carder *et al.*, 2004).

9.3 Algorithm Performance with the IOCCG Data Sets

The Carder_MODIS algorithm requires $R_{\text{rs}}(\lambda)$ data at a minimum of five wavebands: 412, 443, 488, 531 and 551 nm. Further inclusion of the $R_{\text{rs}}(667)$ improves retrievals of $a_{\text{dg}}(443)_{\text{emp}}$ (Equation 9.14) and $a(\lambda)_{\text{emp}}$ (Equation 9.15) values. Since the synthetic $R_{\text{rs}}(\lambda)$ data was generated in 10 nm increments from 400–800 nm, reflectance values at 410, 440, 490, 530, 550 and 670 nm were considered similar enough to the MODIS wavebands and were input into the algorithm. For the IOCCG *in situ* data set only $R_{\text{rs}}(\lambda)$ data at 412, 443, 490, 510, and 555 nm were input into the equations.

9.3.1 Synthetic data set

Using the Carder_MODIS algorithm, the inherent optical properties $a(410)$, $a(440)$, $a(490)$, $a_{\text{ph}}(440)$, $a_{\text{dg}}(440)$ and $b_{\text{bp}}(550)$ were derived from the synthetic $R_{\text{rs}}(\lambda)$ data (Figure 9.1). Statistical analyses were performed on log-transformed data and include the slope, intercept, correlation of determination (R^2) and the root-mean-square error (RMSE) (Table 9.3).

Table 9.3 RMSE and regression (Type II) results of the synthetic data set ($\theta_0 = 30°$). $R_{\text{rs}}(\lambda)$ values at 410, 440, 490, 530, 550 and 670 nm were used as inputs. N is the number of data tested, while n is the number of valid retrievals.

	N	n	intercept	slope	R^2	RMSE	bias
$a(410)$	500	500	0.015	0.990	0.990	0.071	0.020
$a(440)$	500	500	0.030	1.030	0.993	0.059	0.010
$a(490)$	500	500	0.079	1.082	0.993	0.065	0.008
$b_{\text{bp}}(550)$	500	500	-0.012	0.998	0.995	0.042	-0.008
$a_{\text{ph}}(440)$	500	500	-0.046	0.908	0.963	0.141	0.071
$a_{\text{dg}}(440)$	500	500	0.084	1.098	0.978	0.135	-0.004

Particulate backscattering coefficients at 550 nm retrieved using Equation 9.6 from $R_{\text{rs}}(550)$ and $R_{\text{rs}}(670)$ are very accurate (RMSE = 0.042). Total absorption coefficients at 410, 440 and 490 nm were also retrieved accurately for the synthetic data set with RMSE errors equal to 0.071, 0.059 and 0.065, re-

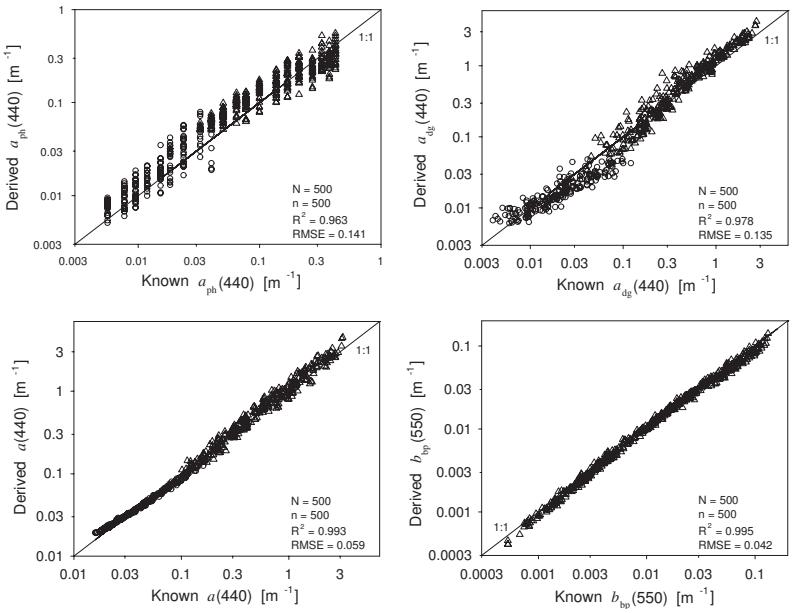

Figure 9.1 Relationships between known and retrieved IOPs using the Carder–MODIS algorithm (synthetic data set with Sun at 30° from zenith), with $R_{rs}(\lambda)$ at 410, 440, 490, 530, 550 and 670 nm used as inputs. Symbols: semi-analytic (o) and empirical (Δ).

spectively. RMSE values for $a_{ph}(440)$ (0.141) and $a_{dg}(440)$ (0.135) are slightly more than double the error calculated for $a(440)$ since phytoplankton and detritus/gelbstoff exhibit overlapping absorption spectra making it difficult to separate them.

9.3.2 *In situ* data set

The results of the Carder_MODIS algorithm when applied to the IOCCG *in situ* data set were not as good as the results observed for the synthetic data set because errors in field R_{rs} and IOP data, not present in the synthetic data, are significant in the *in situ* data.

Total absorption coefficients at 412, 443, and 488 nm derived from the in situ $R_{rs}(\lambda)$ yielded RMSE errors of 0.197, 0.205 and 0.206, respectively (Figure 9.2, Table 9.4). Errors for $a_{ph}(443)$ and $a_{dg}(443)$ were only slightly higher than $a(443)$ and were 0.195 and 0.279, respectively. While the semi-analytic $a_{ph}(443)$ values derived from synthetic $R_{rs}(\lambda)$ data were overestimated, values derived from the *in situ* $R_{rs}(\lambda)$ data were more centered about the one-to-one line. This may indicate that perhaps the underlying $a_{ph}(\lambda)$ functions used to generate the synthetic data for oligotrophic waters are not quite representative of the distribution of the naturally occurring $a_{ph}(\lambda)$ data, or at least Equation 9.8 is more consistent with the $a_{ph}(\lambda)$ functionality of the *in situ* data set than with that of the synthetic data set.

Table 9.4 RMSE and regression (Type II) results of the *in situ* data set. $R_{rs}(\lambda)$ values at 412, 443, 490, 510 and 555 were used as inputs. N is the number of data tested, while n is the number of valid retrievals.

	N	n	intercept	slope	R^2	RMSE	bias
$a(412)$	656	656	0.098	1.066	0.826	0.197	0.039
$a(443)$	656	656	0.030	1.111	0.831	0.205	-0.078
$a(488)$	656	656	0.131	1.173	0.789	0.206	-0.063
aph(443)	656	656	-0.052	0.986	0.827	0.195	-0.032
adg(443)	656	656	-0.041	1.082	0.771	0.279	-0.144

Large errors that occur in empirically derived $a(412)$, $a(443)$, and $a_{ph}(443)$ values and that appear as linear horizontal rows of data in Figure 9.2 at ~0.23, 0.15, and 0.07 m^{-1}, respectively, can be traced to a single investigator for a large multi-year, coastal data set. Removal of these points would improve the performance of the empirical portion of our algorithm. Furthermore, empirical retrievals of $a(\lambda)$ and $a_{dg}(440)$ may also be improved for this data set if $R_{rs}(\lambda)$ data were available for wavelengths longer than 555 nm.

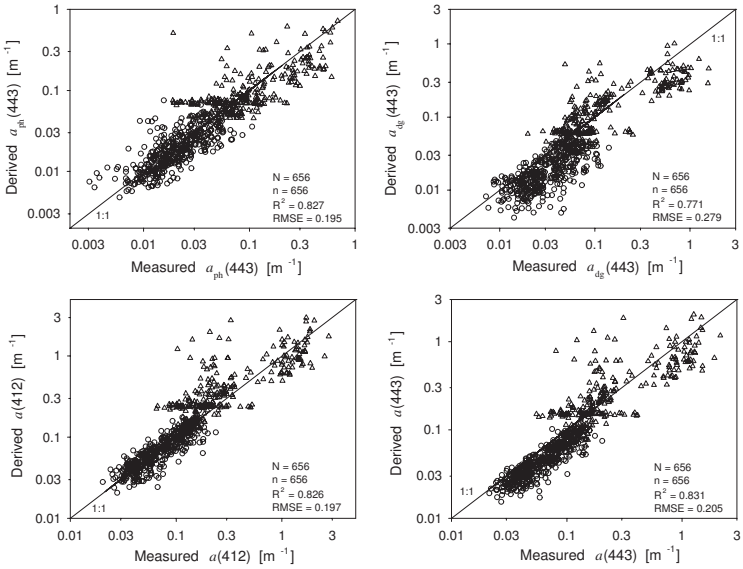

Figure 9.2 Relationships between measured and retrieved IOPs using the Carder_MODIS algorithm (*in situ* data set), with $R_{rs}(\lambda)$ at 412, 443, 490, 510 and 555 nm used as inputs. Symbols: semi-analytic (o) and empirical (Δ).

9.4 Conclusions

The Carder_MODIS algorithm (Carder *et al.*, 1999) calculated $b_{bp}(550)$ and $a(\lambda)$ values very accurately for the synthetic data set. Values for $a_{ph}(443)$ and $a_{dg}(443)$ were calculated less accurately because phytoplankton and detritus/gelbstoff exhibit overlapping absorption making it more difficult to separate them using $R_{rs}(\lambda)$. Retrieval errors tripled for $a(\lambda)$ and doubled for $a_{dg}(443)$ when the algorithm was applied to the *in situ* data set as compared to the synthetic data set. The fact that the partitioned values fell within the same error range as the total-absorption values suggests that much of the error imputed to the algorithms for the *in situ* data set may be attributable to errors or inconsistencies among the measured data sets, whereas the synthetic data set had no measurement noise.

IOP retrieval errors calculated for the *in situ* data set may improve if $R_{rs}(667)$ data were available. Significant error reductions were observed for empirically derived backscattering and total absorption coefficients when red reflectance data were used for our high-absorption Florida data set and for the synthetic data set. Note, however, that while $R_{rs}(667)$ can be used for "perfect" synthetic data, accurate measurements of $R_{rs}(667)$ from space are much more subject to error due to smaller signal-to-noise ratios. A waveband near 610–620 nm would perhaps be a better compromise than the use of 667 nm for satellites. The

Medium Resolution Imaging Spectrometer (MERIS) has such a waveband around 620 nm.

Finally, the expansion of available global data sets in the past 10 years and the broad range of data synthesized in the numerical data set have provided examples of how various older algorithms may be improved, and we are grateful for being included in this challenging algorithm inter-comparison.

Chapter 10

The Quasi-Analytical Algorithm

ZhongPing Lee, Kendall Carder and Robert Arnone

10.1 General Description

The Quasi-Analytical Algorithm (QAA) was developed by Lee *et al.* (2002) to derive inherent optical properties of optically deep waters. QAA separates the inversion process into two consecutive sections. The first section is the derivation of coefficients of total absorption and backscattering. In this section, there is no involvement of spectral models for the absorption coefficient of phytoplankton pigments and gelbstoff. The second section, which utilizes the derived total absorption coefficient from the first section, decomposes the total absorption coefficient into its major components.

10.2 Derive Total Absorption and Backscattering Coefficients

In this part, QAA follows the generally accepted relationship between remote-sensing reflectance and $b_b/(a + b_b)$, and the fact that water absorption coefficients dominate most of the longer wavelengths. Here b_b is the total backscattering coefficient and a is the total absorption coefficient. QAA starts with the calculation of a at a reference wavelength (λ_0, 555 or 640 nm), with the assumption that remote-sensing reflectance at this wavelength is well measured from a remote-sensing platform.

The total absorption coefficient at λ_0 is expressed as

$$a(\lambda_0) = a_w(\lambda_0) + \Delta a(\lambda_0), \tag{10.1}$$

where $a_w(\lambda_0)$ is the contribution from water molecules (Pope and Fry, 1997), and $\Delta a(\lambda_0)$ represents the contribution from dissolved and suspended constituents. For this $a(\lambda_0)$, errors in its estimation are limited as long as $a_w(\lambda_0)$ makes up a big portion (at least one third of the total).

Lee *et al.* (2002) proposed two λ_0 for dealing with IOP inversion: 555 nm for oceanic and most coastal waters and 640 nm for waters with high absorption

coefficients ($a(440) >\sim 0.5$ m^{-1}). For each λ_0, there could be many ways to estimate $a(\lambda_0)$. In the exercise reported here, when 555 nm is selected as λ_0, $a(555)$ is estimated using the Morel-Maritorena approach (Morel and Maritorena, 2001) as described in Chapter 4. That is, $K_d(555)$ is estimated first with $\rho = \log(\max(R_{rs}(440, 490, 510))/R_{rs}(555))$,

$$K_d(555) = 0.0605 + 10^{-1.163-1.969\rho+1.239\rho^2+0.417\rho^3-0.984\rho^4}, \tag{10.2}$$

and then

$$a(555) = \frac{0.9K_d(555)(1 - 6.8R_{rs}(555))}{1 + 15.3R_{rs}(555)}. \tag{10.3}$$

For sensors such as MODIS where no 510 nm band exists, a slight adjustment regarding Equation 10.2 is sufficient for the implementation of QAA.

When 640 nm is selected as λ_0, $a(640)$ is estimated as in Lee *et al.* (2002), *i.e.*,

$$a(640) = 0.31 + 0.07\left(\frac{r_{rs}(640)}{r_{rs}(440)}\right)^{1.1}, \tag{10.4}$$

where r_{rs} is the subsurface remote-sensing reflectance corresponding to the R_{rs} measured above the surface.

To estimate $a(640)$ requires measurements of remote-sensing reflectance at 640 nm, a band which does not exist in many satellite sensors (such as SeaWiFS). To overcome this limitation, $R_{rs}(640)$ is simulated with measurements made at 490, 555 and 670 nm, as described in Lee *et al.* (2005b),

$$R_{rs}(640) = 0.01R_{rs}(555) + 1.4R_{rs}(670) - 0.0005R_{rs}(670)/R_{rs}(490). \tag{10.5}$$

Note that in Lee *et al.* (2005b) it is $R_{rs}(667)$ for SeaWiFS spectral bands. This empirical formula was aimed to more or less correct the chlorophyll-a fluorescence contained in $R_{rs}(670)$.

$r_{rs}(\lambda)$ is calculated from $R_{rs}(\lambda)$ through

$$r_{rs}(\lambda) = R_{rs}(\lambda)/(0.52 + 1.7R_{rs}(\lambda)), \tag{10.6}$$

where 0.52 and 1.7 are empirical values derived from data simulated by Hydrolight (Lee *et al.*, 1999). Because $r_{rs}(\lambda)$ can be modelled as a polynomial function of $b_b/(a + b_b)$ (Gordon *et al.*, 1988; Lee *et al.*, 1998a), $b_b/(a + b_b)$ (represented as symbol u) at λ can be calculated algebraically from $r_{rs}(\lambda)$ (Hoge and Lyon, 1996; Lee *et al.*, 2002),

$$u(\lambda) \equiv \frac{b_b(\lambda)}{a(\lambda) + b_b(\lambda)} = \frac{-0.0895 + \sqrt{0.008 + 0.499r_{rs}(\lambda)}}{0.249}. \tag{10.7}$$

The spectral $b_b(\lambda)$ is modelled with the widely used expression (Smith and Baker, 1981; Gordon and Morel, 1983),

$$b_b(\lambda) = b_{bw}(\lambda) + b_{bp}(\lambda_0)\left(\frac{\lambda_0}{\lambda}\right)^Y, \tag{10.8}$$

where b_{bw} and b_{bp} are the backscattering coefficients of pure seawater and suspended particles, respectively. Values of $b_{bw}(\lambda)$ are provided in Morel (1974).

When $a(\lambda_0)$, $u(\lambda_0)$, and $b_{bw}(\lambda_0)$ are known, $b_{bp}(\lambda_0)$ in Equation 10.8 can be easily derived. The values of $b_b(\lambda)$ at other wavelengths are then calculated when the wavelength exponent (Y) is estimated from Lee *et al.* (2002)

$$Y = 2.2\left(1 - 1.2\exp\left(-0.9\frac{r_{rs}(440)}{r_{rs}(555)}\right)\right). \tag{10.9}$$

Finally, applying $b_b(\lambda)$ back to $u(\lambda)$ (derived from $r_{rs}(\lambda)$, Equation 10.7), the total absorption coefficient at wavelength λ, $a(\lambda)$, is calculated algebraically,

$$a(\lambda) = \frac{(1 - u(\lambda))b_b(\lambda)}{u(\lambda)}. \tag{10.10}$$

To obtain smooth satellite IOP products where both 555 nm and 640 nm could be used as reference wavelengths, the final $a(\lambda)$ product is a combination of the absorption coefficients derived using 555 nm as reference wavelength ($a(\lambda)^{[555]}$) and 640 nm as reference wavelength ($a(\lambda)^{[640]}$), as follows:

$$\begin{cases} a(\lambda) = a(\lambda)^{[555]}, & \text{for } a(440)^{[555]} < 0.3, \\ a(\lambda) = \left(1 - \frac{a(440)^{[555]} - 0.3}{0.2}\right) a(\lambda)^{[555]} + & \\ \qquad \left(\frac{a(440)^{[555]} - 0.3}{0.2}\right) a(\lambda)^{[640]}, & \text{for } 0.3 \le a(440)^{[555]} \le 0.5, \\ a(\lambda) = a(\lambda)^{[640]}, & \text{for } a(440)^{[555]} > 0.5. \end{cases} \tag{10.11}$$

Further, final $b_{bp}(\lambda)$ is recalculated using $u(\lambda)$ and $a(\lambda)$ based on Equations 10.7 and 10.8.

10.3 Decomposition of the Total Absorption Coefficient

Decomposition of $a(\lambda)$ used the $a(410)$ and $a(440)$ values derived from the above steps. In the process, two more parameters are estimated first. One is the spectral ratio of $a_{ph}(410)/a_{ph}(440)$ (represented by symbol ζ), while the other is the spectral ratio of $a_{dg}(410)/a_{dg}(440)$ (represented by symbol ξ). The value of ζ is estimated using the spectral ratio of $r_{rs}(440)/r_{rs}(555)$ based on the field data (Lee *et al.*, 1998b):

$$\zeta = a_{ph}(410)/a_{ph}(440) = 0.71 + \frac{0.06}{0.8 + r_{rs}(440)/r_{rs}(555)}. \tag{10.12}$$

The value of ξ is calculated after the spectral slope S (used to describe the spectral shape of $a_{dg}(\lambda)$) is selected (0.015 nm^{-1} is used in this exercise):

$$\xi = a_{dg}(410)/a_{dg}(440) = \exp(S(440 - 410)). \tag{10.13}$$

When the values of $a(410)$, $a(440)$, ζ and ξ are known, $a_{ph}(440)$ and $a_{dg}(440)$ are calculated algebraically,

$$\begin{cases} a_{dg}(440) = \frac{(a(410)-\zeta a(440))}{\xi-\zeta} - \frac{(a_w(410)-\zeta a_w(440))}{\xi-\zeta}, \\ a_{ph}(440) = a(440) - a_{dg}(440) - a_w(440). \end{cases} \tag{10.14}$$

10.4 Results and Discussion

The above steps to retrieve IOPs from $R_{rs}(\lambda)$ are applied to the IOCCG data sets. For the synthetic data set, R_{rs} values at 410, 440, 490, 510, 555, and 670 nm were used as indicated ($R_{rs}(555)$ is a simple average of $R_{rs}(550)$ and $R_{rs}(560)$). For the *in situ* data set, however, only R_{rs} values at the first five wavelengths were used as $R_{rs}(670)$ is not available. The retrieved IOPs include $a(\lambda)$, $b_{bp}(\lambda)$, $a_{ph}(\lambda)$, and $a_{dg}(\lambda)$ of those wavelengths. To provide a general idea of the algorithm performance, some retrieved properties were compared with known values. Analysis results are presented in Tables 10.1 and 10.2 and the figures that follow. Performance (not presented) for the synthetic data with the Sun at 60° from zenith is similar to that with the Sun at 30°.

Table 10.1 RMSE and regression (Type II) results of the synthetic data set ($\theta_0 = 30°$). IOPs were retrieved with R_{rs} values at 410, 440, 490, 510, 555 and 670 nm. N is the number of data tested, while n is the number of valid retrievals.

	N	n	intercept	slope	R^2	RMSE	bias
$a(410)$	500	500	-0.001	0.971	0.993	0.061	0.016
$a(440)$	500	500	-0.004	0.971	0.992	0.060	0.016
$a(490)$	500	500	-0.041	0.959	0.989	0.062	-0.005
$b_{bp}(440)$	500	500	-0.099	0.945	0.981	0.081	0.008
$b_{bp}(555)$	500	500	-0.063	0.983	0.986	0.079	-0.029
$a_{dg}(410)$	500	476	-0.010	0.961	0.991	0.076	0.019
$a_{dg}(440)$	500	476	-0.032	0.960	0.985	0.093	0.006
$a_{ph}(440)$	500	476	0.044	1.008	0.930	0.160	0.033
$a_{ph}(490)$	500	476	0.013	1.010	0.825	0.257	-0.002

For the synthetic data set, total absorption and backscattering coefficients are accurately retrieved over the entire data range using the QAA algorithm (slope and R^2 values are near 1.0 and RMSE values are 0.06 - 0.08). The performance of the QAA for the *in situ* data set is not as good as that of the synthetic data set (see Figure 10.2 and Table 10.2), which is not surprising considering the unavoidable errors and uncertainties (see Chapter 3) in the measurement of both $R_{rs}(\lambda)$ and IOPs. The natural water environment is also far more complex than that simulated with computer code. Nevertheless, for such an inclusive data set, the RMSE values for $a(\lambda)$ are ~0.17.

Table 10.2 RMSE and regression (Type II) results of the *in situ* data set. IOPs were retrieved with R_{rs} values at 412, 443, 490, 510 and 555 nm. N is the number of data tested, while n is the number of valid retrievals.

	N	n	intercept	slope	R^2	RMSE	bias
$a(412)$	656	656	-0.089	0.963	0.868	0.168	-0.055
$a(443)$	656	656	-0.081	0.969	0.840	0.175	-0.051
$a(490)$	656	656	0.001	1.020	0.792	0.174	-0.021
$a_{dg}(412)$	656	630	-0.092	0.986	0.820	0.209	-0.077
$a_{dg}(443)$	656	630	-0.087	0.989	0.794	0.221	-0.072
$a_{ph}(443)$	656	630	0.033	1.067	0.593	0.321	-0.062
$a_{ph}(490)$	656	630	0.498	1.310	0.686	0.334	-0.007

For both synthetic and *in situ* data sets, the retrieval of $a_{dg}(\lambda)$ is only slightly worse than the retrieval of total absorption coefficients, but more errors are found in the derived $a_{ph}(\lambda)$ (see Tables 10.1 and 10.2 and Figures 10.1 and 10.2). This is, in part, because gelbstoff (including detritus) likely contributes more to the total absorption coefficient at 410 and/or 440 nm.

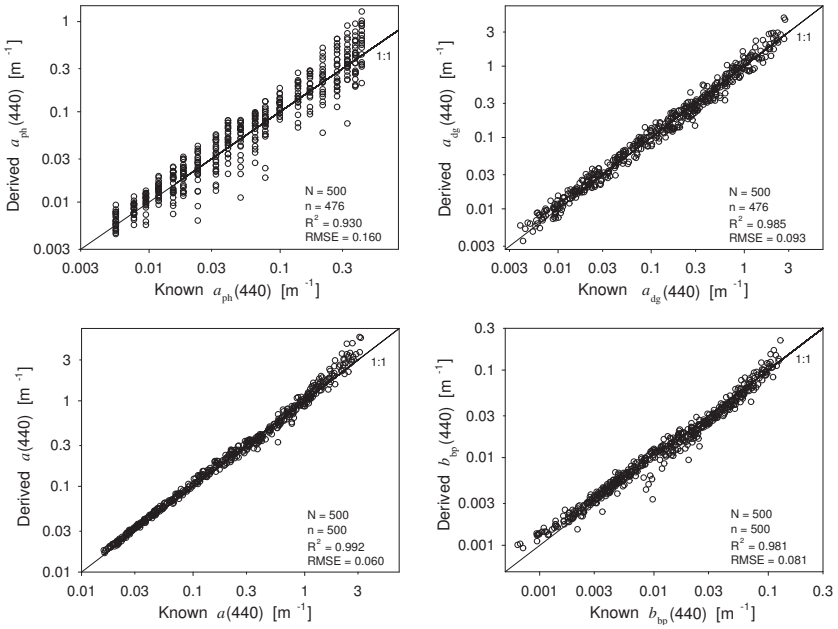

Figure 10.1 Comparison between QAA-derived IOPs and known IOPs, for the synthetic data set (sun at 30° from zenith). IOPs were derived with R_{rs} values at 410, 440, 490, 510, 555 and 670 nm as inputs (see text for details).

Also, in the explicit decomposition of total $a(\lambda)$ to $a_{ph}(\lambda)$ and $a_{dg}(\lambda)$, values of ζ and ξ are not known precisely, but have to be estimated. Errors in these estimations will be propagated to the derived values of $a_{dg}(440)$ and $a_{ph}(440)$.

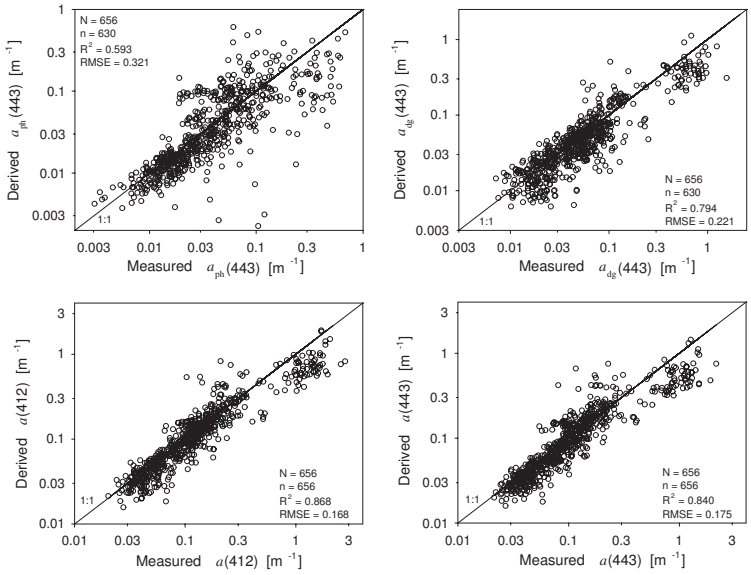

Figure 10.2 Comparison between QAA-derived IOPs and known IOPs, for the *in situ* data set. IOPs were retrieved with R_{rs} values at 412, 443, 490, 510 and 555 nm as inputs.

Note that the value of ξ (directly related to the spectral slope of $a_{dg}(\lambda)$), as observed in the field and represented in the synthetic data set, varies widely based on the nature of waters under study (*e.g.* humic versus fulvic acids, Carder *et al.*, 1989), abundance of detritus (Roesler *et al.*, 1989), but the present version of QAA uses a fixed spectral slope for all cases. Also, QAA currently uses only one spectral constraint regarding $a_{ph}(\lambda)$ (ratio of $a_{ph}(410)/a_{ph}(440)$) in the process of decomposing $a(\lambda)$. Due to errors in $R_{rs}(\lambda)$ measurements as well as errors in the selection of parameter S, negative $a_{ph}(440)$ or $a_{ph}(490)$ values appeared (4.8% in synthetic data and 4.0% in the *in situ* data). Such retrievals were then flagged and removed in the statistical analyses. This kind of obvious error can be remedied by replacing with empirical estimates (Lee *et al.*, 1998b), or by adding more spectral constraints in the derivation of $a_{ph}(\lambda)$ (*e.g.*, the full spectral models of $a_{ph}(\lambda)$ used in other algorithms), although this will introduce model uncertainties.

When $R_{rs}(640)$ was not used in the derivation process (*i.e.* 555 nm alone as reference wavelength), the performance of QAA with the synthetic data set was slightly degraded. For instance, the slope and R^2 values for $a(440)$ changed from 0.971 and 0.992 to 0.907 and 0.978, respectively, and RMSE changed from 0.06 to 0.109. The slope and R^2 values for $a_{dg}(440)$ (and $a_{ph}(440)$) became 0.905 and 0.969 (0.927 and 0.925, n = 477), respectively. As pointed out in Lee *et al.* (2002), the degradation happened to waters with large $a(440)$ (and

then $a(555)$) values (mostly turbid coastal waters) where $a_w(555)$ makes up less than $1/3$ of the total absorption coefficient. For such cases, there will be greater errors in the estimated $a(555)$ and subsequently in other IOPs. If it is limited to waters with $a(440) < 0.5$ m^{-1} (where $a_w(555)$ makes up at least $\sim 1/3$ of $a(555)$), however, the performance of QAA with 555 nm as λ_0 is significantly better. The slope and R^2 values are close to unity (n = 334) and RMSE values are ~ 0.05 for both total absorption and backscattering coefficients; and the RMSE are 0.09 and 0.15 for $a_{dg}(440)$ and $a_{ph}(440)$, respectively. These results demonstrate the importance of having a red band in the vicinity of 620–640 nm for remote sensing of coastal waters and the applicability of QAA to satellite data, especially for oceanic waters.

10.5 Conclusions

The QAA is an algorithm based on the fundamental relationships of ocean optics, and generally follows the inversion concept described in Chapter 1. When applying QAA to the IOCCG data sets (both synthetic and *in situ*), the retrieved IOPs matched known or measured IOPs very well (in particular, absorption coefficient of CDOM and the total, and particle backscattering coefficient). As is the case for many other inversion algorithms, QAA is mathematically simple and physically transparent. These characteristics make the algorithm easily adaptable to various multi-spectral or hyperspectral sensors, and it is also computationally efficient for processing satellite imagery.

Chapter 11

The GSM Semi-Analytical Bio-Optical Model

Stéphane Maritorena and Dave Siegel

11.1 General Description

The GSM (for Garver-Siegel-Maritorena) semi-analytical ocean colour model was initially developed by Garver and Siegel (1997) and later updated by Maritorena *et al.* (2002). The GSM model is based on the quadratic relationship between the remote-sensing reflectance (R_{rs}) and the absorption and backscattering coefficients from Gordon *et al.* (1988),

$$R_{rs}(\lambda) = \frac{t^2}{n_w^2} \sum_{i=1}^{2} g_i \left(\frac{b_b(\lambda)}{b_b(\lambda) + a(\lambda)} \right)^i, \tag{11.1}$$

where $g_1 (= 0.0949)$ and $g_2 (= 0.0794)$ are geometrical factors. The absorption coefficient ($a(\lambda)$) is decomposed into seawater absorption, $a_w(\lambda)$, phytoplankton absorption, $a_{ph}(\lambda)$, and the combined absorption of coloured detrital and dissolved material (CDM), $a_{dg}(\lambda)$ (considered together as a single term because of their similar spectral shapes (Carder *et al.*, 1991; Nelson *et al.*, 1998; Nelson and Siegel, 2002). The backscattering coefficient ($b_b(\lambda)$) is partitioned into terms due to seawater, $b_{bw}(\lambda)$, and suspended particulates, $b_{bp}(\lambda)$. The non-water absorption and scattering terms are parameterized as a known shape with an unknown magnitude,

$$a_{ph}(\lambda) = C a^*_{ph}(\lambda), \tag{11.2}$$

$$a_{dg}(\lambda) = a_{dg}(\lambda) \exp(-S(\lambda - \lambda_0)), \tag{11.3}$$

$$b_{bp}(\lambda) = b_{bp}(\lambda_0) \left(\frac{\lambda_0}{\lambda} \right)^Y, \tag{11.4}$$

where $a^*_{ph}(\lambda)$ is the chlorophyll-a specific absorption coefficient, S is the spectral decay constant for CDM absorption (Bricaud *et al.*, 1981), Y is the power law exponent for particulate backscattering coefficient, and λ_0 is a scaling wavelength (443 nm). For $a_{ph}(\lambda)$, $a_{dg}(\lambda)$, and $b_{bp}(\lambda)$, the unknown magnitudes are the chlorophyll-a concentration (C), the detritus/gelbstoff absorption coefficient ($a_{dg}(443)$), and the particulate backscatter coefficient ($b_{bp}(443)$, respectively. In

application of Equations 11.1–11.4, $a_w(\lambda)$, $b_{bw}(\lambda)$, n_w, t, and g_i are taken from the literature whereas the values of Y, S, and $a^*_{ph}(\lambda)$ were determined by "tuning" the model against a large *in situ* data set (Maritorena *et al.*, 2002) (provided in Table 11.1). The unknowns in Equations. 11.1–11.4, C, $b_{bp}(443)$, and $a_{dg}(443)$, are retrieved by applying a nonlinear least-square technique to fit Equation 11.1 $R_{rs}(\lambda)$ data (or normalized water-leaving radiance) collected at four or more wavelengths. Confidence intervals for the retrieved variables are also generated during the inversion (See Maritorena and Siegel (2005) and Chapter 3).

Table 11.1 Parameters for GSM $R_{rs}(\lambda)$ inversion.

	$a^*_{ph}(\lambda)$ [m^2 mg^{-1}]	S[nm^{-1}]	Y
412	0.00665	0.0206	1.0337
443	0.05582		
490	0.02055		
510	0.01910		
555	0.01015		

The results presented below were obtained using the set of model parameters described in Maritorena *et al.* (2002). In this version, model parameters were optimized using an *in situ* data set that consisted mostly of offshore oceanic Case 1 waters with very few stations from eutrophic waters. In order to streamline the tuning process and to limit the number of unknowns to retrieve, the parameterisation of the original GSM model includes some simplifying assumptions. In particular, several parameters are held constant in the model while they actually vary in nature. For example, $a^*_{ph}(\lambda)$ is expressed as a constant mean spectrum while a more sophisticated function could account for photoadaptation or community structure shifts (e.g., Bricaud *et al.*, 1998). Similarly, particulate backscattering is modelled using a simple function with a fixed spectral dependence (through exponent Y in Equation 11.4) while such wavelength dependence tends to disappear in turbid waters. The slope of the spectral decrease in a_{dg} absorption, S, is also held constant in the model whereas it actually depends on a complex system involving land/sea interactions, the productivity and state of the phytoplankton communities, the microbial loop and photochemistry (see also discussion in Maritorena *et al.*, 2002). Since these parameters were optimized from a large global Case 1 *in situ* data set they are generally well suited for such conditions and for the original GSM retrievals (C, $b_{bp}(443)$, and $a_{dg}(443)$). However, in waters where optical characteristics differ strongly from those used to tune the model, coastal Case 2 or phytoplankton rich waters in particular, the model performance can be significantly degraded. Although not presented here, other tuned versions of the model have been developed that are more appropriate for specific situations (*e.g.*, Santa Barbara channel coastal waters).

The GSM model was initially designed for use with SeaWiFS data, and

chlorophyll-a concentration is one of its three originally retrieved variables (Maritorena *et al.*, 2002). For consistency with some of the other models presented here, additional calculations were implemented in order to generate total and phytoplankton absorption coefficients at 440 nm as well (considered negligible difference from that at 443 nm). The total absorption coefficient was calculated by solving Equation 11.1 for $a(440)$ using the input $R_{rs}(440)$ values and the retrieved $b_{bp}(440)$. The phytoplankton absorption coefficient was then calculated by subtracting $a_w(440)$ and the retrieved $a_{dg}(440)$ value from $a(440)$. The original GSM retrieved variables have to satisfy the following criteria to be considered valid:

$0 < C < 100.0$ mg m^{-3},
$0 < a_{dg}(443) < 2.0$ m^{-1},
and, $0.0001 < b_{bp}(443) < 0.1$ m^{-1}.

11.2 Results

Taking the R_{rs} values at 410, 440, 490, 510, and 555 nm, the variables obtained by inversion of the model were compared to the known or *in situ* data using simple regression analyses. Type II regressions on log-transformed data were performed for each of the retrieved variables. The statistical parameters presented in Table 11.2 include: the slope and intercept of the regression, R^2, RMSE error, bias and the number of valid retrievals.

Table 11.2a RMSE and regression (Type II) results of the synthetic data set ($\theta_0 = 30°$). IOPs were retrieved with R_{rs} values at 410, 440, 490, 510 and 555 nm as inputs. N is the number of data tested, while n is the number of valid retrievals.

	N	n	intercept	slope	R^2	RMSE	bias
$a(443)$	500	479	0.032	1.068	0.974	0.115	-0.017
$a_{dg}(443)$	500	479	0.036	1.053	0.965	0.145	-0.013
$a_{ph}(443)$	500	479	0.162	1.171	0.957	0.173	-0.060
$b_{bp}(443)$	500	479	0.198	1.133	0.957	0.152	-0.062

Table 11.2b RMSE and regression (Type II) results of the *in situ* data set. IOPs were retrieved with R_{rs} values at 412, 443, 490, 510 and 555 nm as inputs. N is the number of data tested, while n is the number of valid retrievals.

	N	n	intercept	slope	R^2	RMSE	bias
$a(443)$	656	646	-0.034	1.097	0.838	0.223	-0.129
$a_{dg}(443)$	656	646	0.003	1.084	0.798	0.246	-0.103
$a_{ph}(443)$	656	646	0.029	1.175	0.737	0.350	-0.221

Results of the inversion using the synthetic data set are presented in Figure 11.1. Overall, the retrievals for the four variables presented show good statistical results with small negative biases and high R^2 values. Slopes are greater than 1.0 for all variables and retrievals tend to slightly underestimate synthetic values at the low end and slightly overestimate at the high end. In general, dispersion tends to increase when absorption or backscattering reaches high values because, as explained above, this version of the model is not ideal in such conditions. Also, no valid retrievals were achieved for a small portion of both synthetic and *in situ* data sets.

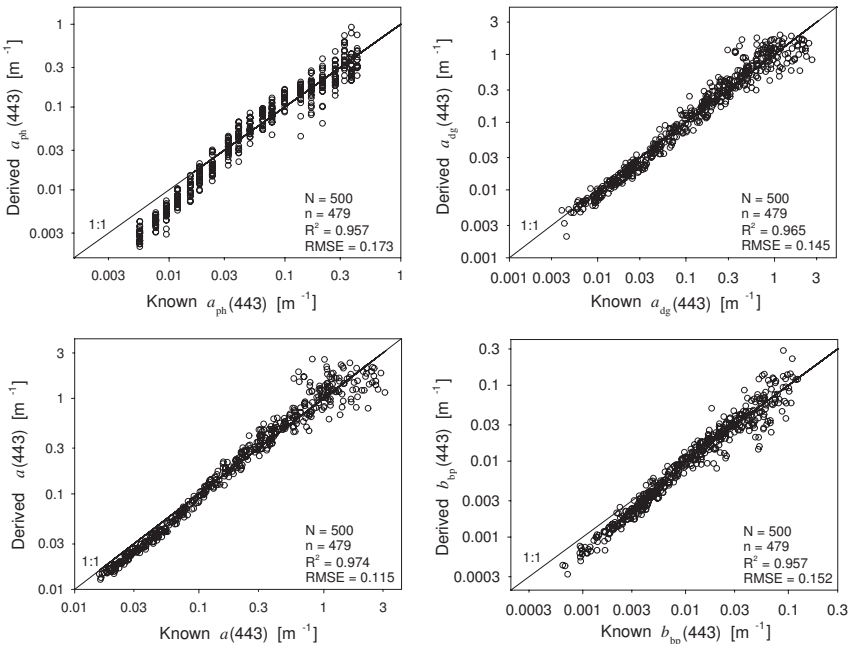

Figure 11.1 Comparison of the modelled and known IOPs for the synthetic data set (sun at 30° from zenith) using the GSM model with $R_{rs}(\lambda)$ at 410, 440, 490, 510 and 555 nm as inputs.

Figure 11.2 presents the GSM retrievals when applied to the *in situ* data set. As expected, the statistical results are slightly degraded. The dispersion is higher than with the synthetic data and R^2 values are lower. This is likely a consequence of the noise and uncertainties associated with *in situ* AOP and IOP measurements. The slopes show the same trends as with the synthetic data but are slightly higher. In general, the GSM retrievals tend to be slightly lower than the *in situ* data.

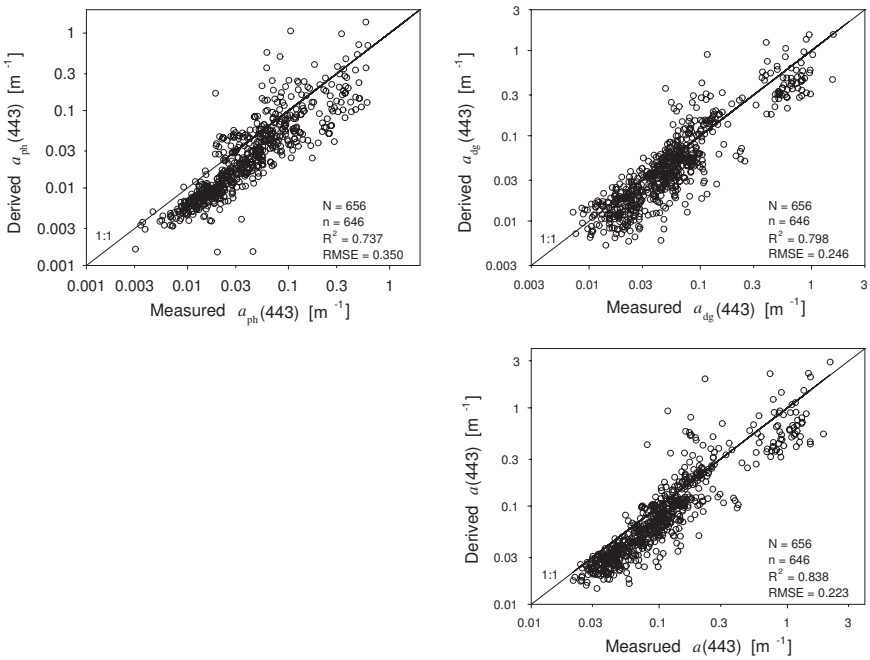

Figure 11.2 Comparison of the modelled and *in situ* IOPs using the GSM model with $R_{rs}(\lambda)$ at 412, 443, 490, 510 and 555 nm as inputs.

11.3 Conclusions

The GSM model is a simple semi-analytical ocean-colour model originally designed for use with SeaWiFS and MODIS-like satellite data over non-coastal waters. While both the synthetic and *in situ* data sets used here have a strong "coastal" component, the model performed well but as expected, its performance was lower in highly absorbing or backscattering situations. Other versions of the model exist or are being developed for specific coastal waters or to implement new features (*e.g.*, band-independent or "*Trichodesmium*" versions, Westberry *et al.*, 2005).

Chapter 12

Inversion Based on a Semi-Analytical Reflectance Model

Emmanuel Devred, Shubha Sathyendranath and Trevor Platt

The algorithm presented here is based on the theoretical reflectance model developed by Sathyendranath and Platt (1997; 1998). They used the assumption of quasi-single scattering to express the reflectance in the ocean as a function of the diffuse attenuation coefficient, K_d, which was in turn expressed as a function of IOPs. This model has since been implemented for remote sensing applications in the North West Atlantic (Sathyendranath *et al.*, 2001; Devred *et al.*, 2005) and coastal waters off Vancouver Island (Sathyendranath *et al.*, 2004). Although the model was designed primarily for application in Case 1 waters, the mathematical formulation (Sathyendranath and Platt, 1997) accounts for multiple orders of scattering, and the computer programme used in the analysis presented here incorporates scattering events up to the fifth order. Thus the model is easily adapted to more turbid Case 2 waters, such as coastal areas. Moreover, some assumptions made to develop the model (*e.g.*, value of 1.0 for the ratio of backscattering to upward-scattering coefficients) may be satisfied in turbid waters in the presence of multiple scattering. This model has been widely used for various applications ranging from chlorophyll-a concentration retrieval to primary production computations. Here it is coupled with a nonlinear, least-square fitting method to retrieve IOPs (absorption and backscattering coefficients) of marine components (phytoplankton and detrital material, dissolved and particulate) from remote-sensing reflectance, R_{rs}.

12.1 Theoretical Background

Sub-surface irradiance reflectance ($R(0^-,\lambda)$) is expressed as the ratio of upwelling irradiance (E_u) to downwelling irradiance (E_d) just below the surface. Sathyendranath and Platt (1997) showed that $R(0^-,\lambda)$ for a homogeneous water column can be expressed as:

$$R(0^-,\lambda) = \frac{s b_b(\lambda)}{\mu_d (K_d(\lambda) + \kappa(\lambda))}, \tag{12.1}$$

where $K_d(\lambda)$ and $\kappa(\lambda)$ are respectively the diffuse attenuation coefficients (m^{-1}) for downwelling and upwelling irradiance (note that $\kappa(\lambda)$ defines the rate of attenuation of upwelling light as it travels to the surface, and that this is different from the attenuation coefficient for upwelling light with increasing depth), μ_d is the average cosine for the downwelling irradiance, s is a shape factor defined as the ratio of upward-scattering coefficient b_u (m^{-1}) to backscattering coefficient b_b (m^{-1}). The parameter s takes the value of 1.0 in very oligotrophic waters where molecular scattering is dominant. The average cosine for downwelling irradiance (μ_d) just beneath the sea surface can be written as the sum of a direct and a diffuse component (Equation 12.2).

The cosine for the direct component is equal to $\cos(\theta_s)$ where θ_s is the subsurface solar zenith angle and mean cosine for the diffuse component is 0.83 (Sathyendranath and Platt, 1988). Thus, the mean cosine for the total downwelling irradiance at the sea surface is given by:

$$\mu_d = \frac{E_{dd}\cos(\theta_s)}{E_d} + \frac{0.83E_{ds}}{E_d}, \tag{12.2}$$

where E_d, E_{dd} and E_{ds} correspond respectively to the total, direct and diffuse solar radiation at the sea surface (Gregg and Carder, 1990). Further details regarding the assumptions and approximations in the ocean-colour model used here are available in Sathyendranath and Platt (1997).

Sathyendranath and Platt (1988) have expressed the diffuse attenuation coefficient as (wavelength argument is omitted here for clarity),

$$K_d = \frac{a + b_b}{\mu_d}, \tag{12.3}$$

and similarly,

$$\kappa = \frac{a + b_b}{\mu_u}, \tag{12.4}$$

where μ_u corresponds to the mean cosine for the upwelling light, which is approximated as 0.5.

From Equations 12.1–12.4, the reflectance R can be expressed as a function of backscattering and absorption coefficients of the marine components at a given wavelength. This model has also been extended to deal with stratified waters and inelastic (Raman) scattering (Sathyendranath and Platt, 1998). However, these features of the model are not exploited here to facilitate comparison with the other models in this report. The model has been used to provide a theoretical underpinning for empirical algorithms for retrieval of chlorophyll-a from ocean-colour data (Sathyendranath *et al.*, 2001), and to develop improved algorithms for chlorophyll-a retrieval for Case 1 waters of the North West Atlantic (Devred *et al.*, 2005). Here, we examine the use of a nonlinear optimization technique to retrieve optical properties of the IOCCG data sets that include both Case 1 and Case 2 waters.

12.2 The Approach

To retrieve the inherent optical properties from remote-sensing reflectance, we applied a classical nonlinear least-square fitting method to Equation 12.1. At a given wavelength, the reflectance at the sea surface is a function of five unknown parameters: $R = f(a_{\mathrm{ph}}, a_{\mathrm{g}}, a_{\mathrm{d}}, b_{\mathrm{b,ph}}, b_{\mathrm{b,p}})$ where subscripts "ph", "g", "d" and "p" stand respectively for chlorophyll (phytoplankton), yellow substances (also referred to as CDOM), detritus and other particulate material, when the absorption and backscattering coefficients in the model are expressed as the sums of their components. Note that absorption (a_{w}) and backscattering (b_{bw}) by pure seawater can be computed at a given wavelength (see respectively Pope and Fry, 1997; Morel, 1974) and do not appear as unknown parameters in the above equation. Further, based on historical measurements and bio-optical models (Bricaud *et al.*, 1981; Ulloa *et al.*, 1994; Bricaud *et al.*, 1995; Loisel and Morel, 1998; Ciotti *et al.*, 2002; Bricaud *et al.*, 2004; Devred *et al.*, 2006;), the spectral dependencies of some components are described as follows:

$$a_{\mathrm{dg}}(\lambda) = a_{\mathrm{dg}}(440)\exp[-S(\lambda - \lambda_0)], \tag{12.5}$$

for combined absorption coefficients of yellow substances (a_{g}) and detritus (a_{d}) at λ, where S, the exponential decrease of absorption with wavelength, is set to the average value of 0.014 nm^{-1}; and

$$b_{\mathrm{bp}}(\lambda) = b_{\mathrm{bp}}(440)\left(\frac{\lambda}{440}\right)^{-\log(C)}, \tag{12.6}$$

for particulate backscattering (organic and mineral). Note that the wavelength dependence is also a function of chlorophyll concentration (C) as in Sathyendranath *et al.* (2001).

The model of Sathyendranath *et al.* (2001) was used to describe phytoplankton absorption,

$$a_{\mathrm{ph}}(\lambda) = U(\lambda)(1 - \exp(-FC)) + a_2^*(\lambda)C. \tag{12.7}$$

Values of $U(\lambda)$, F and $a_2^*(\lambda)$ are provided in Table 12.1, whereas details on interpretation of these parameters can be found in Devred *et al.* (2006). The three parameters of the model were determined by fitting the model to the database from the Bedford Institute of Oceanography.

With the above prescriptions on the spectral dependencies of the optical properties of some of the components, and by combining the absorptions by detritus and yellow substances into a single component (Equation 12.5), the number of unknown parameters in Equation 12.1 is reduced to four (namely, $a_{\mathrm{ph}}(440)$, $a_{\mathrm{dg}}(440)$, $b_{\mathrm{bp}}(440)$ and C). When remote-sensing reflectance at 410, 440, 490, 510, 555 and 670 nm are available from ocean-colour sensors (for example, SeaWiFS, MODIS and MERIS, which are the most commonly-used), we get

Table 12.1 Parameters for $a_{\mathrm{ph}}(\lambda)$ model.

wavelength	$U(\lambda)$	$a_2^*(\lambda)$ [m^2 mg^{-1}]	F
412	0.0369	0.0243	1.582
490	0.0338	0.0129	
510	0.0180	0.0114	
555	0.0036	0.0070	
670	0.0089	0.0172	

a system of six equations with four unknowns. This facilitates the convergence on the solution for the four unknowns. Note that parameters $b_{\mathrm{bp}}(\lambda)$ and $a_{\mathrm{ph}}(\lambda)$ are related to C through Equations 12.6–12.7.

To apply our approach to the IOCCG data sets (both synthetic and *in situ*), the reflectance R was estimated from remote-sensing reflectance, R_{rs}, using:

$$R = \frac{n_{\mathrm{w}}^2}{t^2} Q R_{\mathrm{rs}}. \tag{12.8}$$

Here $n_{\mathrm{w}}^2/t^2 (\approx 1.89)$ accounts for the air-sea interface effects, and Q converts radiance to irradiance. It is known that the factor Q varies with solar zenith angle, sea-surface roughness (wind-induced) and substances present in the water. Here, the dependence of Q on solar zenith angle was computed using the model of Åas and Højerselev (1999) and an empirical function (Devred *et al.*, 2005) was used to compute the dependence of Q on chlorophyll content (Morel and Gentili, 1993).

12.3 Results and Discussion

We used remote-sensing reflectance at 410, 440, 490, 510, 555, and 670 nm (note that $R_{\mathrm{rs}}(670)$ is not available for the *in situ* data set) of the IOCCG data sets to derive total, phytoplankton, and detrital (dissolved and particulate) absorption coefficients, and particulate backscattering coefficient at 440 nm.

12.3.1 Retrieval of IOPs from the simulated data set

The interest in inverting synthesized data lies in the control of all environmental variables such as the sea surface state, solar zenith angle and optical properties. It is then possible to assess accurately the performance of the reflectance model and the fitting method to retrieve inherent optical properties.

Figure 12.1 shows derived versus synthesized total, phytoplankton and detritus absorption coefficients and particulate backscattering at 440 nm for data with a solar zenith angle of 30°. The retrieved data are consistent with the simulated data. For each of the derived IOPs, the optimization method failed to

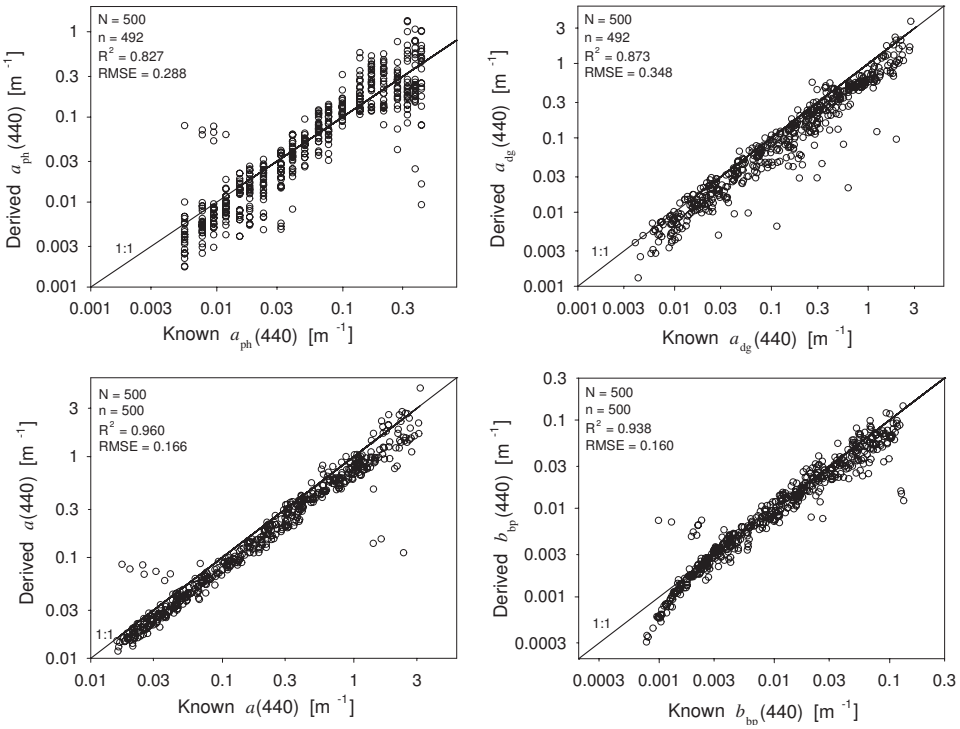

Figure 12.1 Comparison between retrieved and simulated IOPs for a solar zenith angle of 30°. IOPs were retrieved using R_{rs} values at 410, 440, 490, 510, 555 and 670 nm.

retrieve the parameters in eight cases for absorption of phytoplankton and yellow substances (with detritus). Linear regression (Type II) on log-transformed data (omitting the cases where convergence was not obtained) gave slopes close to 1.0 (except for phytoplankton absorption with a slope of 1.16) with a small negative bias for all variables (Table 12.2). Note that similar results were also achieved with the synthesized data of 60° solar zenith angle (not shown). This demonstrates that the assumptions made on the spectral dependence of the IOPs are suitable for ocean-colour inversion.

Matching of phytoplankton absorption coefficients presents the poorest agreement (although still acceptable) with a slope of 1.156 and a bias of -0.053. It also exhibits the lowest correlation coefficient with a value of $R^2 = 0.827$. One observes an increase in discrepancy in the retrieved data (Figure 12.1) as $a_{ph}(440)$ increases. This is probably due to the phytoplankton absorption model used in our algorithm. It is noteworthy that the retrieved total absorption at 440 nm shows a better agreement than does the retrieved phytoplankton absorption. At low backscattering coefficients ($b_{bp}(440) < 0.002$ m^{-1}) our algorithm showed a

Table 12.2 RMSE and regression (Type II) results for the synthetic data set (Sun at 30°). IOPs were retrieved using R_{rs} values at 410, 440, 490, 510, 555 and 670 nm. N is the number of data tested, while n is the number of valid retrievals.

	N	n	intercept	slope	R^2	RMSE	bias
$a(440)$	500	500	-0.122	0.974	0.960	0.166	-0.104
$b_{bp}(440)$	500	500	-0.093	0.981	0.938	0.160	-0.056
$a_{ph}(440)$	500	492	0.145	1.156	0.827	0.288	-0.053
$a_{dg}(440)$	500	492	-0.119	1.090	0.873	0.348	-0.200

systematic underestimation of the retrieved backscattering. It probably results from the formulation of the spectral dependence of the backscattering coefficients as a function of chlorophyll concentration. This approach may not be appropriate at low chlorophyll concentrations, and therefore for low backscattering coefficients. We will explore this problem further.

12.3.2 Retrieval of IOPs from the *in situ* data set

Inversion of *in situ* measurements becomes more challenging not only because the parameters defined in the previous section (IOPs, sun angle, vertical profile) show random and/or systematic variability in their natural environment, but also because external variables (for example, measurement errors) add perturbation to the entire system (defined here as the reflectance/IOP pairs). We can therefore expect a higher variability when retrieving the IOPs as confirmed in Figure 12.2. Only results for absorption coefficients are shown in Figure 12.2 because backscattering measurements were not available.

Table 12.3 RMSE and regression (Type II) results for the *in situ* data set. IOPs were retrieved using R_{rs} values at 410, 440, 490, 510 and 555 nm. N is the number of data tested, while n is the number of valid retrievals.

	N	n	intercept	slope	R^2	RMSE	bias
$a(443)$	656	656	0.011	1.048	0.762	0.218	-0.036
$a_{ph}(443)$	656	656	0.654	1.537	0.648	0.442	-0.110
$a_{dg}(443)$	656	491	0.416	1.312	0.380	0.470	-0.003

The standard deviation has increased for all of the matching pairs (Table 12.3). Retrieved phytoplankton absorption coefficients show the highest discrepancy with the *in situ* data (slope of 1.537 and bias of -0.110), perhaps because of the performance of the absorption model. Previous works (Burenkov *et al.*, 2001; Reynolds *et al.*, 2001; Sathyendranath *et al.*, 2001; Gohin *et al.*, 2002; Devred *et al.*, 2005) showed that local bio-optical models should be preferred to global ones. This type of approach would likely decrease the discrepancy

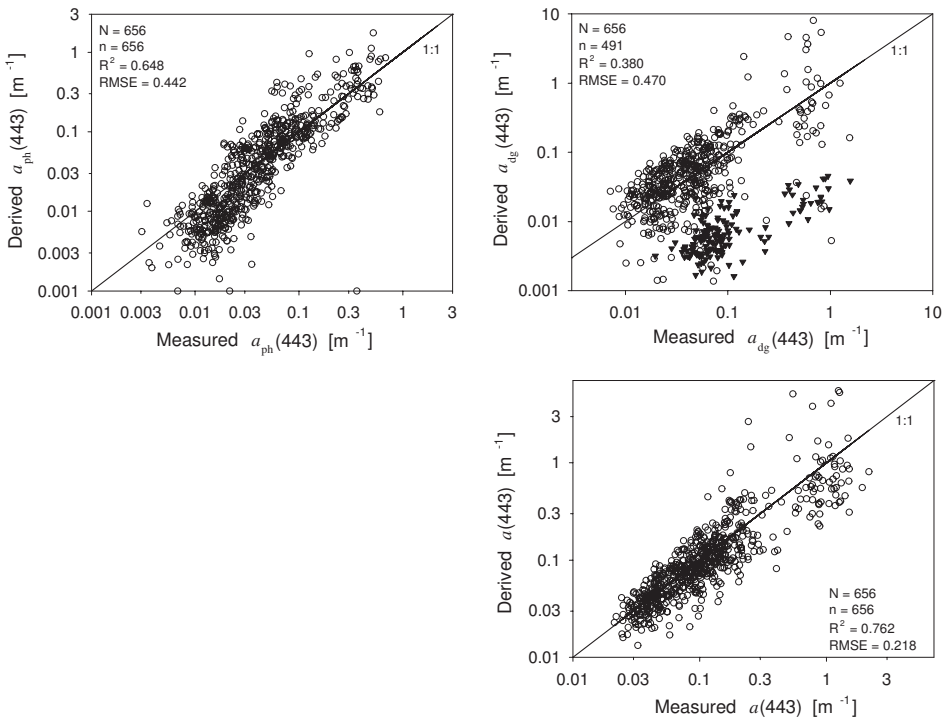

Figure 12.2 Comparison between retrieved and *in situ* IOPs. IOPs were retrieved using R_{rs} values at 412, 443, 490, 510 and 555 nm.

between the retrieved and *in situ* data. Comparison between retrieved and *in situ* absorption coefficients of yellow substances and detritus is also less consistent (slope of 1.312 and bias of -0.003) than the previous case (synthesized data set). In Figure 12.2, cases where the fitting procedure for $a_{\mathrm{dg}}(440)$ failed to converge are shown as filled triangles. These points were not retained in the statistical analysis (resulting in a smaller number of samples). The total absorption coefficients show a good agreement with a slope of 1.048 and a bias of -0.036. This is not inconsistent as phytoplankton absorption seemed to be slightly overestimated while yellow substances are underestimated. These effects cancelled each other, resulting in a better agreement when comparing the total absorption coefficients.

12.4 Conclusion

The reflectance model of Sathyendranath and Platt (1997), although based on the quasi-single scattering assumption, proved to be robust when applied to a great variety of optical marine environments: cases ranging from low to high

albedo (scattering to absorption coefficients ratio).

Retrieval of inherent optical properties shows better accuracy when performed on the synthesized data set at low solar zenith angle. A small decrease in the accuracy was observed as solar zenith angle increased (not presented). A greater discrepancy occurred when retrieving phytoplankton absorption at 440 nm than for other IOPs. This may be explained by the phytoplankton absorption model used in our algorithm. However, retrieval of the total absorption coefficient seems not affected by this feature. Our algorithm underestimated backscattering coefficients at small values, perhaps a limitation of our bio-optical model adapted from Loisel and Morel (1998).

For the *in situ* data set, our algorithm yielded consistent results, although a greater variability around the 1:1 line was observed than that observed when inverting the synthesized data set. We showed that an underestimation (overestimation) of retrieved phytoplankton absorption lead to an overestimation (underestimation) of retrieved yellow substances absorption (not knowing which one is the cause). This will be further analysed to improve the performance of our algorithm. However, our algorithm yielded results comparable to other models reported here.

Chapter 13

Examples of IOP Applications

Robert Arnone, Hubert Loisel, Kendall Carder, Emmanuel Boss, Stephane Maritorena and ZhongPing Lee

The IOPs retrieved from ocean colour provide innovative tools and opportunities for oceanographic studies, as their values can be used directly or indirectly to study biological and biogeochemical processes in the oceans (Gould and Arnone, 1997; Bissett *et al.*, 2001; Coble *et al.*, 2004; Hu *et al.*, 2004, 2005). For instance, earlier studies (Kirk, 1984; Sathyendranath and Platt, 1988) have shown that the diffuse attenuation coefficients of the water can be adequately estimated from water's inherent optical properties. Recent studies (Stramski *et al.*, 1999; Loisel *et al.*, 2001a; Balch *et al.*, 2005) have shown that particulate carbon can be well estimated from particle backscattering coefficient. Further, a new generation of biological models (Bissett *et al.*, 2005; Penta *et al.*, 2005) now integrate explicitly two or more species of plankton, as well as dissolved (DOC) and particulate organic carbon (POC), whereas IOPs play important roles in observing and monitoring blooms of red tides (Cullen *et al.*, 1997; Cannizzaro *et al.*, 2006). As confidence in the IOP products continues to grow, our understanding of how IOP properties are linked to ocean processes expands. This research is moving the ocean community beyond the traditional applications centered on the oceanic chlorophyll-a. In this chapter, we present some examples of IOP applications in this regard.

13.1 Water Composition and Water-Mass Classification

The absorption and backscattering coefficients bring some complementary information on the water composition, because of their different sensitivity to the various optically significant materials in water. While the absorption coefficient is affected by the presence of both suspended and dissolved material in water, the backscattering coefficient represents the concentration (to first order) of organic and inorganic suspended particles, and bubbles. The decomposition of the total absorption coefficient into its different components, as discussed in Chapter 1, allows the monitoring of phytoplankton and of the remaining absorbing

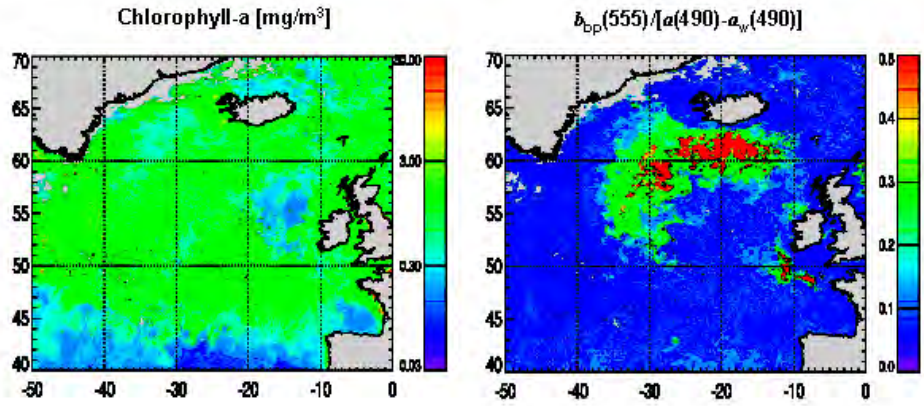

Figure 13.1 Comparison between the SeaWiFS-chlorophyll concentration and the ratio of the particle backscattering to absorption obtained from an inverse algorithm (Loisel and Stramski, 2000) over the North Atlantic (south Island) in June 1998. As seen, C and $b_{bp}(555)/(a(490)\text{-}a_w(490))$ represent different patterns, with the latter clearly showing different particle populations. These particles have been identified as coccolithophorid, which are characterized by a high backscattering efficiency.

materials. Therefore, synoptic satellite observations of a and b_b give a valuable picture of composition of surface waters. For example, the b_{bp}/a ratio may be used to discriminate different families of particles (Figure 13.1).

New applications have also used the IOP characteristics of the water as a tool to fingerprint a water mass and identify the controlling optical processes (Traykovski and Sosik, 2003; Arnone and Parsons, 2004). Besides water absorption, the total absorption is additionally composed of the absorption from CDOM, detritus and phytoplankton (see Chapter 1). By defining the percent contribution of each of these components, a water mass can be defined by which component controls the absorption budget. A ternary plot of these three components provides a useful method for fingerprinting water mass and the dominant absorption process (Gould and Arnone, 2003; Arnone *et al.*, 2004). This method has been applied to satellite absorption properties derived from semi-analytical algorithms for SeaWiFS and MODIS ocean-colour imagery (Figure 13.2a). This water-mass classification can be represented by an RGB image representing percent detritus, phytoplankton and CDOM absorption (Figure 13.2b). These images easily illustrate the controlling biogeochemical processes for monitoring coastal and offshore water masses. Note that this classification method identifies the dominance of the absorption processes, and not the absolute values of the absorption coefficients. This classification method can be used on sequential satellite images of the absorption components to identify changes in absorption processes and to track water masses based on a specific fingerprint of the absorption components.

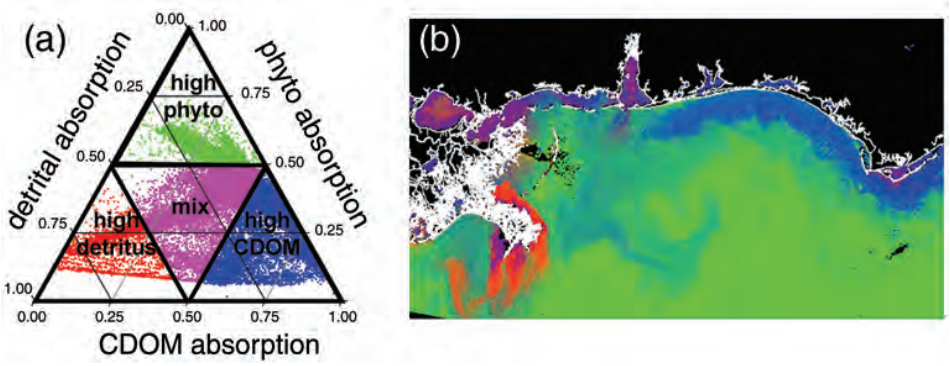

Figure 13.2 (a) Water-mass classification from the absorption budget. Ternary plot of the percent absorption attributed to detritus, CDOM and phytoplankton for each pixel to identify the dominant components. (b) RGB image of percent absorption of detritus (red), phytoplankton (green) and CDOM (blue). Absorption products derived from SeaWiFS were used to determine the absorption budget. Intensity of the colour indicates the dominant component

13.2 Dissolved and Particulate Organic Carbon

Examination of the temporal variations of absorption and backscattering coefficients and comparison with that of chlorophyll over the global ocean have also provided important information about the dynamics of marine particles and dissolved organic carbon, because the absorption and backscattering coefficients are related to different biogeochemical parameters. For instance, the feasibility of estimating POC (in mg m^{-3}), and the coloured detrital and dissolved materials (CDM) (in m^{-1}), from the remotely detected b_b and a was recently demonstrated (Stramski *et al.*, 1999; Loisel *et al.*, 2001b; Loisel *et al.*, 2002; Siegel *et al.*, 2002; Balch *et al.*, 2005) (see Figures 13.3 and 13.4). A phase shift between the annual cycles of b_{bp} and chlorophyll was evidenced, and was attributed to the presence of a pool of non-pigmented particles originating from the accumulation of dead phytoplankton cells, as well as zooplankton detritus, in the summer stratified surface layer (Loisel *et al.*, 2002). The decrease of the Chl/POC ratio in living phytoplankton at high irradiance in summer was also used to explain the lag between the Chl and b_{bp} maxima (Loisel *et al.*, 2002).

Figure 13.4 shows global distributions of CDM of two seasons in 1998, derived from SeaWiFS data (Siegel *et al.*, 2002). Clearly, there are significant spatial and temporal variations in global CDM (a part of DOC). Because POC and CDM represent different pools of carbon stored in oceans, and since CDM plays an important role in regulating subsurface blue/ultraviolet radiation (Siegel *et al.*, 2002), analysis of their spatial/temporal distributions is important for the understanding of the carbon cycles in oceans.

Behrenfeld *et al.* (2005), using backscattering and chlorophyll-a derived from

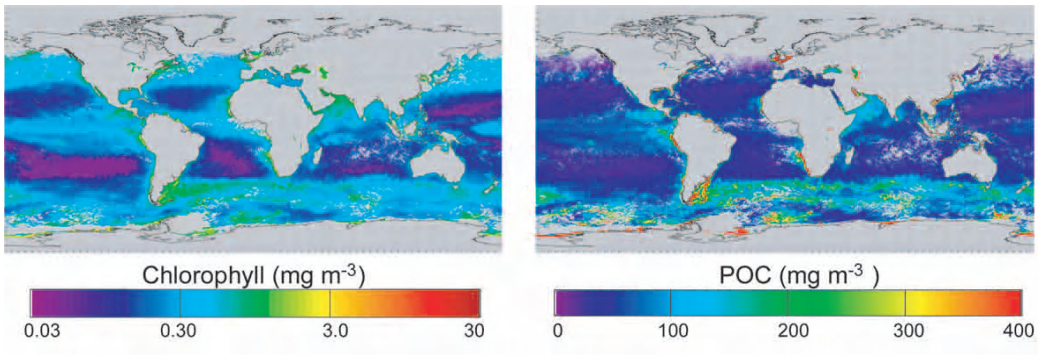

Figure 13.3 Global chlorophyll (SeaWiFS product) and POC distribution in January 2000 (adapted from Loisel *et al.*, 2002).

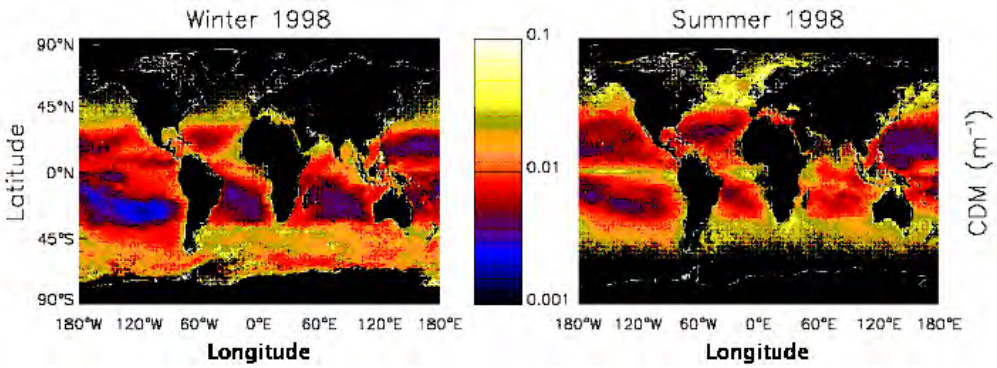

Figure 13.4 Global distribution of CDM (in m^{-1}) derived from SeaWiFS data by the GSM algorithm (Chapter 11) (adapted from Siegel *et al.*, 2002).

R_{rs} as inputs, also developed a novel primary production model based on the physiological link between phytoplankton growth rate and growth conditions (temperature, nutrients, and light) as reflected in the ratio of chlorophyll to carbon of phytoplankton. This novel (and debatable) approach is to use the backscattering coefficient to estimate phytoplankton biomass and assuming a linear relation between total POC and phytoplankton biomass. The observed change (Figure 13.5) in the ratio of chlorophyll-a to phytoplankton carbon is interpreted as reflecting a physiological change, rather than a change in the particulate composition. Net primary production is then computed from the estimated growth rate through a simple multiplication by the phytoplankton carbon and a function that accounts for its vertical distribution with depth.

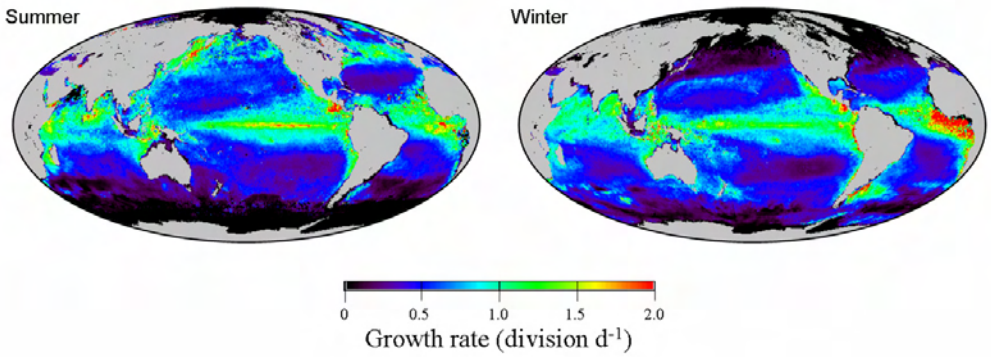

Figure 13.5 Phytoplankton growth rates for Boreal summer (June to August) and winter (December to February). Adapted from Behrenfeld *et al.* (2005).

13.3 Diffuse Attenuation Coefficient of Downwelling Irradiance

The availability of absorption (a) and backscattering coefficients (b_b) also makes it straightforward to calculate the diffuse attenuation coefficient of downwelling irradiance, either at a single wavelength ($K_d(\lambda)$) or for the broad band (350 - 700 nm) visible domain (K_{vis}). Because both K_d and K_{vis} are apparent optical properties, they are directly linked to the IOPs (Sathyendranath and Platt, 1988; Gordon, 1989; Lee *et al.*, 2005a,b). Traditionally, estimation of K_d is based on the spectral ratios of $L_w(\lambda)$ or $R_{rs}(\lambda)$. Such an approach does not reveal the fundamental relationship between AOPs and IOPs, and is found to work only for waters with limited dynamic range (Mueller, 2000). Figure 13.6(a) shows a comparison between measured $K_d(490)$ and R_{rs} derived $K_d(490)$, for a wide range of $K_d(490)$ (0.04 - 4.0 m^{-1}) measured from different regions and at different times, using an algorithm based on a and b_b whose values were derived first from R_{rs} (Lee *et al.*, 2005b). Clearly, excellent agreement is achieved between the two independent measurements and determinations.

K_{vis} (wavelength range of 350 - 700 nm) is a parameter needed for models of oceanic photosynthesis and heat transfer in the upper water column. K_{vis} varies significantly from the surface to depth (z), even for vertically homogeneous waters, which is different from the characteristics of K_d. To represent this vertical variation, earlier studies used multiple exponential terms to describe the vertical propagation of visible solar radiation, with the coefficients of these multiple terms expressed as empirical functions of chlorophyll (Morel and Antoine, 1994; Ohlmann and Siegel, 2000). Again, realizing the intrinsic limitations between an optical property (*e.g.*, K_{vis}) and chlorophyll, a model has been developed (Lee *et al.*, 2005a) that can be used to adequately estimate the vertical variation of K_{vis}

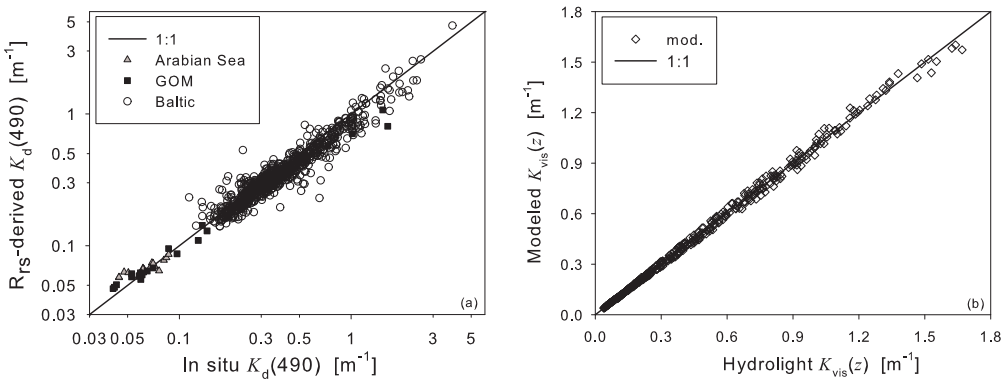

Figure 13.6 (a) Measured $K_d(490)$ vs R_{rs}-derived $K_d(490)$. In the derivation of K_d from R_{rs}, values of a and b_b were derived from R_{rs} first, and then K_d is calculated based on these a and b_b values (from Lee *et al.*, 2005b). (b) modelled $K_{vis}(z)$ compared with $K_{vis}(z)$ from Hydrolight simulations (adapted from Lee *et al.*, 2005a).

when values of $a(490)$ and $b_b(490)$ are available. Figure 13.6(b) shows modelled K_{vis} compared with Hydrolight-calculated K_{vis} for different values of a, b_b, and z. The average difference between the two sets of $K_{vis}(z)$ is 2.2%.

13.4 Oceanic Primary Production

Knowing the values of IOPs can also provide some basic information for the estimation of oceanic primary production. Currently, this estimation is done centred on the values of chlorophyll-a concentration (Platt and Sathyendranath, 1988; Behrenfeld and Falkowski, 1997). When chlorophyll is used as an input parameter representing the function of phytoplankton, a value regarding the chlorophyll-specific absorption coefficient is also explicitly or implicitly utilized. Numerous field measurements (Bricaud *et al.*, 1995; Cleveland, 1995; Lutz *et al.*, 1996; Bricaud *et al.*, 1998) and theoretical studies (Bricaud and Morel, 1986) have pointed out that this property varies widely from place to place and time to time, therefore large uncertainties are automatically introduced when this parameter is involved. Because primary production measures the conversion of solar energy absorbed by phytoplankton to sustenance in the photosynthetic process (Morel, 1978; Smith *et al.*, 1989), remotely derived or locally measured phytoplankton absorption and other IOPs can then be utilized directly in this estimation (Zaneveld *et al.*, 1993). One example of taking this approach is demonstrated in Lee *et al.* (1996a), with Figure 13.7 showing primary production calculated from values of R_{rs} (along with other auxiliary information) compared with primary production measured from *in situ* incubation.

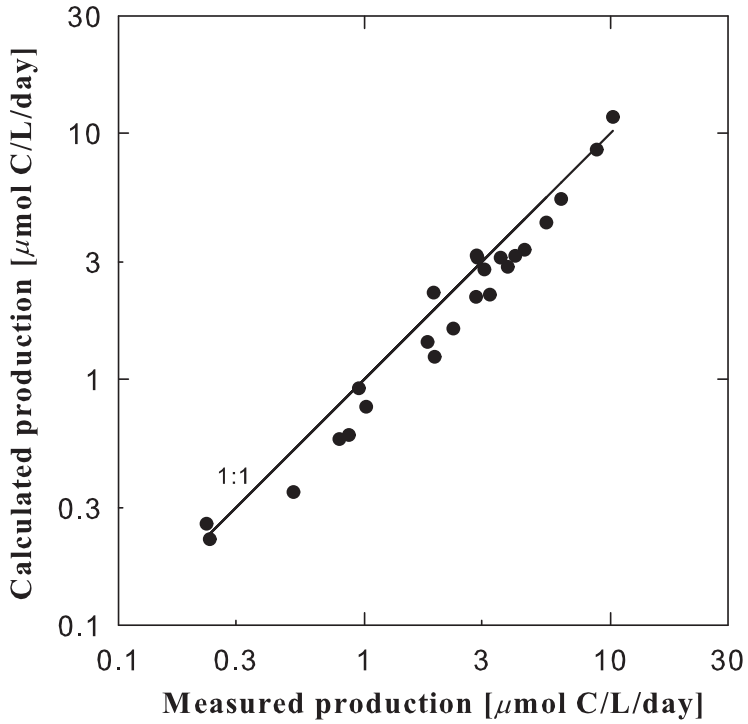

Figure 13.7 Daily primary production calculated from R_{rs} versus that from *in situ* incubation. Adapted from Lee *et al.* (1996a)

13.5 Chlorophyll Concentration from Remotely Derived Pigment Absorption Coefficient

When the absorption coefficient of phytoplankton pigment is derived from ocean colour, it adds the possibility of deriving the concentration of chlorophyll-a (Carder *et al.*, 1999; Lyon *et al.*, 2004) for different regions of the world, as indicated in Carder *et al.* (1999). Applying the semi-analytic code (Carder *et al.*, 1999) to an upwelling site (Smyth *et al.*, 2002) and a river-plume site (Hu *et al.*, 2003), it provided much more realistic estimations of chlorophyll concentration for both cases (where the empirical band-ratio approach (OC4) underestimated the high chlorophyll concentrations of the upwelling site and overestimated chlorophyll concentration for gelbstoff-rich river-plume regions). MODIS-Terra chlorophyll images from the GES DAAC (Goddard Earth Science Distributed Active Archive Center) derived by the semi-analytic code (chl_a_3) and empirical-ratio code (chl_a_2) were composited in 39-km bins for December 2000 and are shown in Figure 13.8. The subtropical gyre regions appear similar for the two images, but the chlorophyll values are clearly elevated with the semi-analytic code for the high-latitude and equatorial upwelling regions which have higher pigment concentrations.

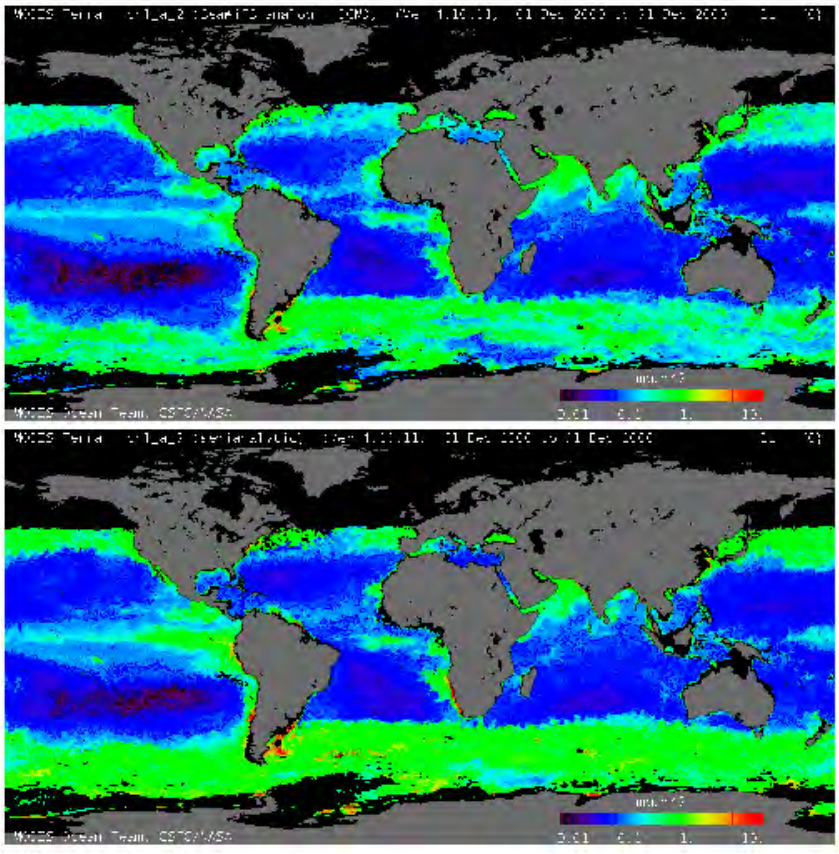

Figure 13.8 Global composited maps (December 2000) of chlorophyll-a concentration (mg m^{-3}) retrieved using empirical (top) and semi-analytic (bottom) algorithms from MODIS-Terra radiometry (adapted from Carder *et al.*, 2004).

13.6 Monitoring Coastal Ocean Processes using IOPs and Numerical Circulation Models

IOPs provide an improved capability to understand how physical processes influence the bio-optical processes (Bissett *et al.*, 2001; Arnone and Parsons, 2004). For instance, ocean colour IOP products from MODIS and SeaWiFS are being integrated with numerical circulation models. The Navy Coastal Ocean Model (NCOM) is forced by large scale ocean models which currently assimilate sea surface height from altimetry and sea surface temperature (SST) from AVHRR. These models are at 32-degree resolution with 41 sigma levels to characterize the mesoscale features (http://www7320.nrlssc.navy.mil/global_ncom/). Overlaying the modelled properties (currents, salinity, surface heights) with optical properties adds continuity to understanding IOP image products. This fusion of physical models and IOP imagery enables improved understanding of the distri-

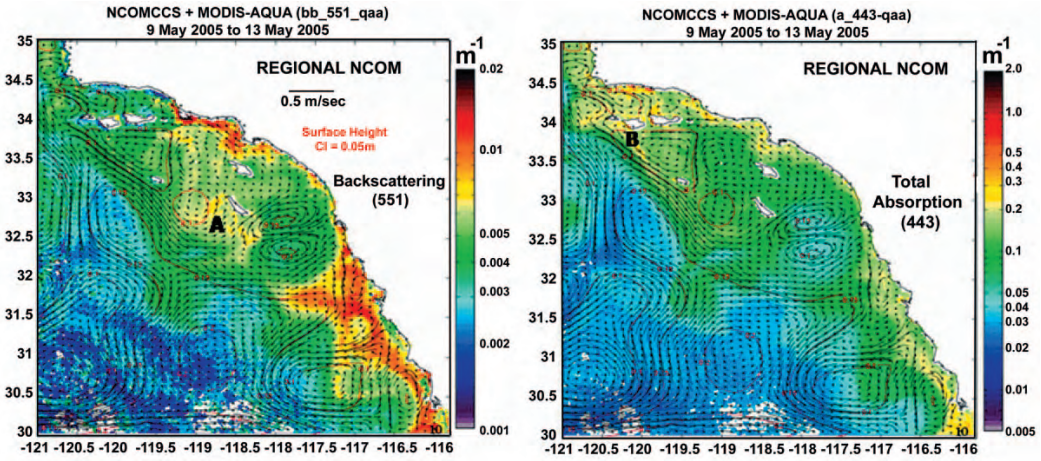

Figure 13.9 The circulation along the California Coast develops coastal filaments shown in surface currents and MODIS-Aqua IOP products. Differences in the locations of backscattering at 551 nm (associated with particles) and the total absorption at 443 nm (detritus, CDOM and phytoplankton) indicate varying bio-optical processes within these filaments.

bution of bio-optical processes that are linked with mesoscale ocean circulation features. Different IOP properties, such as backscattering, CDOM and phytoplankton absorption respond differently to mesoscale processes. Along the U.S. West coast, filaments associated with the California Current System are driven by the physical circulation as shown in Figure 13.9 (Shulman *et al.*, 2004; Penta *et al.*, 2005). The corresponding IOP distribution within these filaments is used to define the response of bio-optical processes. For example, the influence of the strong southerly flow off the Channel Islands is characterized by backscattering and total absorption products. Within this filament, the elevated particles are located south of the strong flow (point A) as shown in the $b_b(551)$ image (a result of advection), whereas the strongest currents (point B) located close to land have elevated total absorption as shown in the $a(443)$ image (a result of coastal upwelling). Divergent and convergent mesoscale fronts are revealed by the IOP properties observed in satellite imagery (Figure 13.9). Similar differences in the distribution of backscattering and absorption have been observed by Otero and Siegel (1995).

13.7 Conclusions

Our understanding of how the optical properties of water constituents are related to ocean processes has advanced significantly in the last decade. Use of IOPs to characterize ocean processes provides improved methods for monitoring and understanding the role of the oceans on a global scale. Because IOPs are

closely associated with the water leaving radiance measured by satellites and IOP retrievals are robust and stable as shown in previous chapters, IOP products are critical for monitoring and detecting changes in the ocean's climatology and forecasting ocean biogeochemical processes.

Chapter 14

Summary and Conclusions

ZhongPing Lee, Ronald Zaneveld, Stephane Maritorena, Hubert Loisel, Roland Doerffer, Paul Lyon, Emmanuel Boss, Kendall Carder, Emmanuel Devred and Robert Arnone

Most algorithms used in ocean colour remote sensing attempt to derive, directly, the concentrations of water constituents, mainly phytoplankton chlorophyll concentration. In this report, however, we present and discuss algorithms which have been developed to derive inherent optical properties (IOPs) from water-leaving radiance, in a one-step or multi-step process. The IOPs are then decomposed into the contributions by different optical components, such as absorption by phytoplankton pigments, and finally the IOPs of different components are converted into concentrations.

IOPs are the fundamental parameters of hydrological optics. The IOPs, in combination with radiances from the sun and sky, determine water-leaving radiance, which in turn defines water colour (an apparent optical property). At the same time, IOPs are also environmental properties. Their variations are directly related to changes in concentration, size distribution and composition of particulate matter and/or dissolved constituents. IOPs derived from remote sensing of ocean colour provide innovative opportunities for environmental observation and oceanographic studies on time and space scales not achievable with *in situ* measurements.

To derive, accurately, various IOPs from water colour, as presented here, is not a simple task. This report presents some frequently encountered methods for IOP retrieval. These algorithms have different levels of complexity; some are explicit about all elements and derivation processes, some are implicit; some have fewer empirical inputs, while others have more empiricism built into them. Table 14.1 highlights their similarities and major characteristics.

When presenting and comparing models, it is always useful to remember that models, by their very nature, represent some sort of reduction, or simplification. It naturally follows that practically all models will have some limitation when they attempt to mimic nature. Thus there is often a need to tailor models for specific applications or for specific regions. If models are applied for purposes for which they were not designed, there is always a risk of poor per-

Table 14.1 Algorithm highlights. L98 - Spectral-ratio algorithm (Lee *et al.* 1998, Chapter 4); B99 - Spectral curvature algorithm (Barnard *et al.* 1999, Chapter 4); MM01 - Spectral-ratio algorithm (Morel and Maritorena, 2001, Chapter 4); Loisel - Inversion of IOP (Chapter 5); D&S - MERIS Neural Network Algorithm (Chapter 6); Lyon - Linear Matrix Inversion (Chapter 7); Boss - Over constrained Linear Matrix Inversion (Chapter 8); Carder - MODIS semi-analytical algorithm (Chapter 9); QAA - Quasi-Analytical Algorithm (Chapter 10); GSM - Garver, Siegel and Maritorena semi-analytical model (Chapter 11); SPD - Sathyendranath, Platt and Devred semi-analytical reflectance model (Chapter 12).

Algorithm	**Type**	**Key features**
L98	Empirical	Empirical constants; products at 440 nm only
B99	Semi-empirical	Relationships between total absorption coefficients
MM01		Bio-optical models; hyperspectral
Loisel		$K_d(\lambda)$ from $R_{rs}(\lambda)$ empirically
D&S	Neural Network	Neural constants; MERIS only
Lyon	Algebraic *(Linear Matrix Inversion)*	Spectral models for $a_{ph}(\lambda)$, $a_{dg}(\lambda)$, and $b_{bp}(\lambda)$
Boss		Varying spectral shapes for $a_{ph}(\lambda)$, $a_{dg}(\lambda)$, and $b_{bp}(\lambda)$; statistical selection of solution; generates output confidence intervals; applicable to multi- and hyperspectral data
Carder	Algebraic for low absorption waters (*iterative solution*); empirical for other	Spectral models for $a_{ph}(\lambda)$, $a_{dg}(\lambda)$, and $b_{bp}(\lambda)$; empirical coefficients for different properties
QAA	Algebraic	Separate derivations for the total and individual components; spectral models for $a_{dg}(\lambda)$ and $b_{bp}(\lambda)$; retrieve multi- or hyperspectral a_{ph} spectrum
GSM	Spectral optimization	Optimized spectral shapes for $a_{ph}(\lambda)$, $a_{dg}(\lambda)$, and $b_{bp}(\lambda)$; applicable to multi- and hyperspectral data; can use input uncertainties and generates output confidence intervals
SPD		Varying spectral shapes for $a_{ph}(\lambda)$, $a_{dg}(\lambda)$, and $b_{bp}(\lambda)$; applicable to multi- and hyperspectral data

formance. Thus a golden rule in application of algorithms (and algorithms are a type of model) is to test them always for the specific application or region envisaged, before routine use is made of the algorithm. But knowledge of the features of the model would often help in making the initial selection of an algorithm for a particular application. For example, it is often useful to know if a particular algorithm is non-linear or not; if it is purely empirical or if it is based on theoretical considerations; if it is multi-variable or not; if it is computationally demanding or not. Such relevant features of the algorithms presented in this report are shown in Table 14.1 and Figures 14.1 - 14.4. But, as is often the case with summary tables and figures, they do not represent the whole story, but merely highlight some emergent properties when all models were made as

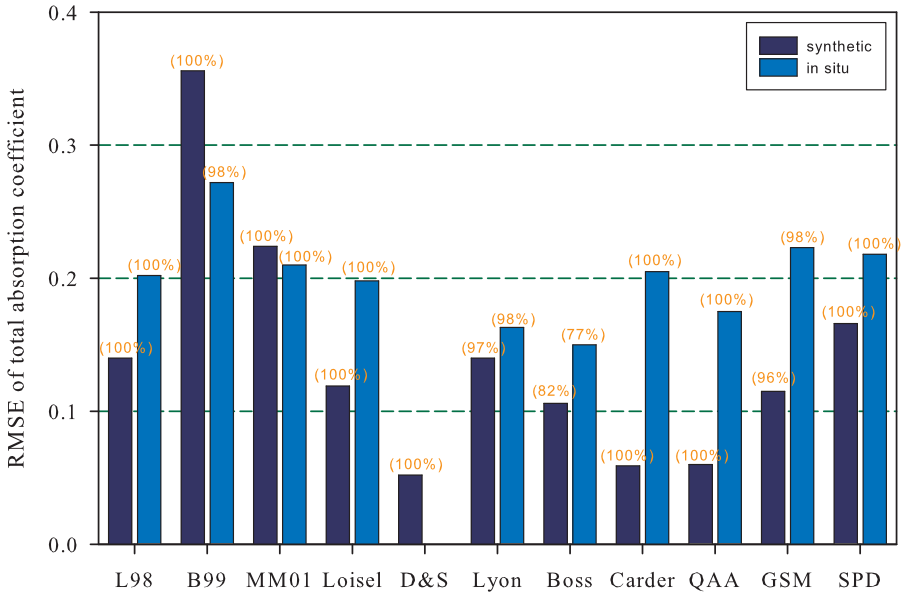

Figure 14.1 RMSE values for total absorption coefficient of both synthetic and *in situ* data sets, for all algorithms tested (see Table 14.1 for notation of algorithms). The "Lyon" results are for 410 nm, while all other results are in the vicinity of 442 nm. Numbers in parenthesis indicate percentage of valid retrievals for each algorithm. Invalid retrievals are excluded from the calculation of RMSE and other statistical analyses.

comparable as possible, for the purpose of this report.

The RMSE errors presented in Figures 14.1 - 14.4 not only represent the performance of each algorithm, but show also the deviation of the bio-optical model behind each algorithm, from that of the bio-optical model used to prepare the synthetic data set. In addition, the RMSE errors for the *in situ* data set include uncertainties associated with field measurements. It should be noted that not all the algorithms tested used the same number of spectral bands, and some algorithms used fewer bands than what they can potentially use (especially for the synthetic data set).

An inversion algorithm works as a mathematical filter analagous to physical or chemical filters used in the lab or field. In this filtering process, uncertainties are introduced, explicitly or implicitly, into the desired products. More uncertainties are introduced when fewer parameters are under control. Clearly, the results of the various algorithms indicate that there remains room for improvement in the derivation of IOPs from ocean colour. As new information becomes available, it is anticipated that the present algorithms could be revised, or exciting new methods could be developed. It is natural that algorithm development is always a continuing and evolving process.

Nevertheless, we can safely draw the following conclusions based on the

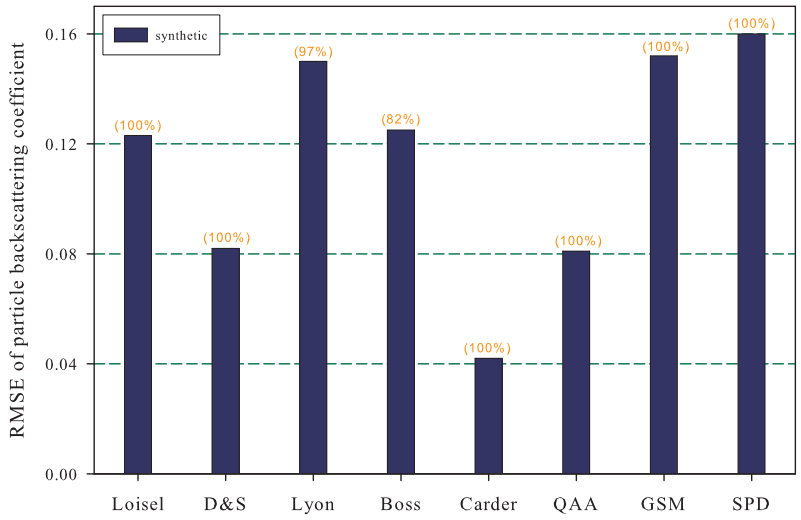

Figure 14.2 As Fig. 14.1, but for particle backscattering coefficient (synthetic data set only).

presentations and discussions of the various algorithms:

1. In general, the best properties that can be obtained from ocean-colour data, regardless of the algorithm used (see Figures 14.1 to 14.4) and as expected from the inversion of radiative transfer (see Figure 1.3), are the spectral absorption and backscattering coefficients of the total water volume.
2. Using the synthetic data set as a reference (the *in situ* data set prevents the separation of algorithm error from measurement error), more reliable results are obtained for clearer waters ($a(440) < \sim 0.3$ m^{-1}). Due to limitations of algorithm architecture and availability of reliable remote-sensing reflectance at specified wavelengths, less accurate results are generally obtained for more absorbing waters ($a(440) > \sim 0.3$ m^{-1}).
3. When decomposing the total absorption coefficient into the components of phytoplankton and coloured material, less accurate results (see Figures 14.3 and 14.4) are anticipated due to overlapping of spectral signals and because the spectral shapes of the components are not constant.
4. If the chlorophyll-a concentration (C) is desired from ocean colour, more uncertainties will be introduced because the chlorophyll-specific absorption coefficient is not constant at a given wavelength, nor is the relationship between backscattering and chlorophyll well defined.
5. Because there are more unknown factors that affect the retrieval of C from ocean colour than there are unknown factors that affect the retrieval of absorption and backscattering coefficients, we should revisit the issue of C remaining the primary product of ocean-colour remote sensing, rather than the IOPs of the bulk water or the optical properties of phytoplankton.

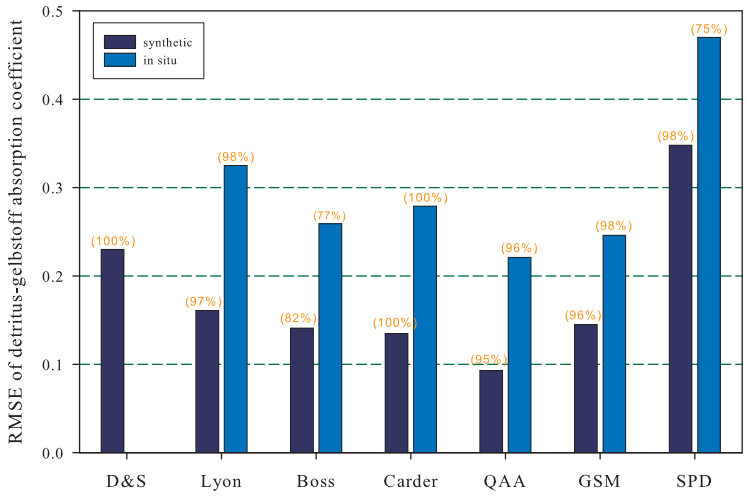

Figure 14.3 As in Figure 14.1, but for absorption coefficient of detritus and gelbstoff combined.

6. The robust and stable results of the total absorption and backscattering coefficients from these various algorithms (again using the synthetic data set as reference), which were developed independently and are based on different principles, clearly indicate that these optical properties should be taken as standard products for all ocean-colour satellite missions. These optical properties, similar to the sea surface temperature, could serve as climatology data records to study long-term changes of the global oceans.
7. Space-based sensors should be equipped with at least one spectral band in the region of 620-640 nm. Such a band is very important for coastal remote sensing (or for more turbid waters), and algorithm performance would be improved when such a band is included in the process.
8. Algorithms based on the fundamentals of hydrological optics are strongly advocated. Simple empirical relationships prevent understanding of the basics and, therefore, limit advancement in ocean-colour remote sensing. On the other hand, analytical or semi-analytical algorithms enable opportunities to trace back the error sources.

Because inherent optical properties provide important indices for our water environments and open new doors for oceanographic studies, we should spend a great deal of effort on the following issues to improve IOP products:

- Increased high-quality, co-located measurements of remote-sensing reflectance and IOPs.
- Improved methods to select model parameters such as the spectral shapes of individual IOPs that include $b_b(\lambda)$, $a_{ph}(\lambda)$ and $a_{dg}(\lambda)$. Separation of the global ocean into dynamic biogeochemical provinces may provide vital help in this regard (see IOCCG working group on “Global Ecological Provinces"

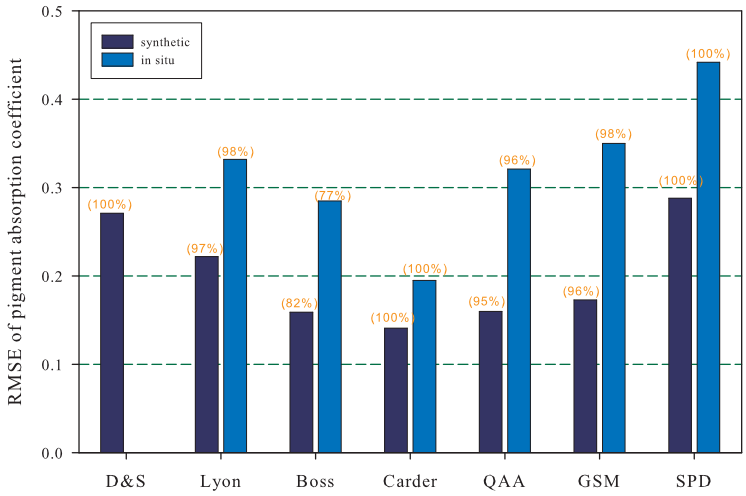

Figure 14.4 As in Figure 14.1, but for the absorption coefficient of phytoplankton pigments.

`http://www.ioccg.org/groups/dowell.html` for more information).

- Better quantification of uncertainties in derived products. An in-depth analysis of error sources and their propagation are highly desirable in this regard.
- Improved procedure for atmospheric correction. All algorithms tested use remote-sensing reflectance (R_{rs}) as inputs for the calculation of IOPs. Quality of R_{rs}, which is one of the products derived from atmospheric correction, plays a critical role in the accuracy of retrieved IOPs. Addition of UV-a bands would assist in the derivation of R_{rs} from satellite measured radiance, especially for coastal waters. Also, such bands may increase the ability to separate phytoplankton absorption from that of dissolved and non-pigmented particulate materials.
- And, finally, enhance and broaden applications of IOPs for oceanographic studies, which are the ultimate goal of ocean-colour remote sensing.

It should be pointed out that in this exercise, the water column was assumed to be homogeneous in terms of its optical properties. Passive optical remote sensing becomes quite a challenge when the optical properties of the upper water column are significantly stratified. Furthermore, we did not touch on issues related to optically shallow environments in this report (for discussions on this issue see IOCCG Report 3). To resolve these important issues, we need to effectively combine measurements from satellite with those from other observatory platforms, such as LIDAR, gliders, and the Network of Coastal Observatories.

References

Åas, E., and Højerslev, N.K. (1999). Analysis of underwater radiance observations: Apparent optical properties and analytic functions describing the angular radiance distribution. J. Geophys. Res. 104: 8015-8024.

Aires, F., Prigent, C., and Rossow, W.B. (2004). Neural network uncertainty assessment using Bayesian statistics: A remote sensing application. Neural Computation 16: 2415-2458.

Allali, K., Bricaud, A., Babin, M., Morel, A., and Chang, P. (1995). A new method for measuring spectral absorption coefficients of marine particles. Limnol. Oceanogr. 40: 1526-1532.

Arnone, R.A., and Parsons, A.R. (2004). Real-time use of ocean color remote sensing for coastal monitoring. In: Remote Sensing of the Coastal Environments. Miller, R.L., DelCastillo, C.E., and McKee, B.A. (eds). Kluwer academic, Dordrecht, The Netherlands.

Arnone, R.A., Wood, A.M., and Gould, R.W. (2004). The evolution of optical water mass classification. Oceanogr. 17: 14-15.

Balch, W.M., Gordon, H.R., Bowler, B.C., Drapeau, D.T., and Booth, E.S. (2005). Calcium carbonate measurements in the surface global ocean based on Moderate-Resolution Imaging Spectroradiometer data. J. Geophys. Res. 110: doi:10.1029/2004JC002560.

Barnard, A.H., Zaneveld, J.R., and Pegau, W.S. (1999). *In situ* determination of the remotely sensed reflectance and the absorption coefficient: closure and inversion. Appl. Opt. 38: 5108-5117.

Bates, D.M., and Watts, D.G. (1988). Nonlinear regression analysis and its applications. Wiley, New York, p. 384.

Behrenfeld, M.J., and Falkowski, P.G. (1997). A consumer's guide to phytoplankton primary productivity models. Limnol. Oceanogr. 42: 1479-1491.

Behrenfeld, M.J., Boss, E., Siegel, D., and Shea, D.M. (2005). Carbon-based ocean productivity and phytoplankton physiology from space. Global Biogeochem. Cycles 19: GB1006, doi:1010.1029/2004GB002299.

Berwald, J., Stramski, D., Mobley, C.D., and Kiefer, D.A. (1995). Influences of absorption and scattering on vertical changes in the average cosine of the underwater light field. Limnol. Oceanogr. 40: 1347-1357.

Bissett, W.P., Arnone, R., DeBra, S., Dieterle, D.A., Dye, D., Kirkpatrick, G.J. *et al.* (2005). Predicting the optical properties of the West Florida Shelf: resolving

the potential impacts of a terrestrial boundary condition on the distribution of colored dissolved and particulate matter. Mar. Chem. 95: 199-233.

Bissett, W.P., Schofied, O., Glenn, S., Cullen, J.J., Miller, W.L., Plueddemann, A.J., and Mobley, C.D. (2001). Resolving the impacts and feedback of ocean optics on upper ocean ecology. Oceanogr. 14: 30-53.

Boss, E., and Pegau, W.S. (2001). The relationship of light scattering at an angle in the backward direction to the backscattering coefficient. Appl. Opt. 40: 5503-5507.

Bricaud, A., and Morel, A. (1986). Light attenuation and scattering by phytoplanktonic cells: a theoretical modeling. Appl. Opt. 25: 571-580.

Bricaud, A., and Stramski, D. (1990). Spectral absorption coefficients of living phytoplankton and nonalgal biogenous matter: A comparison between the Peru upwelling area and the Sargasso Sea. Limnol. Oceanogr. 35: 562-582.

Bricaud, A., Morel, A., and Prieur, L. (1981). Absorption by dissolved organic matter of the sea (yellow substance) in the UV and visible domains. Limnol. Oceanogr. 26: 43-53.

Bricaud, A., Babin, M., Morel, A., and Claustre, H. (1995). Variability in the chlorophyll-specific absorption coefficients of natural phytoplankton: Analysis and parameterization. J. Geophys. Res. 100: 13321-13332.

Bricaud, A., Claustre, H., Ras, J., and Oubelkheir, K. (2004). Natural variability of phytoplanktonic absorption in oceanic waters: Influence of the size structure of algal populations. J. Geophys. Res. 109: doi:10.1029/2004JC002419.

Bricaud, A., Morel, A., Babin, M., Allali, K., and Claustre, H. (1998). Variations of light absorption by suspended particles with chlorophyll a concentration in oceanic (case 1) waters: Analysis and implications for bio-optical models. J. Geophys. Res. 103: 31033-31044.

Bukata, R.P., Jerome, J.H., Kondratyev, K.Y., and Pozdnyakov, D.V. (1995). Optical Properties and Remote Sensing of Inland and Coastal Waters. CRC Press, Boca Raton, FL.

Burenkov, V.I., Verdernikov, V.I., Ershova, S.V., Kopelevitch, O.V., and Sheberstov, S.V. (2001). Use of satellite ocean color data for assessment of bio-optical characteristics in the Barent Sea. Okeanologiya 41: 485-492.

Cannizzaro, J.P., Carder, K.L., Chen, F.R., Heil, C.A., and Vargo, G.A. (2006). A novel technique for detection of the toxic dinoflagellate, *Karenia brevis*, in the Gulf of Mexico from remotely sensed ocean color data. Cont. Shelf Res. Accepted.

Carder, K.L., Steward, R.G., Harvey, G.R., and Ortner, P.B. (1989). Marine humic and fulvic acids: their effects on remote sensing of ocean chlorophyll. Limnol. Oceanogr. 34: 68-81.

Carder, K.L., Hawes, S.K., Baker, K.A., Smith, R.C., Steward, R.G., and Mitchell, B.G. (1991). Reflectance model for quantifying chlorophyll a in the presence of

productivity degradation products. J. Geophys. Res. 96: 20599-20611.

Carder, K.L., Chen, F.R., Lee, Z.P., Hawes, S.K., and Kamykowski, D. (1999). Semianalytic Moderate-Resolution Imaging Spectrometer algorithms for chlorophyll-a and absorption with bio-optical domains based on nitrate-depletion temperatures. J. Geophys. Res. 104: 5403-5421.

Carder, K.L., Chen, F.R., Cannizzaro, J.P., Campbell, J.W., and Mitchell, B.G. (2004). Performance of the MODIS semi-analytical ocean color algorithm for chlorophyll-a. Adv. Space Res. 33: 1152-1159.

Chandrasekhar, S. (1960). Radiative Transfer. Dover Publications, Inc., New York, p. 393.

Ciotti, A.M., Lewis, M.R., and Cullen, J.J. (2002). Assessment of the relationships between domininant cell size in natural phytoplankton communities and spectral shape of the absorption coefficient. Limnol. Oceanogr. 47: 404-417.

Claustre, H., and Maritorena, S. (2003). The many shades of ocean blue. Science 302: 1514-1515.

Claustre, H., Hooker, S.B., Heukelem, L.V., Berthon, J.F., Barlow, R., Ras, J. *et al.* (2004). An intercomparison of HPLC phytoplankton methods using *in situ* samples: Application to remote sensing and database activities. Mar. Chem. 85: 41-61.

Cleveland, J.S. (1995). Regional models for phytoplankton absorption as a function of chlorophyll a concentration. J. Geophys. Res. 100: 13,333-13,344.

Cleveland, J. S., and Weidemann, A. D. (1993). Quantifying absorption by aquatic particles: A multiple scattering correction for glass-fiber filters. Limnol. Oceanogr. 38: 1321-1327.

Coble, P., Hu, C., Gould, R., Chang, G., and Wood, A.M. (2004). Colored dissolved organic matter in the coastal ocean: An optical tool for coastal environmental assessment and management. Oceanogr. 17: 50-59.

Cullen, J.J., Ciotti, A.M., Davis, R.F., and Lewis, M.R. (1997). Optical detection and assessment of algal blooms. Limnol. Oceanogr.: 1223-1239.

Devred, E., Sathyendranath, S., Stuart, V., Maass, H., Ulloa, O., and Platt, T. (2006). A two-component model of phytoplankton absorption in the open ocean: theory and applications. J. Geophys. Res. 111: doi:10.1029/2005JC002880, 2006.

Devred, E., Fuentes-Yaco, C., Sathyendranath, S., Caverhill, C., Maass, H., Stuart, V. *et al.* (2005). A semi-analytic, seasonal algorithm to retrieve chlorophyll-a concentration in the northwest Atlantic from SeaWiFS data. Indian J. Mar. Sci. 34: 356-367.

Doerffer, R., and Schiller, H. (2000). Neural Network for retrieval of concentrations of water constituents with the possibility of detecting exceptional out of scope spectra. In: IEEE 2000 International Geoscience and Remote Sensing Symposium, Honolulu, Hawaii USA, p. 714-717.

Doerffer, R., and Schiller, H. (2006). The MERIS case 2 water algorithm. Int. J. Remote Sens. In press.

Doerffer, R., Heymann, K., and Schiller, H. (2002). Case 2 water algorithm for the medium resolution imaging spectrometer (MERIS) on ENVISAT. In: Proceedings of the ENVISAT validation workshop, 9-13 December 2002, ESA report.

Dupouy, C., Loisel, H., Neveux, J., Moulin, C., Brown, S., Blanchot, J. *et al.* (2003). Microbial absorption and backscattering coefficients from *in situ* and POLDER satellite during an El Nino-Southern Oscillation cold phase in the equatorial Pacific (180°). J. Geophys. Res. 108: 8138.

Fischer, J., and Fell, F. (1999). Simulation of MERIS measurements above selected ocean waters. Int. J. Remote Sensing 20: 1787-1807.

Garver, S.A., and Siegel, D. (1997). Inherent optical property inversion of ocean color spectra and its biogeochemical interpretation 1. Time series from the Sargasso Sea. J. Geophys. Res. 102: 18607-18625.

Gohin, F., Druon, J.N., and Lampert, L. (2002). A five channel chlorophyll concentration algorithm applied to SeaWiFS data processed by SeaDAS in coastal waters. Int. J. Remote Sens. 23: 1639-1661.

Gordon, H.R. (1989). Can the Lambert-Beer law be applied to the diffuse attenuation coefficient of ocean water? Limnol. Oceanogr. 34: 1389-1409.

Gordon, H.R. (2002). Inverse Methods in hydrologic optics. Oceanologia 44: 9-58.

Gordon, H.R., and Clark, D.K. (1980). Remote sensing optical properties of a stratified ocean: an improved interpretation. Appl. Opt. 19: 3428-3430.

Gordon, H.R., and Morel, A. (1983). Remote assessment of ocean color for interpretation of satellite visible imagery: A review. Springer-Verlag, New York.

Gordon, H.R., Brown, O.B., and Jacobs, M.M. (1975). Computed relationship between the inherent and apparent optical properties of a flat homogeneous ocean. Appl. Opt. 14: 417-427.

Gordon, H.R., Brown, O.B., Evans, R.H., Brown, J.W., Smith, R.C., Baker, K.S., and Clark, D.K. (1988). A semianalytic radiance model of ocean color. J. Geophys. Res. 93: 10,909-10,924.

Gould, R.W., and Arnone, R. (1997). Remote sensing estimates of inherent optical properties in a coastal environment. Remote Sens. Environ. 61: 290-301.

Gould, R.W., and Arnone, R.A. (2003). Optical water mass classification for ocean color imagery. In: Second International Conference, Current Problems in Optics Of Natural Waters. St. Petersburg, Russia.

Gregg, W.W., and Carder, K.L. (1990). A simple spectral solar irradiance model for cloudless maritime atmospheres. Limnol. Oceanogr. 35: 1657-1675.

Haltrin, V.I. (1999). Chlorophyll-based model of seawater optical properties. Appl. Opt. 38: 6826-6832.

Hoepffner, N., and Sathyendranath, S. (1991). Effect of pigment composition on absorption properties of phytoplankton. Mar. Ecol. Prog. Ser. 73: 11-23.

Hoepffner, N., and Sathyendranath, S. (1992). Bio-optical characteristics of coastal waters: Absorption spectra of phytoplankton and pigment distribution in the western North Atlantic. Limnol. Oceanogr. 37: 1660-1679.

Hoge, F.E., and Lyon, P.E. (1996). Satellite retrieval of inherent optical properties by linear matrix inversion of oceanic radiance models: an analysis of model and radiance measurement errors. J. Geophys. Res. 101: 16631-16648.

Hoge, F.E., and Lyon, P.E. (1999). Spectral parameters of inherent optical property models: Methods for satellite retrieval by matrix inversion of an oceanic radiance model. Appl. Opt. 38: 1657-1662.

Hoge, F.E., Wright, C.W., Lyon, P.E., Swift, R.N., and Yungel, J.K. (2001). Inherent optical properties imagery of the western North Atlantic Ocean: Horizontal spatial variability of the upper mixed layer. J. Geophys. Res. 106: 31,129-31,140.

Hooker, S.B., and Maritorena, S. (2000). An evaluation of oceanographic radiometers and deployment methodologies. J. Atmos. Ocean. Tech. 17: 811-830.

Hooker, S.B., Esaias, W.E., Feldman, G.C., Gregg, W.W., and McClain, C.R. (1992). An overview of SeaWiFS and Ocean Color. SeaWiFS technical report series. Volume 1, Hooker, S.B., and Firestone, E.R. (eds), NASA Goddard Space Flight Center, Greenbelt, MD, p. 24.

Hooker, S.B., McClain, C.R., Firestone, J.K., Westphal, T.L., Yeh, E.-N., and Ge, Y. (1994). The SeaWiFS Bio-Optical Archive and Storage System (SeaBASS), Part 1. In: NASA Tech. Memo. 104566. Hooker, S.B., and Firestone, E.R. (eds). NASA Goddard Space Flight Center, Greenbelt, Maryland, p. 1-40.

Hooker, S.B., Zibordi, G., Berthon, J.-F., D'Alimonte, D., Maritorena, S., McLean, S., and Sildam, J. (eds) (2001). Results of the second SeaWiFS data analysis round robin. NASA Goddard Space Flight Center, Greenbelt, Maryland.

Hu, C., Lee, Z., Muller-Karger, F.E., Carder, K.L., and Walsh, J.J. (2006). Ocean color reveals phase shift between marine plants and yellow substance. IEEE Geosci. Remote Sens. Lett. 3(2): 262-266.

Hu, C., Chen, Z., Clayton, T.D., Swarzenski, P., Brock, J.C., and Müller-Karger, F.E. (2004). Assessment of estuarine water-quality indicators using MODIS medium-resolution bands: Initial results from Tampa Bay, Florida. Remote Sens. Environ. 93: 423-441.

Hu, C., Muller-Karger, F.E., Biggs, D.C., Carder, K.L., Nababan, B., Nadeau, D., and Vanderbloemen, J. (2003). Comparison of ship and satellite bio-optical measurements on the continental margin of the NE Gulf of Mexico. Int. J. Remote Sens. 24: 2597-2612.

Kamykowski, D. (1987). A preliminary biophysical model of the relationship between temperature and plant nutrients in the upper ocean. Deep-Sea Res. 34: 1067-1079.

Kamykowski, D., and Zentara, S. (1986). Predicting plant nutrient concentrations from temperature and sigma-t in the upper kilometer of the world ocean. Deep-Sea Res. 33: 89-105.

Kirk, J.T.O. (1984). Dependence of relationship between inherent and apparent optical properties of water on solar altitude. Limnol. Oceanogr. 29: 350-356.

Kirk, J.T.O. (1994). Light and Photosynthesis in Aquatic Ecosystems. University Press, Cambridge.

Kopelevich, O.V., and Burenkov, V.I. (1977). Relation between the spectral values of the light absorption coefficients of sea water, phytoplanktonic pigments, and the yellow substance. Oceanology 17: 278-282.

Krasnopolsky, V., and Schiller, H. (2003). Some Neural Network applications in environmental sciences. Part I: Forward and inverse problems in geophysical remote measurements. Neural Networks 16: 321-334.

Laws, E.A. (1997). Mathematical methods for oceanographers: An introduction. John Wiley and Sons, New York.

Lee, Z.P. and Hu, C. (2006). Global distribution of Case-1 waters: An analysis from SeaWiFS measurements. Remote Sens. Env. 101: 270-276.

Lee, Z.P., Carder, K.L., and Arnone, R. (2002). Deriving inherent optical properties from water color: A multi-band quasi-analytical algorithm for optically deep waters. Appl. Opt. 41: 5755-5772.

Lee, Z.P., Carder, K.L., and Du, K.P. (2004). Effects of molecular and particle scatterings on model parameters for remote-sensing reflectance. Appl. Opt. 43: 4957-4964.

Lee, Z.P., Carder, K.L., Steward, R.G., and Perry, M.J. (1996a). Estimating primary production at depth from remote sensing. Appl. Opt. 35: 463-474.

Lee, Z.P., Carder, K.L., Peacock, T.G., Davis, C.O., and Mueller, J.L. (1996b). Method to derive ocean absorption coefficients from remote-sensing reflectance. Appl. Opt. 35: 453-462.

Lee, Z.P., Carder, K.L., Mobley, C.D., Steward, R.G., and Patch, J.S. (1998a). Hyperspectral remote sensing for shallow waters. 1. A semianalytical model. Appl. Opt. 37: 6329-6338.

Lee, Z.P., Carder, K.L., Steward, R.G., Peacock, T.G., Davis, C.O., and Patch, J.S. (1998b). An empirical algorithm for light absorption by ocean water based on color. J. Geophys. Res. 103: 27967-27978.

Lee, Z.P., Carder, K.L., Mobley, C.D., Steward, R.G., and Patch, J.S. (1999). Hyperspectral remote sensing for shallow waters: 2. Deriving bottom depths and water properties by optimization. Appl. Opt. 38: 3831-3843.

Lee, Z.P., Du, K., Arnone, R., Liew, S.C., and Penta, B. (2005a). Penetration of solar radiation in the upper ocean - A numerical model for oceanic and coastal waters. J. Geophys. Res. 110: C09019, doi:09010.01029/02004JC002780.

Lee, Z.P., Darecki, M., Carder, K.L., Davis, C., Stramski, D., and Rhea, W.J. (2005b). Diffuse attenuation coefficient of downwelling irradiance: An evaluation of remote sensing methods. J. Geophys. Res. 110: doi:10.1029/2004JC002573.

Loisel, H., and Morel, A. (1998). Light scattering and chlorophyll concentration in Case 1 waters: A reexamination. Limnol. Oceanogr. 43: 847-858.

Loisel, H., and Stramski, D. (2000). Estimation of the inherent optical properties of natural waters from the irradiance attenuation coefficient and reflectance in the presence of Raman scattering. Appl. Opt. 39: 3001-3011.

Loisel, H., and Morel, A. (2001). Non-isotropy of the upward radiance field in typical coastal (Case 2) waters. Int. J. Remote Sens. 22: 275-295.

Loisel, H., Nicolas, J.M., Deschamps, P.Y., and Frouin, R. (2002). Seasonal and inter-annual variability of the particulate matter in the global ocean. Geophys. Res. Lett. 29: 2196, doi:2110.1029/2002GL015948.

Loisel, H., Bosc, E., Stramski, D., Oubelker, K., and Deschamps, P.Y. (2001a). Seasonal variability of the backscattering coefficients in the Mediterranean Sea based on Satellite SeaWIFS imagery. Geophys. Res. Lett. 28: 4203-4206.

Loisel, H., Stramski, D., Mitchell, B.G., Fell, F., Fournier-Sicre, V., Lemasle, B., and Babin, M. (2001b). Comparison of the ocean inherent optical properties obtained from measurements and inverse modeling. Appl. Opt. 40: 2384-2397.

Lutz, V.A., Sathyendranath, S., and Head, E.J.H. (1996). Absorption coefficient of phytoplankton: Regional variations in the North Atlantic. Mar. Ecol. Prog. Ser. 135: 197-213.

Lyon, P.E., Hoge, F.E., Wright, C.W., Swift, R.N., and Yungel, J.K. (2004). Chlorophyll biomass in the global oceans: Satellite retrieval using inherent optical properties. Appl. Opt. 43: 5886-5892.

Maritorena, S., and Siegel, D.A. (2005). Consistent merging of satellite ocean color data sets using a bio-optical model. Remote Sens. Environ. 94: 429-440.

Maritorena, S., Siegel, D.A., and Peterson, A.R. (2002). Optimization of a semi-analytical ocean color model for global-scale applications. Appl. Opt. 41: 2705-2714.

McClain, C.R., Barnes, R.A., R.E. Eplee, J., Franz, B.A., Hsu, N.C., Patt, F.S. *et al.* (2000). SeaWiFS Postlaunch Calibration and Validation Analyses, Part 2. NASA Goddard Space Flight Center, Greenbelt, Maryland.

Melin, F., G., Z., and Berthon, J.F. (2002). Comparison of *in situ* and SeaWiFS derived atmospheric and marine products for the Adriatic Sea. In: Proc. Ocean Optics XVI, Santa Fe, New Mexico. Ackleson, S. (ed), Office of Naval Research, Fremantle, USA.

Mitchell, G., Bricaud, A., Carder, K.L., Cleveland, J., Ferrari, G., Gould, R. *et al.* (2000). Determination of spectral absorption coefficients of particles, dis-

solved material, and phytoplankton for discrete water samples. In: Ocean Optics Protocols for Satellite Ocean Color Sensor Validation, Revision 2, NASA/TM 2000-209966, Fargion, G.S. and Mueller, J.L. (eds.) NASA Goddard Space Flight Center, Greenbelt, Maryland. p. 125– 153.

Mitchell, B. G., and Kiefer, D. A. (1988). Variability in pigment specific particulate fluorescence and absorption spectra in the northeastern Pacific Ocean. Deep-Sea Res. I. 35: 665-689.

Mobley, C.D. (1994). Light and Water: radiative transfer in natural waters. Academic Press, New York.

Mobley, C.D. (1995). Hydrolight 3.0 Users' Guide. SRI International, Menlo Park, California.

Mobley, C.D., Gentili, B., Gordon, H.R., Jin, Z., Kattawar, G.W., Morel, A. *et al.* (1993). Comparison of numerical models for computing underwater light fields. Appl. Opt. 32: 7484-7504.

Mobley, C. D., Stramski, D., Bissett, W.P. and Boss, E. (2004). Optical modeling of ocean waters: Is the Case 1 - Case 2 classification still useful? Oceanography, 17(2): 60-67.

Morel, A. (1974). Optical properties of pure water and pure sea water. In: Optical Aspects of Oceanography. Jerlov, N.G., and Nielsen, E. S. (eds). Academic Press, New York, p. 1-24.

Morel, A. (1978). Available, usable, and stored radiant energy in relation to marine photosynthesis. Deep-Sea Res 25: 673-688.

Morel, A. (1988). Optical modeling of the upper ocean in relation to its biogenous matter content (Case I waters). J. Geophys. Res. 93: 10749-10768.

Morel, A., and Prieur, L. (1977). Analysis of variations in ocean color. Limnol. Oceanogr. 22: 709-722.

Morel, A., and Gentili, B. (1993). Diffuse reflectance of oceanic waters II: Bidirectional aspects. Appl. Opt. 32: 6864-6879.

Morel, A., and Antoine, D. (1994). Heating rate within the upper ocean in relation to its bio-optical state. J. Physical Oceanogr. 24: 1652-1665.

Morel, A., and Gentili, B. (1996). Diffuse reflectance of oceanic waters, III: Implications of bi-directionality for the remote sensing problem. Appl. Opt. 35: 4850-4862.

Morel, A., and Maritorena, S. (2001). Bio-optical properties of oceanic waters: A reappraisal. J. Geophys. Res. 106: 7163-7180.

Morel, A., Antoine, D., Babin, M., and Dandonneau, Y. (1996). Measured and modeled primary production in the northeast Atlantic (EUMELI JGOFS program): the impact of natural variations in photosynthetic parameters on model predictive skill. Deep-Sea Res. I. 43: 1273-1304.

Mueller, J.L. (2000). SeaWiFS algorithm for the diffuse attenuation coefficient, K(490), using water-leaving radiances at 490 and 555 nm. In SeaWiFS Postlaunch Calibration and Validation Analyses, Part 3. Hooker, S.B. (ed), NASA

Goddard Space Flight Center, Greenbelt,Maryland, pp. 24-27.

Mueller, J.L., and Austin, R.W. (eds.) (1992). Ocean optics protocols for SeaWiFS validation. NASA Tech. Memo. 104566, Vol. 5, SeaWiFS Tech. Report Series, NASA Goddard Space Flight Center, Greenbelt, Maryland, 45 pp.

Mueller, J.L., and Austin, R.W. (eds) (1995). Ocean Optics Protocols for SeaWiFS Validation, Revision 1. NASA Tech. Memo. 104566, Vol. 25, SeaWiFS Tech. Report Series, Goddard Space Flight Center, Greenbelt, Maryland, 67 pp.

Mueller, J.L., Davis, C., Arnone, R., Frouin, R., Carder, K.L., Lee, Z.P. *et al.* (2002). Above-water radiance and remote sensing reflectance measurement and analysis protocols. In: Ocean Optics Protocols for Satellite Ocean Color Sensor Validation, Revision 3, NASA/TM-2002-210004, NASA Goddard Space Flight Center, Greenbelt, Maryland. Mueller, J.L., and Fargion, G.S. (eds), pp. 171-182.

Nelson, N.B., and Siegel, D.A. (2002). Chromophoric DOM in the open ocean. In: Biogeochemistry of Marine Dissolved Organic Matter. Hansell, D.A., and Carlson, C.A. (eds), Academic Press, San Diego, p. 774.

Nelson, N.B., Siegel, D.A., and Michaels, A.F. (1998). Seasonal dynamics of colored dissolved material in the Sargasso Sea. Deep-Sea Res. 45: 931-957.

Ohlmann, J.C., and Siegel, D. (2000). Ocean Radiant Heating. Part II: Parameterizing solar radiation transmission through the upper ocean. J. Phys. Oceanogr. 30: 1849-1865.

O'Reilly, J., Maritorena, S., Mitchell, B.G., Siegel, D., Carder, K.L., Garver, S. *et al.* (1998). Ocean color chlorophyll algorithms for SeaWiFS. J. Geophys. Res. 103: 24937-24953.

Otero, M.P., and Siegel, D.A. (1995). Spatial and temporal characteristics of sediment plumes and phytoplankton blooms in the Santa Barbara Channel. Deep-Sea Res. 100: 13279-13294.

Pegau, W.S., Gray, D., and Zaneveld, J.R.V. (1997). Absorption and attenuation of visible and near-infrared light in water: dependence on temperature and salinity. Appl. Opt. 36: 6035-6046.

Penta, B., Kindle, J., Shulman, I., deRada, S., Anderson, S., Lee, Z.P. *et al.* (2005). Remote sensing in conjunction with the Navy Coastal Ocean Model (NCOM): examples from the California current system. In: Eighth International Conference on Remote Sensing for Marine and Coastal Environments, Halifax, Nova Scotia.

Platt, T., and Sathyendranath, S. (1988). Oceanic primary production: estimation by remote sensing at local and regional scales. Science 241: 1613-1620.

Pope, R., and Fry, E. (1997). Absorption spectrum (380 - 700 nm) of pure waters: II. Integrating cavity measurements. Appl. Opt. 36: 8710-8723.

Preisendorfer, R.W. (1976). Hydrologic optics, Vol. 1: Introduction. Springfield: National Technical Information Service. Also available on CD, Office of Naval Research.

Press, W.H. (1992). Numerical Recipes in FORTRAN: The Art of Scientific Computing, 2nd ed., Cambridge University Press, New York.

Press, W.H., Teukolsky, S.A., Vetterling, W.T., and Flannerty, B.P. (1992). Numerical Recipes in C: The Art of Scientific Computing, 2nd Edition. Cambridge University Press, New York.

Prieur, L., and Sathyendranath, S. (1981). An optical classification of coastal and oceanic waters based on the specific spectral absorption curves of phytoplankton pigments, dissolved organic matter, and other particulate materials. Limnol. Oceanogr. 26: 671-689.

Reynolds, R.A., Stramski, D., and Mitchell, B.G. (2001). A chlorophyll-dependent semianalytical reflectance model derived from field measurements of absorption and backscattering coefficients within the Southern Ocean. J. Geophys. Res. 106: 7125-7138.

Roesler, C.S., and Perry, M.J. (1995). *In situ* phytoplankton absorption, fluorescence emission, and particulate backscattering spectra determined from reflectance. J. Geophys. Res. 100: 13279-13294.

Roesler, C.S., and Boss, E. (2003). Spectral beam attenuation coefficient retrieved from ocean color inversion. Geophys. Res. Lett. 30: 1468.

Roesler, C.S., Perry, M.J., and Carder, K.L. (1989). Modeling *in situ* phytoplankton absorption from total absorption spectra in productive inland marine waters. Limnol. Oceanogr. 34: 1510-1523.

Sathyendranath, S., and Platt, T. (1988). The spectral irradiance field at the surface and in the interior of the ocean: a model for applications in oceanography and remote sensing. J. Geophys. Res. 93: 9270-9280.

Sathyendranath, S., and Platt, T. (1989). Remote sensing of ocean chlorophyll: consequence of nonuniform pigment profile. Appl. Opt. 28: 490-495.

Sathyendranath, S., and Platt, T. (1997). Analytic model of ocean color. Appl. Opt. 36: 2620-2629.

Sathyendranath, S., and Platt, T. (1998). Ocean-color model incorporating transspectral processes. Appl. Opt. 37: 2216-2227.

Sathyendranath, S., Cota, G., Stuart, V., Maass, M., and Platt, T. (2001). Remote sensing of phytoplankton pigments: a comparison of empirical and theoretical approaches. Int. J. Remote Sens. 22: 249-273.

Sathyendranath, S., Platt, T., Irwin, B., Horne, E., Borstad, G., Stuart, V. *et al.* (2004). A multispectral remote sensing study of coastal waters off Vancouver Island. Int. J. Remote Sens. 24: 893-919.

Schiller, H., and Doerffer, R. (2005). Improved determination of coastal water constituent concentrations from MERIS data. IEEE Trans. Geosci. Remote Sens. 43: 1585-1591.

SeaWiFS (2000). Ocean color algorithm evaluation. URL http://seawifs.gsfc.nasa.gov/SEAWIFS/RECAL/Repro3/OC4_reprocess.html.

Shifrin, K. (1988). Physical optics of ocean water. American Institute of Physics, New York.

Shulman, I., Kindle, J.C., deRada, S., Anderson, S.C., Penta, B., and Martin, P.J. (2004). Development of a hierarchy of nested models to study the California current system. In: Estuarine and Coastal Modeling 2003, 8th International Conference on Estuarine and Coastal Modeling, Spaulding, M.L. (ed.) November 3–5, 2003, Monterey, California, pp. 74-88.

Siegel,D. A., Maritorena, S., Nelson, N. B., Hansell, D. A. and Lorenzi-Kayser, M. (2002). Global distribution and dynamics of colored dissolved and detrital organic materials. J. Geophys. Res. 107: 3228, doi:10.1029/2001JC000965.

Siegel, D.A., O'Brien, M.C., Sorensen, J.C., Konnoff, D.A., Brody, E.A., Mueller, J.L. *et al.* (eds) (1995). Results of the SeaWiFS Data Analysis Round-Robin (DARR-94). NASA Goddard Space Flight Center, Greenbelt, Maryland.

Smith, R.C., and Baker, K.S. (1981). Optical properties of the clearest natural waters. Appl. Opt. 20: 177-184.

Smith, R.C., Prezelin, B.B., Bidigare, R.R., and Baker, K.S. (1989). Bio-optical modeling of photosynthetic production in coastal waters. Limnol. Oceanogr. 34: 1524-1544.

Smyth, T.J., Groom, S.B., Cummings, D.G., and Llewellyn, C.A. (2002). Comparison of SeaWiFS bio-optical chlorophyll-a algorithms within the OMEXII programme. Int. J. Remote Sens. 23: 2321-2326.

Sokal, R.R., and Rohlf, F.J. (1981). Biometry. W.H. Freeman, New York.

Stramski, D., Bricaud, A., and Morel, A. (2001). Modeling the inherent optical properties of the ocean based on the detailed composition of the planktonic community. Appl. Opt. 40: 2929-2945.

Stramski, D., Reynolds, R.A., Kahru, M., and Mitchell, B.G. (1999). Estimation of particulate organic carbon in the ocean from satellite remote sensing. Science 285: 239-242.

Stuart, V., Sathyendranath, S., Platt, T., Maass, H., and Irwin, B. (1998). Pigments and species composition of natural phytoplankton populations: effect on the absorption spectra. J. Plankton Res. 20: 187-217.

Thomas, G.E., and Stamnes, K. (1999). Radiative Transfer in the Atmosphere and Ocean. Cambridge University Press, Cambridge, UK.

Traykovski, L.V.M., and Sosik, H.M. (2003). Feature-based classification of optical water types in the Northwest Atlantic based on satellite ocean color data. J. Geophys. Res. 108(C5): 3150, doi:10.1029/2001JC001172, 2003.

Twardowski, M.J., Lewis, M.R., Barnard, A., and Zaneveld, J.R.V. (2005). In-water instrumentation and platforms for ocean color remote sensing applications. In: Remote sensing of Coastal Aquatic Environments. Miller, R.L., Castillo, C.E.D., and McKee, B.A. (eds). Springer, Dordrecht, 347 pp.

Ulloa, O., Sathyendranath, S., and Platt, T. (1994). Effect of the particle-size distribution on the backscattering ratio in seawater. Appl. Opt. 30: 7070-

7077.

van de Hulst, H.C. (1981). Light Scattering By Small Particles. Dover, New York.

Van Heukelem, L., Thomas, C.S., and Glibert, P.M. (eds) (2002). Sources of variability in chlorophyll analysis by fluorometry and high performance liquid chromatography in a SIMBIOS inter-calibration exercise. NASA Goddard Space Flight Center, Greenbelt, Maryland.

Wang, P., Boss, E., and Roesler, C. (2005). Uncertainties of inherent optical properties obtained from semi-analytical inversions of ocean color. Appl. Opt. 44: 4074-4085.

Westberry, T.K., Siegel, D.A., and Subramaniam, A. (2005). An improved bio-optical model for the remote sensing of *Trichodesmium* spp. blooms. J. Geophys. Res. 110: C06012, doi:06010.01029/02004JC002517.

Yoder, J.A., Moore, J.K., and Swift, R.N. (2001). Putting together the big picture: Remote-sensing observations of ocean color. Oceanogr. 14: 33-40.

Zaneveld, J.R.V. (1973). New developments of the theory of radiative transfer in the ocean. In: Optical Aspects of Oceanography. Jerlov, N.G. (ed). Academic Press, London, p. 121-134.

Zaneveld, J.R.V. (1982). Remote sensed reflectance and its dependence on vertical structure: a theoretical derivation. Appl. Opt. 21: 4146-4150.

Zaneveld, J.R.V. (1989). An asymptotic closure theory for irradiance in the sea and its inversion to obtain the inherent optical properties. Limnol. Oceanogr. 34: 1442-1452.

Zaneveld, J.R.V. (1995). A theoretical derivation of the dependence of the remotely sensed reflectance of the ocean on the inherent optical properties. J. Geophys. Res. 100: 13135-13142.

Zaneveld, J.R.V., Kitchen, J.C., and Mueller, J.L. (1993). Vertical structure of productivity and its vertical integration as derived from remotely sensed observations. Limnol. Oceanogr. 38: 1384-1393.

Zaneveld, J.R.V., Barnard, A.H., and Boss, E. (2005a). Theoretical derivation of the depth average of remotely sensed optical parameters. Opt. Express 13: 9052-9061.

Zaneveld, J.R.V., Twardowski, M.J., Barnard, A., and Lewis, M.R. (2005b). Introduction to radiative transfer. In: Remote sensing of Coastal Aquatic Environments. Miller, R.L., Castillo, C.E.D., and McKee, B.A. (eds).Springer, Dordrecht, p. 347.

Acronyms and Abbreviations

aNN	Artificial Neural Network
AOP	Apparent Optical Property
AVHRR	Advanced Very High Resolution Radiometer
CDM	Coloured Detrital and Dissolved Material
CDOM	Coloured Dissolved Organic Matter
CZCS	Coastal Zone Colour Scanner
DOC	Dissolved Organic Carbon
ERT	Equation of Radiative Transfer
FWHM	Full-Width at Half Max
GSM	Garver Siegel Maritorena
IOP	Inherent Optical Property
LMI	Linear Matrix Inversion
MERIS	Medium Resolution Imaging Spectrometer
MOBY	Marine Optical Buoy
MODIS	Moderate Resolution Imaging Spectroradiometer
NCOM	Navy Coastal Ocean Model
NDT	Nitrate Depletion Temperature
NN	Neural Network
NPOESS	National Polar-orbiting Operational Environmental Satellite System
POC	Particulate Organic Carbon
QAA	Quasi Analytical Algorithm
RGB	Red Green Blue
RMSE	Root Mean Square Error
SeaBASS	SeaWiFS Bio-Optical Archive and Storage System
SeaWiFS	Sea-viewing Wide Field-of-view Sensor
SST	Sea Surface Temperature
VIIRS	Visible Infrared Imager Radiometer Suite
VSF	Volume Scattering Function

Mathematical Notations

Symbol	Description	Units
a	Absorption coefficient	m^{-1}
a_d	Absorption coefficient of non-algal particles	m^{-1}
a_g	Absorption coefficient of yellow substance (gelbstoff)	m^{-1}
a_{dg}	Sum of absorption coefficients of non-algal particles plus yellow substances (gelbstoff)	m^{-1}
a_{ph}	Absorption coefficient of phytoplankton pigments	m^{-1}
a^*_{ph}	Specific absorption coefficient of phytoplankton pigments (normalized to chl concentration)	m^2 (mg chl)$^{-1}$
a^+_{ph}	Absorption coefficient of phytoplankton pigments normalized at 440 nm	
a_w	Absorption coefficient of water molecules	m^{-1}
b	Scattering coefficient	m^{-1}
b_f	Forward scattering coefficient	m^{-1}
b_b	Backscattering coefficient	m^{-1}
b_{bp}	Backscattering coefficient of particles	m^{-1}
c	Beam attenuation coefficient	m^{-1}
C	Concentration of chlorophyll-a	mg m^{-3}
E_d	Downwelling irradiance	W m^{-2}
E_{od}	Downwelling scalar irradiance	W m^{-2}
E_u	Upwelling irradiance	W m^{-2}

K_d	Diffuse attenuation coefficient for downwelling irradiance	m^{-1}
k_u	Diffuse attenuation coefficient for upwelling radiance	m^{-1}
K_{VIS}	Diffuse attenuation coefficient for downwelling broad band (350–700 nm) irradiance	m^{-1}
L	Radiance	$W\ m^{-2}\ sr^{-1}$
L_u	Upwelling radiance	$W\ m^{-2}\ sr^{-1}$
L_w	Water-leaving radiance	$W\ m^{-2}\ sr^{-1}$
L_{wN}	Normalized water-leaving radiance	$W\ m^{-2}\ sr^{-1}$
Q	Ratio of upwelling irradiance to upwelling radiance	sr
r_{rs}	Remote sensing reflectance just below the surface	sr^{-1}
R	Irradiance reflectance	
R_{rs}	Remote sensing reflectance just above the surface	sr^{-1}
S	Slope of absorption coefficient of yellow substance	nm^{-1}
Y	Exponent for particle backscattering coefficient	
β	Volume scattering function	$m^{-1}\ sr^{-1}$
λ	Light wavelength in free space	nm
η	Ratio of molecular scattering to total scattering	
μ_d	Mean cosine of the downwelling irradiance	
μ_u	Mean cosine of the upwelling irradiance	